Universitat Politècnica de Catalunya

Departament de Física

Dynamics and physical processes involving extreme temperatures in the Iberian Peninsula and Iraq

by

Ali Jasim Mohammed

A thesis submitted to the Universitat Politècnica de Catalunya in conformity with the requirements for the Doctoral degree, speciality in Computational and Applied Physics

Director:

Marta Alarcón Jordán

Co-director:

David Pino González

Barcelona, July 2018

Acknowledgements

First and foremost, I would like to deeply thank Dra. Marta Alarcón for her expert guidance and support. Thanks to her by helping in scientific and technical questions, ideas, comments and encouragement, I felt energized and highly motivated to immerse myself in the work after each meeting with her.

I am very grateful to Dr, David Pino for his valuable advice and insightful comments that helped me focus my ideas and for providing an inspiring example of leadership that creates a congenial and stimulating working atmosphere.

We acknowledge the financial support from the Spanish Government through the projects CGL2012-39523-C02-01/CLI, CGL2012-39523-C02-02, CGL2012-37416-C04-03, CGL2016-75996-R and CTM2017-89565-C2-2-P. Ali Jasim Mohammed wishes to thank the Iraqi Ministry of Higher Education and Scientific Research and Mustansiriya University for their support in carrying out this research. We thank the European Centre for Medium-Range Weather Forecasts for making freely available the ERA13 Interim reanalysis and the operational model. We thank J. Tuset (Univ. Lleida) for producing Fig. 1. We would also like to thank Dr. I. Bladé (University of Barcelona) for providing the summer NAO index data and Drs. J. Martín-Vide and J. A. López-Bustins (University of Barcelona) for the WeMO index data.

Last but not the least, nobody has been more important to me in the pursuit of this project than the members of my family. I would like to thank my Aunts (Drs. Ahlam, Molkeya and Maleya and My Uncle Dr. Hafidh Farhan, my little sister (Halaa), also mother-in-law (Jehan), brother-in-law (Mohammed) and sister-in-law (Zina), for supporting me spiritually throughout writing this thesis and my life in general.

Most importantly, I wish to thank my loving and supportive wife, Lina, and my three wonderful children, Ayaa, Saif and Jannat, who provide unending inspiration.

Thanks for all your encouragement!

Abstract

The occurrence of heat waves and cold spells has received special attention in recent years due to their impact on human health, ecosystems and economy. In the context of climate change, there is evidence that extreme temperature episodes, and not only the mean temperature, are changing in response to anthropogenic radiative forcing.

This thesis focuses in the study of the dynamics and the physical processes leading to temperature extremes in two regions located at the west and the east sides of the Mediterranean Sea: the Iberian Peninsula (IP) and Iraq. The 12–hourly 2–m height maximum/minimum temperatures obtained from the 1º×1º ERA–Interim database in the period 1994–2013 are used. At each grid point, hot/cold extremes are defined as those events in which T2MAX/T2MIN was above/under its 99.9^{th}/0.1^{th} percentile. The results in both study areas show that there is a positive trend in the occurrence and persistence of both hot and cold events.

By using the Hybrid Single-Particle Lagrangian Integrated Trajectory (HYSPLIT) model, the 10-day back-trajectories of the air masses producing the extremes are analysed. Rather than meridional advection, the primary cause behind the occurrence of hot extremes seems to be progressive diabatic warming, which becomes accentuated the days before the episode. The extremes are caused by air masses with long residence times and by recirculation processes during summer days of weak baric gradient. The air masses producing the extreme cold events have faster trajectories. Cold events are mainly associated with advection of air-masses from northeast and north Europe for IP and from Siberia and East Europe for Iraq.

In the IP, Principal Component Analysis of the pressure and geopotential fields has also been carried out to identify the associated synoptic scale configurations, showing that advection during cold episodes is induced by the presence of a relative low in the central Mediterranean and a blocking high in the North Atlantic and/or in northeast Europe.

We analyse the correlations between temperature extremes and the modes of climatic variability affecting the Mediterranean basin: North Atlantic Oscillation (NAO), Western Mediterranean Oscillation (WeMO), Arctic Oscillation (AO) and East Atlantic Oscillation (EA). In the IP, a significant positive correlation ($p < 0.01$) is found between the annual average of the extreme hot temperatures and annual WeMO. Significant

negative correlation ($p < 0.01$) is found between the number of cold days and the annual index for NAO. In Iraq, significant positive correlation ($p < 0.01$) between the annual average of the extreme hot temperatures and annual EA is found.

The mechanisms underlying the occurrence of hot extreme temperatures for specific events occurred in IP have been analysed by using both HYSPLIT and the Weather Research and Forecast (WRF) mesoscale model. For the event that occurred on 10 August 2012, that affected the highest number of grid points of the series, the synoptic situation shows an omega blocking system and local recirculation of warm air masses. The analysis of the only hot extreme event recorded just at one single grid point, on 15 August 2012, shows that not synoptic or mesoscale conditions substantially different from those of the neighbours grid point were given.

Resum

L'estudi de les causes de les onades de calor i fred ha tingut una atenció especial en els últims anys a causa del seu impacte en la salut humana, els ecosistemes i l'economia. En el context del canvi climàtic, hi ha evidències que mostren que els episodis de temperatura extrema, i no només la temperatura mitjana, estan canviant en resposta al forçament antropogènic.

Aquesta tesi se centra en l'estudi de la dinàmica i els processos físics que condueixen a temperatures extremes en dues regions situades a l'oest i l'est del mar Mediterrani: la Península Ibèrica (PI) i Iraq. S'utilitzen les temperatures màximes/mínimes a 2 m d'altura, obtingudes a partir de la base de dades ERA-Interim en el període de 20 anys 1994-2013. En cada punt de la malla que cobreix les dues àrees d'estudi, cada 12 hores (03 i 15 UTC) amb resolució 1ºx1º, es defineixen els extrems càlids/freds com aquells episodis en què T2MAX/T2MIN es troba per sobre/sota del percentil 99.9/0.1. Els resultats en ambdues àrees d'estudi mostren que hi ha una tendència positiva en l'ocurrència i persistència d'episodis tant càlids com freds.

Mitjançant l'ús del model Hybrid Single-Particle Lagrangian Integrated Trajectory (HYSPLIT), s'analitzen les trajectòries, endarrere en el temps, de 10 dies de durada, de les masses d'aire que produeixen els extrems. La causa principal que explica l'aparició d'extrems càlids sembla estar associada a un escalfament diabàtic progressiu, que s'accentua els dies anteriors a l'episodi, i no pas a l'advecció de masses d'aire des d'àrees més càlides. Els extrems càlids són produïts per masses d'aire amb temps de residència llargs sobre la PI i per processos de recirculació que tenen lloc durant dies d'estiu amb un feble gradient bàric. Les masses d'aire que produeixen dies de fred extrem tenen associades trajectòries més ràpides que les masses d'aire càlides. Els episodis freds a la PI es relacionen principalment amb advecció de masses d'aire procedents del nord-est i el nord d'Europa, i per l'Iraq, procedents de Sibèria i l'Est d'Europa.

A la PI també s'ha realitzat l'anàlisi de components principals dels camps de pressió i geopotencial per identificar les configuracions d'escala sinòptica associades; aquestes mostren que l'advecció durant els episodis de fred és induïda per la presència a la Mediterrània central d'una baixa relativa i un alta de bloqueig a l'Atlàntic Nord i/o al nord-est d'Europa.

S’analitzen també les correlacions entre l’ocurrència de temperatures extremes i els principals modes de variabilitat climàtica que afecten la conca mediterrània: Oscil·lació de l'Atlàntic Nord (NAO), Oscil·lació de la Mediterrània Occidental (WeMO), Oscil·lació Àrtica (AO) i Oscil·lació de l'Atlàntic Oriental (EA). A la IP es troba una correlació positiva significativa ($p < 0,01$) entre la mitjana anual de les temperatures extremes càlides i l’índex anual de WeMO. També es troba una correlació negativa significativa ($p < 0,01$) entre el nombre de dies freds i l'índex anual de NAO. A Iraq, s’ha obtingut una correlació significativa positiva ($p < 0,01$) entre la mitjana anual de temperatures extremes càlides i l’índex anual de EA.

Els mecanismes subjacents a l'aparició de temperatures extremes càlides per a episodis extrems específics ocorreguts a la IP s'han analitzat utilitzant el model a gran escala HYSPLIT i el model mesoescalar Weather Research and Forecast (WRF). Per a l'episodi que es va produir el 10 d'agost de 2012, que va afectar simultàniament al nombre més gran de punts del període, l’estudi sinòptic mostra una situació de bloqueig associada a una configuració ‘omega’, que provoca recirculació de massa d’aire. L’anàlisi de l’únic episodi càlid que va afectar a un sol punt de la malla, el 15 d’agost de 2012, mostra que les condicions sinòptiques i/o mesoescalars no van diferir substancialment de les que es van donar en els punts circumdants al punt de l’extrem càlid.

Contents

List of Figures

List of Table

Chapter 1

Chapter 1
Introduction

1.1.Motivation and objectives

The occurrence of heat waves and cold spells is attracting special attention in the last years due to their impact on human health, on the ecosystems and on other aspects such as the economy. In the context of climate change, there is evidence that extreme temperature episodes, and not only mean temperatures, are changing in response to the anthropogenic radiative forcing (Katz and Brown, 1992). Episodes of hot extremes can affect many aspects of human life such as death rate, comfort, environment, agriculture and hydrology (Schindler, 1997). For example, the heat wave that hit Europe in summer 2003 led to the destruction of large tracts of forest, the interruption of electricity, and it affected water availability, ecosystems and agricultural production. It also claimed thousands of lives (UNEP, 2004). In the last years, significant efforts have been made to assess changes in the frequency, intensity and duration of heat waves and cold spells (Fonseca *et al.*, 2016, Mazon *et al*., 2014, Alexander *et al.*, 2006; Brunet *et al*., 2007; Frich *et al*., 2002). These studies have analysed the extreme temperatures at different spatial scales, ranging from regional to global (Del Río *et al*., 2011; Fernández-Montes *et al.*, 2013). In general, most of these results revealed a significant upward (downward) trend in frequency and duration of hot (cold) extreme (Alexander *et al*., 2006; Salman *et al.*, 2017).

The dynamics of hot extreme events in Europe has been studied by many authors, who have investigated their effects in several fields, such as agriculture (Jolly *et al*., 2005), human health (Smoyer-Tomic *et al*., 2003; Meehl and Tebald., 2004), and discomfort (Matzarakis

and Nastos, 2010; Nasto and Matzarakis, 2012). Bieli *et al.* (2014) and Santos *et al.* (2014) used a Lagrangian approach to study the temperature extreme events in Europe to understand its dynamics. They tracked the backward trajectories of the air masses associated with extreme temperature events to identify their origin and to study the physical mechanisms that occur along their pathway.

The Mediterranean regions, in the transition zone between the mild, wet domain of the mid-latitudes and the dry area of the tropical anticyclone belt, are especially sensitive to climate change. The persistent large-scale circulation patterns associated with the production of extreme temperatures in Europe is known to interfere with hemispheric oscillation patterns, in particular, North Atlantic Oscillation (NAO) and Arctic Oscillation (AO). The anomalously cold winter of 2010 was found to be strongly linked to a negative phase of the NAO (Cattiauxet *et al*., 2010; Al-Khalidi *et al.*, 2017; Ríos-Cornejo *et al.*, 2015; Comas-Bru and Mcdermott, 2014).

The aim of this work is the study of the dynamics and the physical processes related to extreme temperatures in two regions: the Iberian Peninsula (IP), located at the west of the Mediterranean Sea and Iraq, in western Asia, focusing on the following questions:

1. What are the synoptic situations that lead to the development of temperature extremes?
2. What physical mechanisms contribute to the occurrence of temperature extremes?
3. Is there any influence of the climate variability in the frequency of occurrence of extreme temperatures?
4. What are the time scales in which an air mass becomes extreme with respect to the local temperature distribution along its trajectory?
5. Are there inter-regional differences in the development of extreme temperatures between the two regions?

Chapter one offers an overview of the definitions used to characterize hot and cold extremes in IP and Iraq and their interactions with the large-scale circulation and synoptic patterns. The Köppen-Geiger climate classification for the two regions is also

introduced. Finally a brief introduction to the use of trajectory models and the Weather Research and Forecasting mesoscale model (WRF) is given. Chapter 2 describes the methodology used for the two regions. Afterwards, the results are presented along three chapters. Chapter 3, is focused on the study of extreme temperature episodes in Iberian Peninsula (IP) for the 20-year period 1994-2013. The conductive meteorological conditions have been characterized by means of i) a Lagrangian approach to determine the air-mass pathways; ii) the study of the evolution of the physical variables along the atmospheric trajectories; and iii) the identification of the synoptic situations by Principal Component Analysis of the pressure and geopotential fields. Chapter 4 is focused in analysing two hot extreme events that occurred in IP by applying both the Hybrid Single-Particle Lagrangian Integrated Trajectory model (HYSPLIT) model and the WRF mesoscale model. Chapter 5 presents the results of the study of hot/cold extreme episodes in Iraq for the same time period, using the same methodology. Finally, the summary and conclusions are presented in chapter 6.

1.2. Hot and Cold Extremes in the Iberian Peninsula and Iraq

1.2.1. Study area

The Mediterranean basin (MB) is situated in the subtropical latitudes and have a complex topography with many mountain ranges distributed in both west-east and south-north such as the Pyrenees, the Alps and the Balkans. The two regions studied here have in common their proximity to the Mediterranean Sea. The IP is located in the western region of the MB and dominated in its eastern fringe by a Mediterranean climate. Iraq, at the east of the MB is located on the northern Persian Gulf, on the historically known as Mesopotamia. Although a Mediterranean climate does not predominate in Iraq, it is strongly influenced by its proximity.

The IP, located in Southwest Europe, (lat: 43°47′ N – 36°01′ N; long: 9°30′ W – 3°19′ E) (Fig. 1.1), has a sharply differentiated topography: the coastland areas (< 200 m a.s.l.), the interior plateau (200–1000 m a.s.l.) and the high mountain areas (> 1000 m a.s.l.). These mountain ranges are organized from east to west and include the Pyrenees, the Cantabrian mountains, the northwest ranges, the Central Range, the Iberian Range, and the Betic Range (Oliva *et al.*, 2018). IP climate is influenced by their locations in the subtropical transition area in the western European face (Lionello, 2012, Angulo *et al.*, 2016), and it also has large marine influence due its location between the Atlantic Ocean

and the Mediterranean Sea. The distribution of the mountain systems led to dividing the IP area into four main climatic areas, 1) the north coast; 2) the northern mid-west regions; 3) the southern coast and southwestern region; and 4) the Mediterranean coast (Font Tullot, 1983; Martín and Olcina, 2001; Angulo *et al*., 2016; Peel *et al*., 2007). In general, the climate is very seasonal, controlled by westerly winds, and the Azores anticyclone, which predominates in summer (Paredes *et al*., 2006; Angulo *et al*., 2016).

The annual average of maximum air temperature in IP varies between 10°C in areas of high altitude and 22°C, in the southwest region. The annual average of minimum air temperature in IP varies between below 0°C in areas of high altitude, and higher than 15°C on the south coast of Portugal. In summer, the maximum temperature is recorded in Extremadura and inland Andalusia. In winter, the average values for minimum air temperature (< –2.5°C) occur in areas of high altitude in the northern regions (Iberian Climate Atlas, 2011).The largest precipitation values are above 2200 mm in the mountainous areas of north-eastern Portugal and some areas of southwestern Galicia, close to the "Rias Baixas" in Spain. The lowest rainfall values are below 300 mm recorded in the southeast of Spain (Iberian Climate Atlas, 2011).

At the other side of the Mediterranean Sea, Iraq is located in southwest Asia (lat: 29°15′N–38°15′N and long: 38°45–48°45′E) in the northern temperate zone, but with continental and subtropical climate characteristics (Fig. 1.1). Most of the Iraq surface is mainly of lowlands that do not exceed 300 m of altitude. Three major geographic regions can be identified: desert in the west and southwest, extending uplands between the Euphrates and Tigris rivers; mountains in the north and northeast; and alluvial lowland in the central and southern regions. In northern Iraq, mountains located E-W rise to over 3600 m near the Turkish and Iranian borders including the Taurus Mountains near Turkey and the Zagros Mountains that lie across the border in Iran (Malinowski, 2002). The annual mean maximum temperature range is 41 - 48 ºC, in summer; especially hot are the central and southern regions. The annual mean minimum temperatures reach the freezing point in the north and stay around 5°C in the southern area (Salman *et al*., 2017).

Most of the precipitation occurs during January and March. Mean monthly precipitation varies between 102-229 mm in northern Iraq, while in the center and southern regions varies between 25-76 mm. The south-western side of Iraq has the lowest mean amounts, 2.5 mm. Isolated, windward mountain sites have annual averages of 508 mm (Walker,

2005). In general, the annual average precipitation in Iraq is about 120 mm, which is less than 15% of the average rainfall in the world (860 mm) (Al-Salihi *et al.*, 2013).

1.2.2. Definition of extreme temperature

According to the book Glossary of Meteorology (Glickman 2000), the concept of extreme temperature refers to "the highest and lowest values of temperature attained at a specified location during a given time interval, for example daily, monthly or seasonally ". However, in general, the meteorological literature does not provide a specific definition of hot and cold extremes according to their nature, instead, individual deviations from prevailing climatic conditions are used to identify hot and cold extremes. In the present study, the percentile-based index, which takes into account the temperature at each grid point, will be used to select the hot and cold extremes. That is, the events belonging to the 0.1% hottest/coldest events of the complete dataset will be selected as extremes.

1.2.3. Interactions with large-scale circulation patterns

The production of extreme temperatures might be associated with extreme phases of low-frequency variability patterns, particularly for Western Europe the North Atlantic Oscillation (NAO) and the Arctic Oscillation (AO) (Pfahl and Wernli, 2012).

The NAO is a phenomenon in the North Atlantic Ocean caused by fluctuations at sea level between the Icelandic low and the Azores high pressures. These fluctuations control prevailing wind speed and direction and the storm routes across the North Atlantic Ocean.

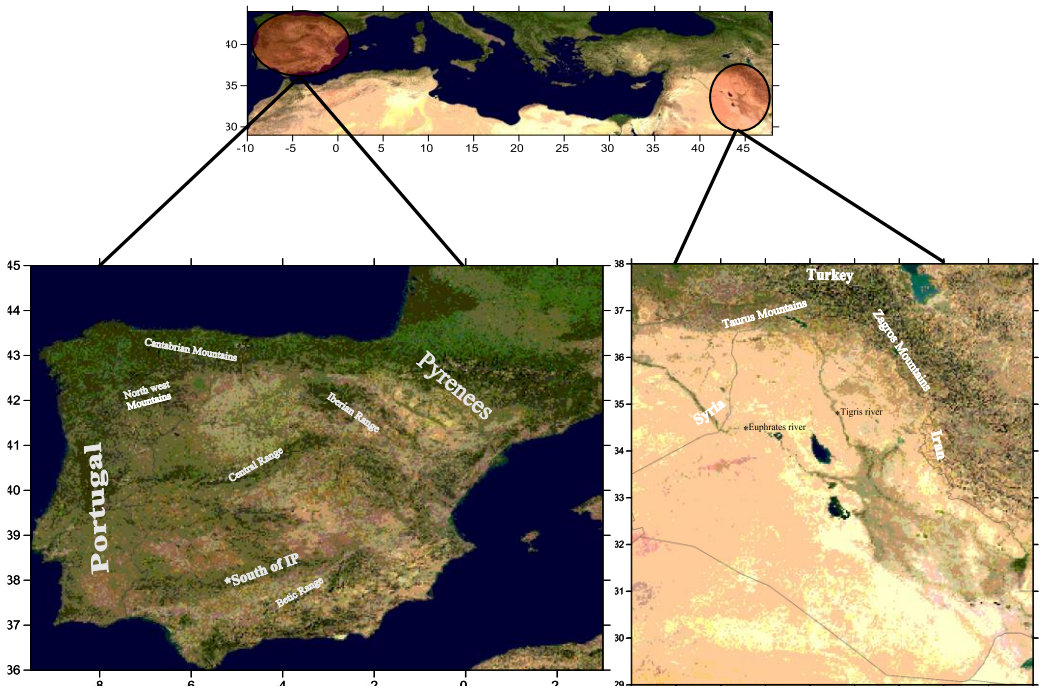

Figure 1.1: Geographical situation of the Iberian Peninsula (left) and Iraq (right). Source: Map Server WMS Demo, Blue Marble World Elevation and Bathymetry Raster.

The NAO alternates between two phases, positive and negative: "The positive phase of the NAO reflects below-normal heights and pressure across the high latitudes of the North Atlantic and above-normal heights and pressure over the central North Atlantic, the eastern United States and western Europe. The negative phase reflects an opposite pattern of height and pressure anomalies over these regions." (Hurrell, 1995).

Lorenz (1950), Kutzbach (1970), Thompson and Wallace (1998, 2000) and Thompson *et al*. (2000) described the AO as a fluctuation in the mean sea level pressure between the Arctic and North Atlantic oceans. The AO pattern is directly connected to weather patterns in several sites of Europe, North America and Asia (Ambaum *et al*., 2001; Gong *et al*., 2001; Black, 2002; Wettstein and Mearns, 2002). Hansen (2013) described the mechanism by which the AO influences at points remarkably farther from the Arctic, as follows:

"The degree to which Arctic air penetrates into middle latitudes is related to the AO index, which is defined by surface atmospheric pressure patterns. When the AO index is positive, surface pressure is low in the polar region. This helps the middle latitude jet stream to blow strongly and consistently from west to east, thus keeping cold Arctic air locked in the polar region. When the AO index is negative, there tends to be high pressure in the polar region, weaker zonal winds, and greater movement of frigid polar air into middle latitudes."

The link between the NAO and temperature has been studied by several researchers (Wanner *et al*., 2001; Hurrell *et al*., 2003; Thompson and Wallace, 1998). Hurrell (1995) suggested that there is a link between the global heating and the NAO index. He found a similarity between temperature and the positive phase of NAO. In western Europe, extreme phases of the low-frequency variability patterns such as NAO and AO can lead to the production of extreme temperatures (Pfahl and Wernli, 2012). Favà *et al.* (2016) found significant positive correlation between summer NAO and the maximum temperatures for the northern IP for the 1951–1967 period; while in the 1962–1978 period these correlations were negative and affected the eastern part of IP. Other authors (Rodríguez-Puebla *et al.*, 2010) pointed out no correlations between NAO and the occurrence of warm days in the IP. The relationship between the winter temperature variability over northern Spain and the NAO, AO and East Atlantic Oscillation (EA) were analysed by Sáenz *et al.* (2001a). The only significant correlation was obtained for EA, while NAO and AO did not show any significant correlation. Wallace and Gutzler (1981) described the EA pattern as having three

centers: one located at the southwest of the Canary Islands (25° N, 25° W), another at the west of Great Britain (55° N, 20° W), and the third near the Black Sea (50° N, 40° E). To define the EA pattern, the monthly mean for 500 hPa geopotential height at specific grid points is used. "Thus, a positive pattern index is indicative of an anomalously high 500 hPa height over the North Atlantic and low heights over the subtropical Atlantic and Eastern Europe; a negative pattern index indicates anomalies in the opposite sense."(Knežević *et al*., 2013). EA is one of the most important patterns characterizing the Northern Hemisphere extratropical climate variability (Wallace and Gutzler, 1981; Jones *et al*., 1997). According to the National Oceanic and Atmospheric Administration (NOAA, USA), in Europe for all months, there is a link between the positive phase of the East Atlantic pattern and above-average surface temperatures. In contrast, over the southern USA, during January-May, with the same positive phase, temperatures are below-average (http://www.cpc.ncep.noaa.gov/data/teledoc/ea_ts.shtml).

On the other hand, the Western Mediterranean Oscillation (WeMO) was introduced by Martín-Vide and López-Bustins (2006) to account for some western Mediterranean regions, such as eastern IP, that are weakly or not related to the NAO pattern. The WeMO is defined using the dipole San Fernando (Spain) - Padua (Italy). The positive mode corresponds to high pressures over the Azores and SW Iberian Peninsula and low pressures in the Liguria Gulf. In the positive phase rainfall is more abundant in the Cantabrian peninsular coast and lower in the Mediterranean one. Its negative mode is produced when an anticyclone is situated in central Europe and the north of Italy and low pressures in the SW Iberian Peninsula. The WeMO positive phase has been shown to trigger air masses from the Atlantic to move into the IP, while its negative phase is associated to flows from the Mediterranean (Martín-Vide and Lopez-Bustins, 2006; Lopez-Bustins *et al*., 2008). Most studies have focused on the effect of WeMO on precipitation in the IP (Vicente-Serrano *et al*., 2009), however, few studies deal with its influence on temperature. El Kenawy *et al*. (2012) found a relationship between the negative mode of WeMO and high temperatures during the warm season.

At the east of the Mediterranean Sea hot and cold extreme events are also influenced by hemispheric oscillation patterns, particularly the NAO, the AO and the EA. In Iraq, Al Khalid (2017) found a relationship between the positive phase of NAO and temperature anomalies in winter. These anomalies are caused by the westerly advection of warm air over the Middle East which extends from north of Africa and through the northeast of Iraq.

Also, Salar *et al*. (2014) concluded that NAO positive phase causes an expansion of the desert climatic region and simultaneous diminishes the surface of the other climate regions. On the other hand, little attention has been devoted to the impact of EA in the Middle East climate despite it is one of the most important patterns characterizing the extratropical climate variability in the Northern Hemisphere (Wallace and Gutzler 1981; Jones *et al*. 1997).

1.2.4. Interactions with the synoptic patterns

The weather features in IP are highly influenced by the proximity of the almost enclosed Mediterranean Sea, representing an important source of energy and moisture for cyclone and anticyclone development. The three most influential synoptic systems in the meteorology of the IP are the subtropical high-pressure system, the winter Siberian anticyclone, and the Saharan depression (Font-Tullot, 2000). Among them, the most determinant is the first one, commonly known as the Azores anticyclone, which is characterized by a semi-permanent anticyclone region with relatively consistent high pressure located at around 30°N latitude in winter. The Azores High has a great influence on weather and climate over western Europe, but also over northwestern Africa and eastern United States (Fig.1.2). In summer, the pressure centere shifts towards 35°N across the Iberian Peninsula and a ridge may appear across France, northern Germany and even the southeast of the UK. In early winter (November, December) the Azores High tends to be located over the western Mediterranean while, in January, it is virtually absent, so its influence is almost null. From February to April, the Azores High is still far out over the Atlantic (Littmann, 2000). In summer, it is reinforced and displaced to the north. Both in winter and summer, the central pressure lies around 1024 hPa, but conditions are more variable in winter (Davis *et al*., 1996).

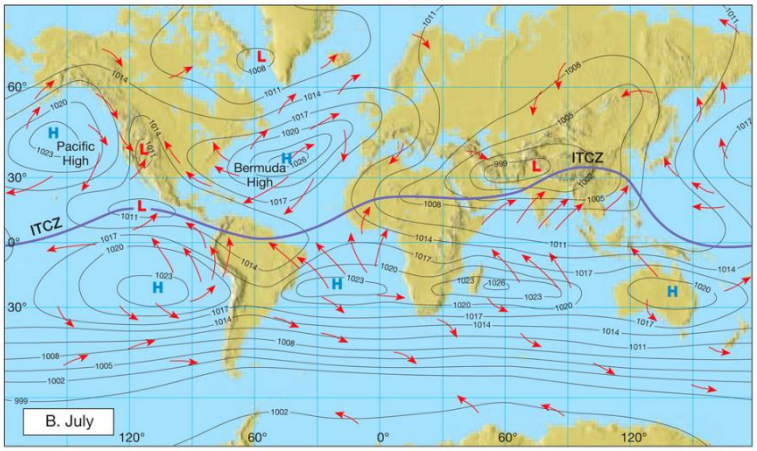

Figure 1.2: Mean sea level pressure and prevailing winds on July (Person Prentice Hall.Inc).

The second synoptic system which influences the west side of the Mediterranean basin is the Siberian anticyclone, an area of semi-permanent cold high-pressure cells that develops over Siberia during the winter months of the Northern Hemisphere. These cold high-pressure cells inhibit cloud formation, maximizing radiative cooling; they are characterized by the particularly high pressures on the center, which exceed 1050 hPa. The Siberian anticyclone is one of the principal source of polar air masses. Mean January temperatures at certain locations within this pressure system are the lowest in the Northern Hemisphere (-46° C). The anticyclone forms because of the intense cooling of the surface layers over the continent during winter. In summer, the Siberian high is replaced by a low-pressure system, resulting in a summer precipitation maximum across almost the whole Siberia.

Finally, the third synoptic system affecting IP is the Saharan depression, a thermal low-pressure system that originates at North Africa. Thermal lows occur frequently, 50% of the days, above the Iberian Peninsula during summer (Portela and Castro, 1991). The thermal low pressure has been classified as one of the important weather types in the Iberian climatology. Besides, the variations in the Saharan depression have a direct influence in the occurrence of North African air-mass intrusions over the IP.

The Iraqi region has a climate similar to that of the Eastern Mediterranean (EM) region, characterized by rainy winters and dry and hot summers. Therefore, the foremost influential synoptic systems in the meteorology of the EM are the subtropical high-pressure system, the winter Siberian anticyclone, the monsoon low pressure, the Red Sea trough and the Mediterranean low (extra-tropical low) (Alhamawi, 2008).

During the Iraq summer, starting from mid-May, the most dominant synoptic pattern is the Indian monsoon low pressure, which is described as a seasonal warm and moist air into the thermally generated low-pressure areas of the continental interior, where it rises releasing both precipitation - initiating the wet season - and latent heat. This causes heavy rains carried by high winds from the Indian Ocean and over South Asia (Milind, 2006). In general, the eastern Mediterranean area is affected by the massive monsoon thermal low which develops over northwest India and may extend westward over Iran and Iraq through the Persian trough (Tyrlis *et al*., 2013). During the winter monsoon, a large persistent high-

pressure zone over Asia drives cool and dry air southwards, toward the tropics, providing the monsoon region (India, Pakistan, Iran, Iraq and Arab gulf region) with its dry season.

The second pressure system that influences the EM region is the Mediterranean low pressure, dominant at mid-latitudes. Its passage is associated with strong winds, precipitation, and temperature changes. The Mediterranean lows are traveling cyclonic storms of up to 2000 km in diameter and with surface winds of 6 to 52 km/h. Mediterranean cyclones are generally characterized by shorter life cycles and smaller spatial scales than the extra-tropical cyclones developing over the Atlantic. Their radius are generally within the sub-synoptic scale (< 500 km), with a mean duration of a day or longer (Flocas *et al.*, 2010). The Mediterranean low is the result of dynamic interactions of warm tropical and cold polar air masses at the polar front that causes the warm air to cyclonically rise and mix with colder upper atmospheric air which led to transports excess energy from lower to higher latitudes (Trigo *et al.*, 2002). Mediterranean lows can produce a wide variety of precipitation types: rain, freezing rain, hail, sleet, and snow. Most frequently forming in the baroclinic zones, Mediterranean lows are characterized by strong horizontal temperature gradients (Maheras *et al.*, 2002).

The third pressure system that influences the EM region is the Subtropical high pressure (Fig.1.3). The eastern side of a Subtropical high is associated with subsiding stable air, which produces low relative humidity and sunny skies; the atmosphere at the far western side is less stable and can be associated with cloudy, humid weather. Thus, the world's major deserts are located at the eastern side of the Subtropical high, and the aridity of the Mediterranean basin is due to the subsidence of air in the system (Alpert and Ziv, 1989). Subtropical anticyclones exert the highest surface pressure in the summer - they shift toward the poles in spring and toward the equator in the autumn. The north-to-south variation of the subtropical anticyclone has a substantial influence on seasonal climate. During summer, the central pressure rises higher than 1025 hPa and is characterized by hot days with few or no clouds, morning mist and light winds. In winter, the central pressure drops around 1022 hPa and is characterized by cloudless skies (but less radiation due to the low angle of the sun), cold days and even colder nights due to lack of cloud cover, and fog and frost formation during the night (Rodwell and Hoskins, 2001).

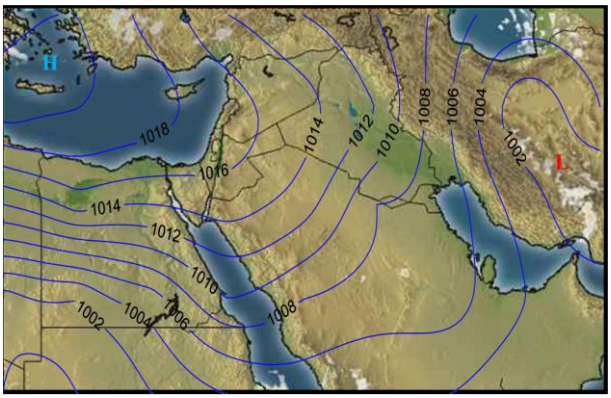

Figure 1.3: Effects of the Subtropical high on the Eastern Mediterranean region on July (Alhamawi *et al*., 2011).

1.3. The Köppen-Geiger climate classification for the Iberian Peninsula and Iraq

In 1900, Wladimir Köppen (1846–1940) presented the first quantitative classification of world climates in a world map. This classification was updated in 1954 and 1961 by Rudolf Geiger (1894–1981). The Köppen-Geiger classification is the climate classification most frequently used, and, in 2001 Essen Wagner presented a complete review. A large number of climate studies adopted this edition of the Köppen-Geiger map. This climate classification has been thoroughly applied to a wide range of topics in climate research as well as in physical geography, hydrology, or agriculture (e.g. Kottek *et al*., 2006; McMahon *et al*., 1992; Peel *et al*., 2004, 2006; Kalvova *et al*. 2003).

In the IP, according to the last version of the Köppen-Geiger climate classification maps (Peel *et al*., 2007) (see Fig.1.4), there is a wide variety of climatic zones due to the complex topography and the proximity of the Atlantic Ocean and the Mediterranean Sea. For simplicity, only the four main climate types have been considered in this work: BSK, Csa, Csb and Cfb. The BSK (Arid–Steppe–cold) region spreads at the southeast of the Peninsula and the Ebro Valley, part of the southcentral plateau region and Extremadura. The Csb region (temperate with dry or temperate summer) covers most of the northwest of the Peninsula, as well as almost all the west coast of Portugal, and numerous mountainous regions within the Peninsula. The Csa region (temperate with dry or hot summer) covers the southwest of the Peninsula, within an area of medium-altitude and the Balearic Islands. Finally, the Cfb region (temperate with a dry season and temperate

summer) covers almost all the north of IP, including the Cantabrian Mountains, the Pyrenees and part of the northern central plateau.

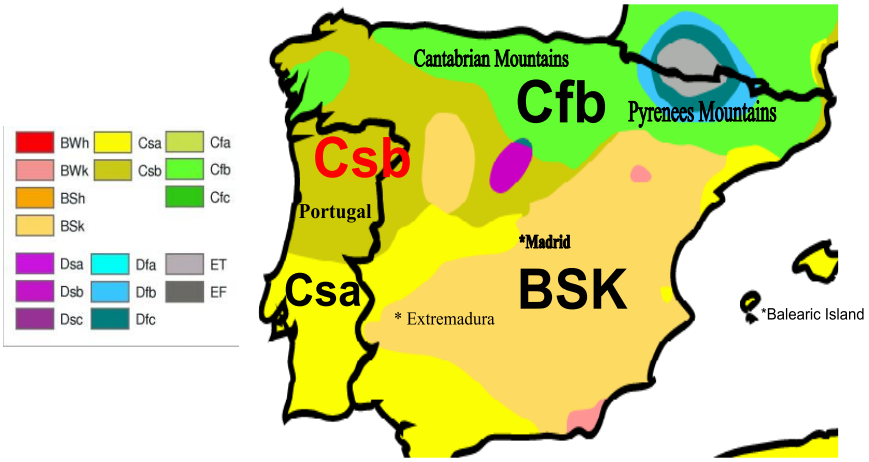

Figure 1.4: The Köppen -Geiger climate type map of IP (Peel *et al*., 2007).

Due of its location, the annual movements of subtropical high pressure and mid-latitude low pressure are reflected in Iraq's climate, existing only three climate regions. First, the southern half of Iraq, from the coastal areas near Basra (south of Iraq near Kuwait) to the Syrian Desert, is influenced by the subtropical high-pressure zone and it is classified as a Subtropical Desert (BWh). Second, the region at the north of Baghdad, significantly wetter, particularly in winter, is classified as a Subtropical Steppe (BSh). Finally, in the northern mountainous regions, where the conditions are much cooler and rainfall more common, the climate is the Mediterranean or Dry-Summer Subtropical (Csa) (Peel *et al*., 2007).

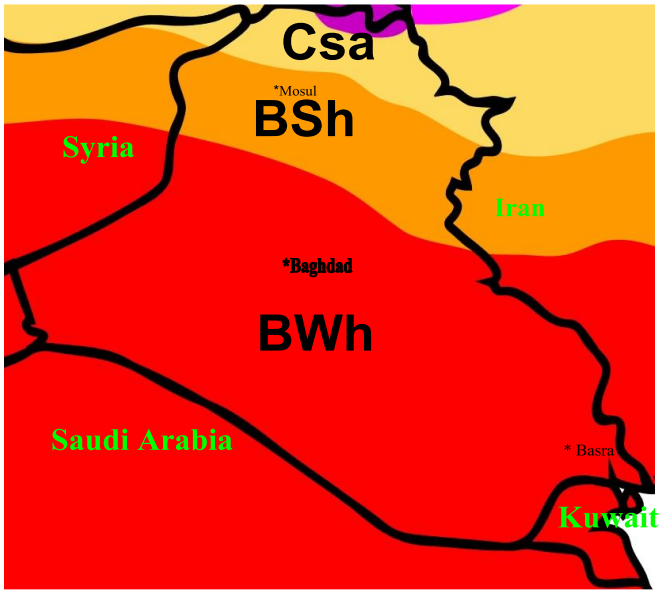

Figure1.5: The Köppen -Geiger climate type map of Iraq (Peel *et al*., 2007).

1.4. Trajectory and WRF models

The Lagrangian approach to study the atmosphere focuses on individual air parcels as they move through time and space (the observer being incorporated into the particle motion). The paths of these air parcels are known as trajectories. Many applications in synoptic meteorology and long-range transport studies have used trajectory models, for instance, in climatology, to identify pathways of water vapour transport (Rong Fu *et al*., 2006; Kurita, 2011; Brimelow and Reuter, 2005), in air pollution, to study the atmospheric transport of chemical compounds (Seibert *et al*., 1994; Stohl, 1996; Charron *et al*., 1998), or mineral dust (Escudero *et al*., 2006; McGowan and Clark, 2008). More recently, statistical trajectory models have been applied to study the atmospheric behavior of biological material such as pollens, fungal spores (Belmonte *et al*., 2008), and living organisms like butterflies (Stefanescu *et al*., 2007) or moths (Dantart *et al*., 2009). Bieli *et al*. (2014) and Santos *et al*. (2014) used the Lagrangian approach to study the dynamics of extreme temperature events in different European regions to understand the physical mechanisms associated with them.

In regions with complex orography as the IP, the broad spatial resolution of the trajectory models cannot solve with enough accuracy the involved meteorology when specific episodes are analysed. A nested model such as Weather Research and Forecasting (WRF) model is essential for simulating, at high resolution, these specific meteorological situations. WRF model has been widely used for different offline simulations, such as storm prediction and research, air quality modelling, precipitation, hurricane and tropical storm prediction, and regional climate (Michalakes *et al*., 2004; Izquierdo *et al*., 2017). The WRF model has been applied to different research topics in a wide range of spatial scales, from thousands to down to a few meters scales, including the global scale, the mesoscale, and the microscale (Skamarock *et al*. 2008). Many authors have used WRF model to study extreme events and heat waves (Gladich *et al*., 2008; Mazon *et al*., 2014). Other authors have analysed the relationship between temperature anomalies and other parameters such as soil moisture (Zeng *et al*., 2014). Gladich *et al*. (2008) analysed the unusual and sudden thermal fluctuation at Friuli Venezia Giulia (Italy) during the night of 27 July 1983. Furthermore, Esbensen *et al*. (2008) studied the impacts of sea surface temperature (SST) and air-sea coupling near oceanic fronts through the analysis of surface winds.

Chapter 2

Chapter 2

Methodology

2.1 Meteorological data

The study used the following data: ECMWF ERA-Interim 12-hourly (03 and 15 UTC) maximum and minimum 2 m height temperature data (T2MAX/T2MIN) covering the Iberian Peninsula (IP) (from 36° N to 45° N and from 9° W to 3° E, with a grid of 13×10 cells) and Iraq (from 29° N to 38° N and from 39° E to 48° E, with a grid of 10×10 cells). At each grid point, hot/cold extremes were defined as events where T2MAX/T2MIN was above/below the 99.9th/0.1th percentile for the 20-years period. The operation yielded 15 hot/cold extremes at each grid point; the IP yielded a total of 130 grid points and 1950 hot/cold extremes, while a total of 1500 hot/cold extreme events over 100 grid points were recorded in Iraq.

The persistence of extreme events was analysed separately for diurnal (15 UTC) and nocturnal (03 UTC) extremes by applying the criterion of the 99.9th/0.1th percentile to the T2MAX/T2MIN data. Duration was then obtained by counting the number of consecutive days with temperatures in the 99.0^{th} /1.0^{th} percentile following and/or preceding each diurnal and nocturnal extreme.

2.2 Correlations with climatic indices

The indices NAO (available at https://climatedataguide.ucar.edu/climate-data/hurrell-north-atlantic-oscillation-nao-index-station-based; Hurrell *et al.*, 2014), WeMO; (available at http://www.ub.edu/gc/2016/06/08/wemo/; Group of Climatology, University of Barcelona), AO; available at http://www.cpc.ncep.noaa.gov/products/precip/CWlink/daily_ao_index/ao.shtml;

National Oceanic and Atmospheric Administration (NOAA)/National Center for Environmental Prediction (NCEP), Climate Prediction Center), and EA (available at http://www.cpc.ncep.noaa.gov/data/teledoc/ea.shtml, NOAA)/NCEP, Climate Prediction Center) were correlated with the annual number of extremes and the annual extreme temperature average. Standardized data (obtained by subtracting the mean and dividing by the standard deviation) are used for the extremes and the climatic indices. The Spearman rank correlation coefficient, the Kendall-tau, and the Pearson coefficient are computed to characterize the relationship between extremes and climatic indices. Considering that climatic indices show their most relevant dynamics during the cold months, both the annual and the winter (December to March) NAO, AO, WeMO and EA indices are used, as well as the summer NAO, which is defined as the leading mode of the July-August sea level pressure variability in the North Atlantic sector (Bladé *et al.*, 2011).

2.3 Trajectory model

A Lagrangian approach was applied by computing backward trajectories to identify the origin and pathway of the extreme air-masses. The Hybrid Single-Particle Lagrangian Integrated Trajectory (HYSPLIT) model was used here. HYSPLIT was developed by the Air Resources Laboratory (ARL) of the NOAA; it received an upgrade in 2001 by NOAA and the Australian Bureau of Meteorology (Draxler and Rolph, 2003). HYSPLIT is widely used in large-scale atmospheric transport research; it employs both Eulerian (concentration over a fixed network) and Lagrangian (standard advection) approaches to its calculation algorithms (Draxler, 1998).

Trajectory computation follows the Lagrangian scheme, where a particle/parcel is assumed to be passively following the wind, thus it is given by the integral of the particle 3D position vector *P*:

$$\frac{dP}{dx} = V\left(x, y, z, t\right) \tag{2.1}$$

where *V* is the velocity vector. The equation is solved numerically according to the improved Euler–Cauchy method of consecutive estimates:

$$P'(t+\Delta t) = P\left(t\right) + V\left(P, t\right)\Delta t \tag{2.2}$$

$$P(t+\Delta t) = P(t) + \frac{1}{2}\left[V(P,t) + V(P', t+\Delta t)\right]\Delta t \quad (2.3)$$

Where P' is the first estimate of the position and the final estimate P is calculated according to an averaging scheme. The order of the integration scheme is set to provide sufficient accuracy where P' is the first estimate of the position and the final estimate P is calculated according to an averaging scheme. The order of the integration scheme is set to provide sufficient accuracy for modelling purposes without overtaxing the computation resources.

The time step Δt can be either fixed or it can vary (1 minute to 1 hour) depending on the particle trajectory, compared to a stability ratio criterion:

$$V_{\max}\Delta t < stability\_ratio \quad (2.4)$$

Where V_{max} is the maximum particle transport speed during the previous hour.

Gridded meteorological fields are remapped into an internal terrain-following vertical coordinate system defined by:

$$\sigma = \left(Z_{top} - Z_{msl}\right)/\left(Z_{top} - Z_{gl}\right) \quad (2.5)$$

Where Z_{top} is the boundary value of the coordinate system, Z_{msl} is the height of the internal coordinate ground level, and Z_{gl} is the height of the ground level. Trajectories are computed above surfaces of $\sigma = ct$. Trajectory computation terminates once the trajectories exceed the boundary values defined in the model setup.

2.3.1 Computation of backward trajectories

The HYSPLIT model, in its Lagrangian mode, is used here to compute 10-day back-trajectories from the gridded NCEP/NCAR (National Center for Atmospheric Research) reanalysis data. Trajectories are computed at two vertical levels: 100 and 1500 m a.s.l, at the time of episode onset. These heights can be taken as representative of the mean atmospheric transport at a synoptic scale within the lower and upper boundary layer (Izquierdo *et al.*, 2014). Stohl (1998) discussed some of the limitations of trajectory analysis concluding that, in general, the path of an air parcel along a trajectory is sensitive to the initial conditions of the model data, uncertainties in the wind field used to calculate

air parcel motions, and interpolation related to model resolution. Errors of 20% of the distance travelled seem to be typical for trajectories computed from analyzed wind fields.

Several of the extremes occurred on consecutive days in a given grid point. In these cases, only the first day of the event was considered in order to focus on the mechanism leading to the extreme production. The number of extreme events by only considering the first day of consecutive extremes was reduced from 1950 to 1275 (hot) and 1238 (cold) in IP, and from 1500 to 870 (hot) and 874 (cold) for events in Iraq.

2.3.2 Trajectory densities

The representation of trajectory densities, i.e. the number of time steps per grid box at different levels, is used to identify source areas of air masses. Densities are computed for the back-trajectories of 4- and 10-days length associated to hot and cold extreme events at the levels of 100 and 1500 m. The domains used for the trajectory density representation is given by the coordinates: 25ºW-25ºE to 20ºN-70ºN for IP, and 00ºE-74ºE to 00ºN-59ºN for Iraq. The maps of trajectory densities help to determine the meridional and horizontal advection development during the extremes, and the median and average length of the back-trajectories.

2.4 Synoptic situation

The meteorological scenarios leading to extreme episodes in the IP are characterized according to Principal Component Analysis (PCA) of the mean sea level pressure and the geopotential height at 850 hPa and 700 hPa. ERA-Interim reanalysis data are used, with a 2º×2º horizontal resolution in a domain covering Europe, the Mediterranean Sea, and North Africa (30ºW-30ºE, 20ºN-70ºN). Several extreme events occurred on the same date at different grid points or on consecutive days over the same grid point. These dates are filtered out, and PCA, computed from the correlation matrix, was applied to the 140 remaining dates in S-mode (correlation between temporal series) and T-mode (correlation between fields). In S-mode, the grid points are the variables and the dates are the cases, whereas in T-mode it is vice-versa in T-mode. S-mode tries to identify homogeneous mean sea level pressure and geopotential regions with respect to time variability. T-mode extracts the spatial variability and the dominant circulation types (Compagnucci *et al.*, 2001; Huth, 1996). PCA was carried out using the correlation matrix.

2.4.1 Weather patterns

The Hess-Berezowsky (HB) catalogue (Hess and Brezowsky, 1977; Gerstengarbe *et al*., 1993, 1999), also known as the Gross-wetterlangen or GWL catalogue, is used to sort out the synoptic patterns. This catalogue conducted a daily classification of 197 European weather patterns from 1881 to 2015, with 29 common weather types based on the 198 fields of mean sea level pressure and geopotential height at 500 hPa (James, 2007).

2.5 Köppen–Geiger climate classification

We have simplified the Köppen–Geiger climate classification (Peel *et al*., 2007) for the IP and Iraq by only considering the four main climate types and three climatic types respectively. The number of grid points (1ºx1º) for each climatic region is also shown in Fig. 2.1. For IP, the four regions correspond to: i) BSK (Arid–Steppe–cold) region is widespread in the east and southeast and includes 40 grid points; ii) Csb (cold–dry summer) region covers the west and northwest of IP, accounting for 22 grid points; iii) Csa (temperate with a dry season and hot summer) is restricted to the southwest of IP covering 26 grid points; iv) Cfb climate (temperate with dry or hot summer) is located in almost all the north of IP, including the Cantabrian Mountains, the Pyrenees and part of the northern central plateau; this region contains 42 grid points (Fig. 2.1a).

For Iraq, the three climatic regions are represented as follows: i) Subtropical Desert BWh (Arid-Desert-Hot), located in the southern half of Iraq, from the coastal areas near Basra to the Syrian Desert, covering 61 grid points; ii) Subtropical Steppe BSh (Arid, Steppe, Hot), the region at the north of Baghdad, with a mountainous topography and significantly wetter, particularly in winter; this region covers 16 grid points; iii) Dry-Summer Subtropical Csa (Temperate, Dry summer, Hot summer) or Mediterranean, in

the northern mountain regions, where conditions are much cooler and rainfall more plentiful, covers 23 grid points of the study area (Fig. 2.1 b).

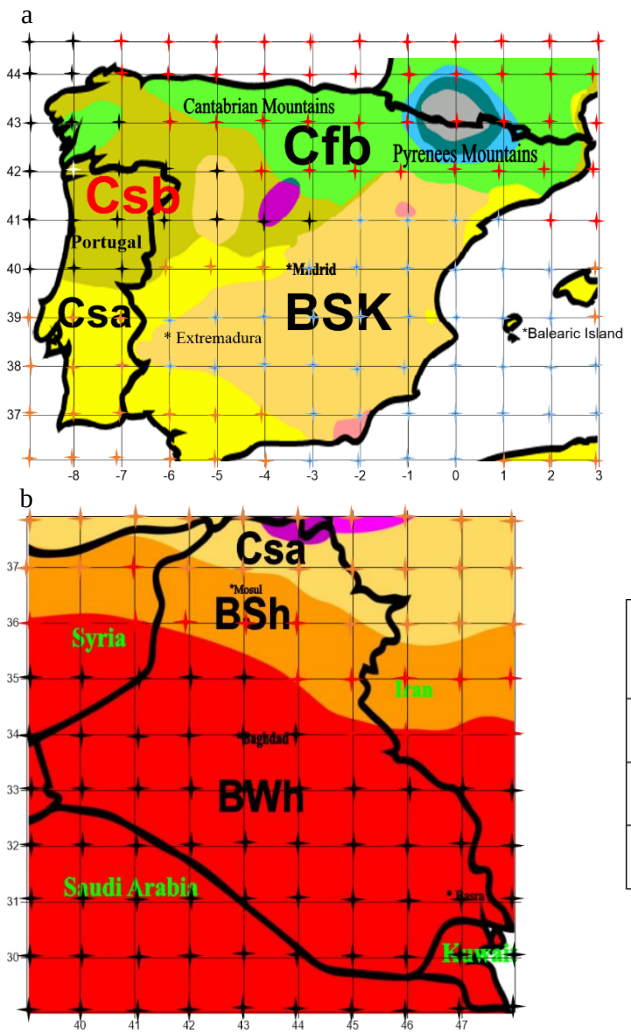

Region		Number of grid points
Cfb/NE		42
Csb/NW		22
BSK/SE		40
Csa/SW		26

Region		Number of grid points
BWh		61
BSh		16
Csa		23

Figure 2.1: The Koppen-Geiger climate type map of the a) IP and b) Iraq (Peel *et al.*, 2007) and the number of grid points for each climatic region.

2.6 Physical variables along the trajectories

In order to understand the dynamics of the air masses leading to temperature extremes, a set of variables was considered along with the back-trajectories: latitude, longitude, height, pressure, temperature, potential temperature, relative humidity, downward solar radiation flux and mixing-layer height (Table 2.1). These variables determine the location and height of the air mass at a given time step, as well as its thermodynamic properties: temperature changes caused by heating/cooling during diabatic/adiabatic vertical displacements, radiative processes, humidity changes and surface heat fluxes. In order to provide a measure of the deviance of an air-mass property from its final state, their

evolution along the back-trajectories were analysed in terms of differences regarding their final value at the grid point, except for mixing-layer height and downward solar radiation. To follow the temporal changes, five percentiles of the variables were traced along the trajectories: the median (50^{th}), the upper and lower quartiles (75^{th} and 25^{th}), and the 5^{th} and 95^{th} percentiles. The physical variables are obtained as an optional output of HYSPLIT. The data is retrieved from the Global Forecast System (GFS) model and interpolated to the coarser grid of the trajectories. As a consequence, there is a certain degree of uncertainty in adopting these thermodynamic values.

Table 2.1. Physical variables used in monitoring extreme events.

Variable	Symbol [Units]
Pressure	P [hPa]
Temperature	T [°C]
Potential Temperature	θ [K]
Relative Humidity	RH [%]
Downward Solar Radiation Flux	DSR [Wm^{-2}]
Mixing-Layer Depth	MLD [m]

2.7 Weather Research Forecast - Advanced Weather Research (WRF-ARW) model

We use the Weather Research Forecast - Advanced Weather Research (WRF-ARW) model (http://www.wrf-model.org/index.php) to study, at high resolution, two events occurred in IP : i) an event that affected simultaneously the highest number of grid points, and ii) the only extreme event that occurred just at a single grid point in the 20 analysed years.

The WRF model was designed for both research and operational forecasting as a next-generation mesoscale model by a joint effort from NCAR, NOAA, NCEP, the Earth System Research Laboratory (ESRL), the Center for Analysis and Prediction of Storms (CAPS) at the University of Oklahoma, and the Federal Aviation Administration (FAA).

2.7.1 Model architecture

WRF is a compressible non-hydrostatic finite difference model running the conservation equations (mass, momentum, energy) describing the atmosphere, on three consecutive stages.

The first stage, the WRF Preprocessing System (WPS), processes the input data by calibrating them for real–data simulation. The WPS module defines the nested domains; computes latitude, longitude, map scale factors, and Coriolis parameters at every grid point; and interpolates time–invariant terrestrial data to the simulation grids (e.g. terrain height, soil type, land-use). WPS calls on three sub-modules that are dedicated to specific tasks: GEOGRID, UNGRID, and METGRID (Fig. 2.2). At the end, a file is generated for each domain of all the meteorological and geographical information needed to proceed.

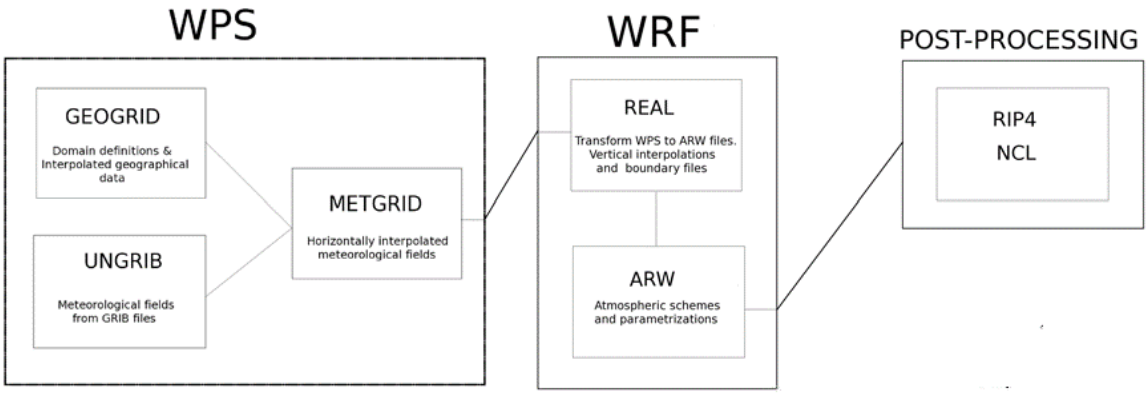

Figure 2.2: WRF model architecture of pre-processing modules (WPS), main model (WRF), and post processing modules (Mazon *et al.*, 2014).

GEOGRID is an acronym for GEO-graphical-GRID. This sun-module defines the map projection, geographical location, and domain dimensions; it evaluates static (time-invariant) fields, latitudes, longitudes, map scale factors, and Coriolis parameters at individual grid points, and interpolates static terrestrial data: topography height, land use, soil type, vegetation fraction, monthly surface albedo. UNGRIB comprises a World Meteorological Organization file format for storing regularly–distributed fields (Generated Regularly-distributed Information in Binary, GRIB). UNGRIB reads GRIB files and extracts meteorological fields - if necessary, it derives and extrapolates required fields from source data (e.g. relative humidity from temperature, pressure, and specific humidity). GEOGRIB and UNGRIB operate independently, outputting to METGRID that

horizontally interpolates meteorological data (extracted by UNGRIB) and adapts it to the domains defined by GEOGRID.

Vertical interpolation to WRF η–levels is performed in the second stage via the REAL submodule, which creates a boundary and initial condition files fed to the model itself. The WRF module (REAL and ARW submodules) offers various options for atmospheric schemes (such as boundary layer dynamics, microphysics, cloud formations, physical interactions, surface fluxes, radiation, and soil) that users can modify according to the meteorological event to be simulated.

At the end of the simulation, RIP4 is used for plotting and extracting parameter values. The main parameters used in our work are the potential temperature, 2-m temperature, wind field, sensible heat flux, latent heat flux, relative humidity, air pressure at 1000 hPa, and solar radiation.

2.7.2 Model setup

The WRF model is used to obtain the evolution of pressure, temperature, wind field, and surface fluxes on the days surrounding the event (Skamarock *et al.*, 2008). We define three nested domains with 18 km, 6 km, and 2 km horizontal resolution (Fig. 2.3). The smallest domain is centered over the general area of individual extreme events, covering a total of 152 × 152 km^2. In the vertical, 45 η-vertical levels are defined. We use the MRF scheme for parameterizing the planetary boundary layer (Hong & Pan, 1996), the RRTM scheme for modelling longwave radiation (Mlawer *et al.*, 1997), the MM5 shortwave scheme for modelling shortwave radiation (Dudhia, 1989), the WSM 3-class scheme for microphysics parameterization (Hong *et al.*, 2004), and the Noah land surface model (Chen and Dudhia, 2001). No cloud parameterization is used for the smallest domain, as the horizontal resolution is lower than 3 km. Initial and boundary conditions were updated every 6 hours with information obtained from the operational ECMWF model

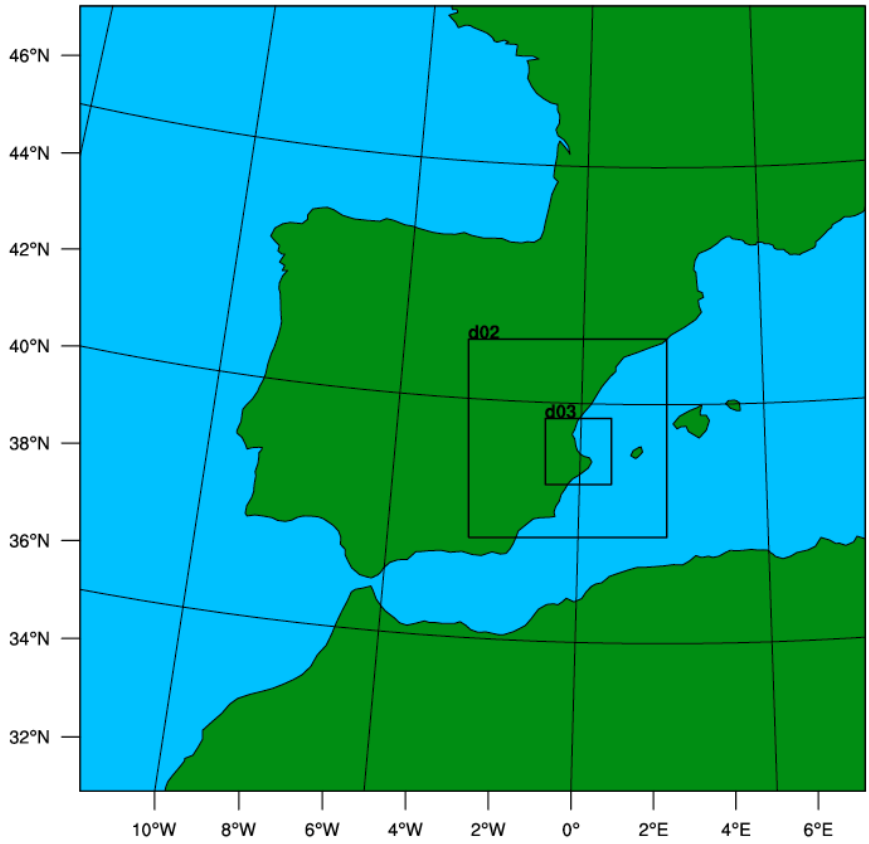

Figure 2.3: Nested domains defined in the WRF-ARW numerical simulations.

Chapter 3

Chapter 3

Hot and cold extreme temperature events on the Iberian Peninsula

3.1. Introduction

The Iberian Peninsula (IP) is one of the European areas where the projections show a large change in temperature. Different studies show that these changes have already begun to happen. Dankers and Hiederer (2008) concluded that there is an increase in the daily mean temperature over most European regions, especially in the IP and the Alps. Some authors have analysed the trends of mean temperatures in the IP (Del Río *et al.*, 2011; Serra et al, 2001; Brunet *et al.*, 2007). However, little research has been conducted so far on extreme temperatures. Regarding this, the work of Fernández-Montes *et al.* (2013) analysed extreme temperatures in the IP in relation to circulation types. They concluded that the detected decrease in spring cold nights could be attributable to a decrease in the frequency of the northerly flows and that the increase in summer warm nights in the Southern regions may be due to uptrends in the Iberian thermal low and North Atlantic anticyclones. Furió and Meneu (2010) studied the statistical behaviour of extreme temperature values in four Spanish sites, concluding that the maxima (minima) temperatures are becoming more (less) extreme, and that, in general terms, the daily temperature range decreased over the twentieth century. Brunet *et al.* (2007) studied the annual changes of maximum, minimum and mean temperatures over Spain from 1901 to 2005 and they found general and highly significant warming on an annual and seasonal basis over the entire period for the three daily temperature variables. In the same study, estimated trends in the number of moderately extreme cold days (Tmax < 10^{th} percentile) and moderately extreme cold nights (Tmin < 10^{th} percentile) showed significant reductions of, respectively, 0.74 and 0.54 days/decade. A regional study for southern Spain corroborates that maximum temperatures have increased along with the number of warm days and nights during the second half of the 20th century, particularly in summer (Castro-Díez *et al.*, 2007).

Extended periods of cold temperatures in Europe during winter are generally of dynamic origin (Cattiaux *et al*., 2012). High-pressure anomalies over the Arctic and low pressure over the European continent induce the advection of cold air from the north or the northeast towards lower latitudes (Tomassini *et al.*, 2012; Horton *et al*., 2015). In Peninsular Spain, an analysis (Prieto *et al.*, 2004) based on an objective detection scheme was applied to 45 stations for the period 1955-1998, and it revealed that most of the temperature extremes occurred under six synoptic patterns. However, they note that the role of synoptic processes was limited: they provide favourable conditions for its occurrence, but do not completely determine it. The study also detected a shift towards higher mean values in the distribution of minimum daily temperatures.

Because of the intense surface heating over land, a near stationary thermal low is produced in the IP mostly during the summer months reaching its maximum intensity during the afternoon and then weakening during the night (Hoinka and Castro, 2003). The physical process that generates the Iberian thermal low is the vertical expansion of the lowest layers of the atmosphere as a result of convective heating, which produces divergence above these layers (Hoinka and Castro, 2003). Strong pressure gradients develop at the boundary of the low, causing low-level winds that blow from the coastal areas towards the interior of the IP (Millán *et al*., 1991).

Extreme temperatures in western Europe can be induced by extreme phases of the climatic indices. In the IP, NAO, AO and WeMO are the most influencing (Pfahl and Wernli, 2012; Martín-Vide and López-Bustins, 2006; Vicente-Serrano *et al*., 2009). NAO has been identified as one of the atmospheric patterns which mostly influence the temporal evolution of precipitation and temperature in the Mediterranean area. More recently, WeMO has also been proposed to describe the precipitation variability in the eastern Iberian Peninsula. Some studies deal with the influence of these climatic indices on the atmospheric routes and its influence on the rain chemistry in IP. Izquierdo *et al.* (2014) found a more relevant role of the WeMO compared to NAO in the deposition of either marine or anthropogenic pollutants related to the fact that the negative phase of WeMO causes the entry of air masses from the Mediterranean into the IP, that are enriched with marine ions and ions of anthropogenic origin coming from southern Europe. However, little research has been done so far on the influence of teleconnection patterns on extreme temperatures.

This chapter focuses on the study of extreme hot and cold episodes in the Iberian Peninsula for the 20-year period 1994-2013, based on the 12-hourly maximum/minimum 2-m temperatures from the ERA-Interim reanalysis data (ECMWF). The conductive meteorological conditions have been characterized by means of: 1) a Lagrangian approach to determine the air-mass pathways; 2) the study of the correlations with the main teleconnection patterns; 3) the study of the evolution of the physical variables along the atmospheric trajectories; and 4) the identification of the synoptic situations by Principal Component Analysis of the pressure and geopotential fields.

3.2. Results and discussion

3.2.1. Annual distribution, duration and correlation with climatic indices

Figure 3.1 shows the average of extreme temperatures at each grid point. This spatial distribution reflects the strong influence of the three main geographical factors in IP: orography, sea proximity and latitudinal difference. The highest values for the hot events corresponded to the SW region and the lowest ones to the NE one (Pyrenees), with a difference between them of about 8 K inside the continent and 20 K in the whole domain. Regarding the cold events, a latitudinal gradient of 22 K can be observed from the northeast to the southwest, with the lowest values in the Pyrenees.

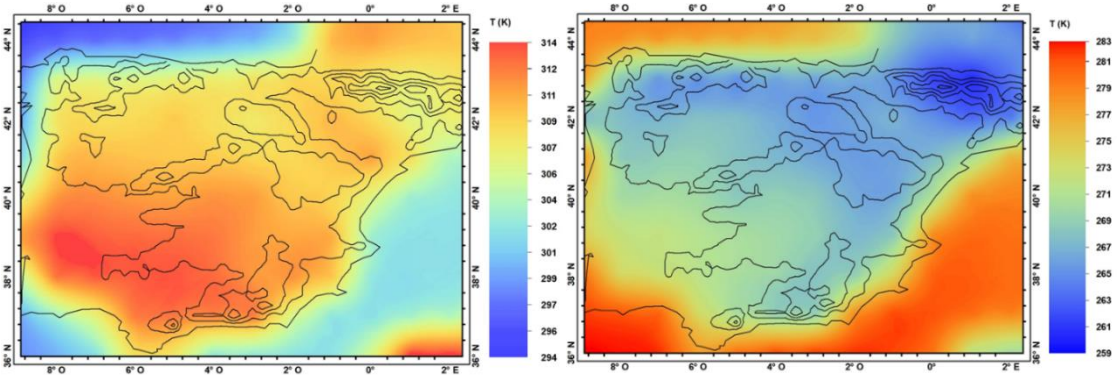

Figure 3.1: Geographical distribution in IP of the average extreme temperatures for the 20-year, the black lines represent the mountains in IP

Figure 3.2 indicates the temporal evolution of the number of events with durations of one day, two days, and three or more days, specifically those that are: (a) hot nocturnal (03:00 UTC) events, (b) hot diurnal (15:00 UTC) events, (c) cold nocturnal events and (d) cold diurnal events, with the trend lines also represented. Regarding the hot events, two periods can be distinguished: from 1996 to 2002 only 19% of events occurred, while the second half of the period (2003-2013) registered 81%. The year 2003 registered the highest

number (30%). Regarding the cold events, the 10 first years of the period registered only 28% of the events, while the second half of the period comprised 72%. The year 2005 registered the highest number of cold events, representing 21% of the total, followed by 2012 with 20%.

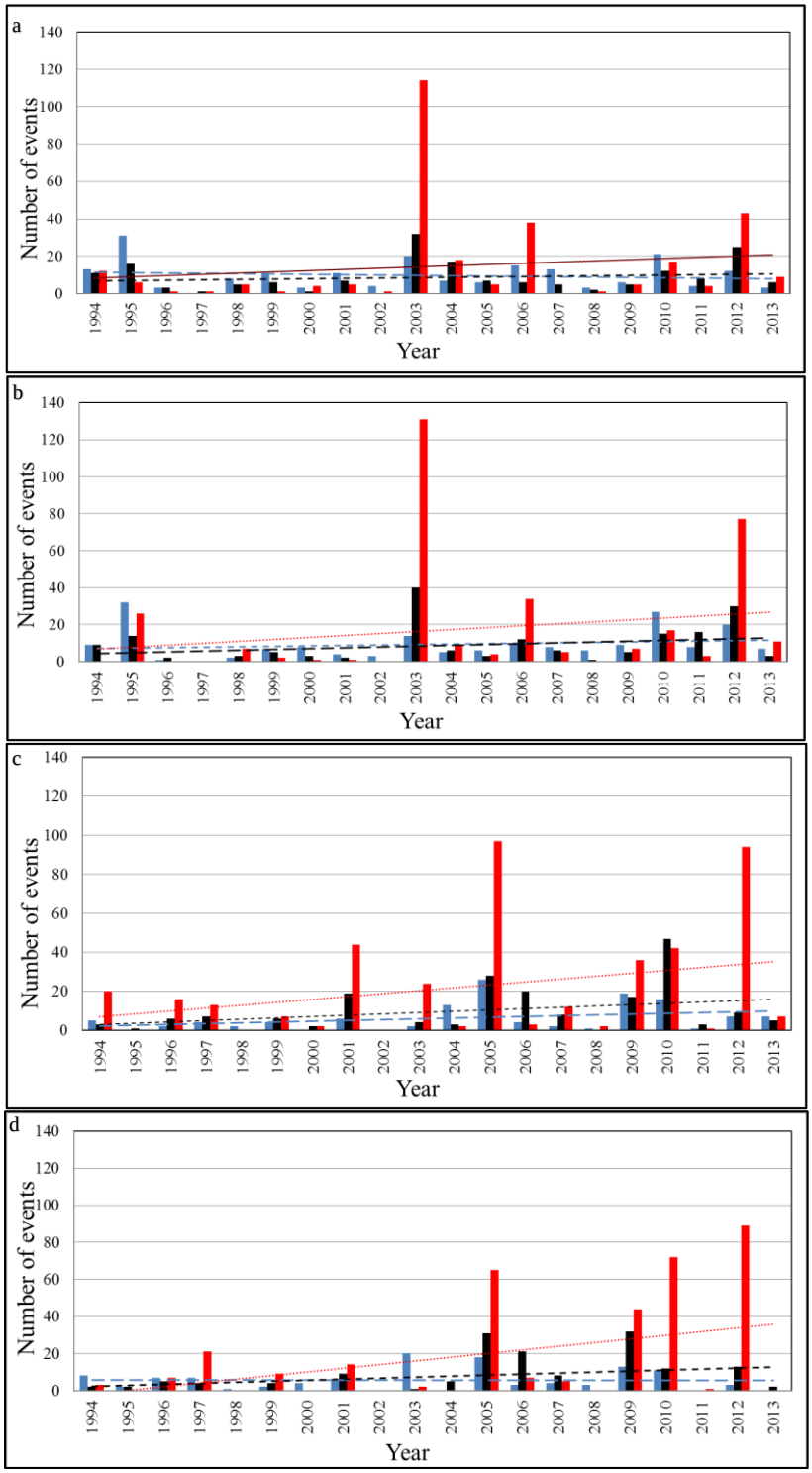

Figure.3 2 :Number of events with durations of one day (blue), two days (black) and three or more days (red) for a) hot nocturnal (03:00 UTC), b) hot diurnal (15:00 UTC), c) cold nocturnal, d) cold diurnal. The dashed lines represent the trend for each duration.

Most of the hot extreme events (80% for nocturnal and 70% for diurnal) persist between one and three days (Fig. 3.3a), with durations of one day being the most frequent. The long-lasting episodes of more than nine days correspond to the extremely hot summer in the year 2003, with the exception of four that occurred in other years. The years 2003, 2010 and 2012 accumulated a total of 20 long-episodes (3 or more days) that affected the Iberian Peninsula in at least 10% of its territory. The temporal trend in the occurrence and persistence of hot events is positive, but not significant. This result is in agreement with that obtained by Brunet *et al.* (2007) for a longer series (the 105-years period 1901-2005) and moderately hot days (T > 90th percentile), in which they obtained a positive significant trend of 0.53 days/decade.

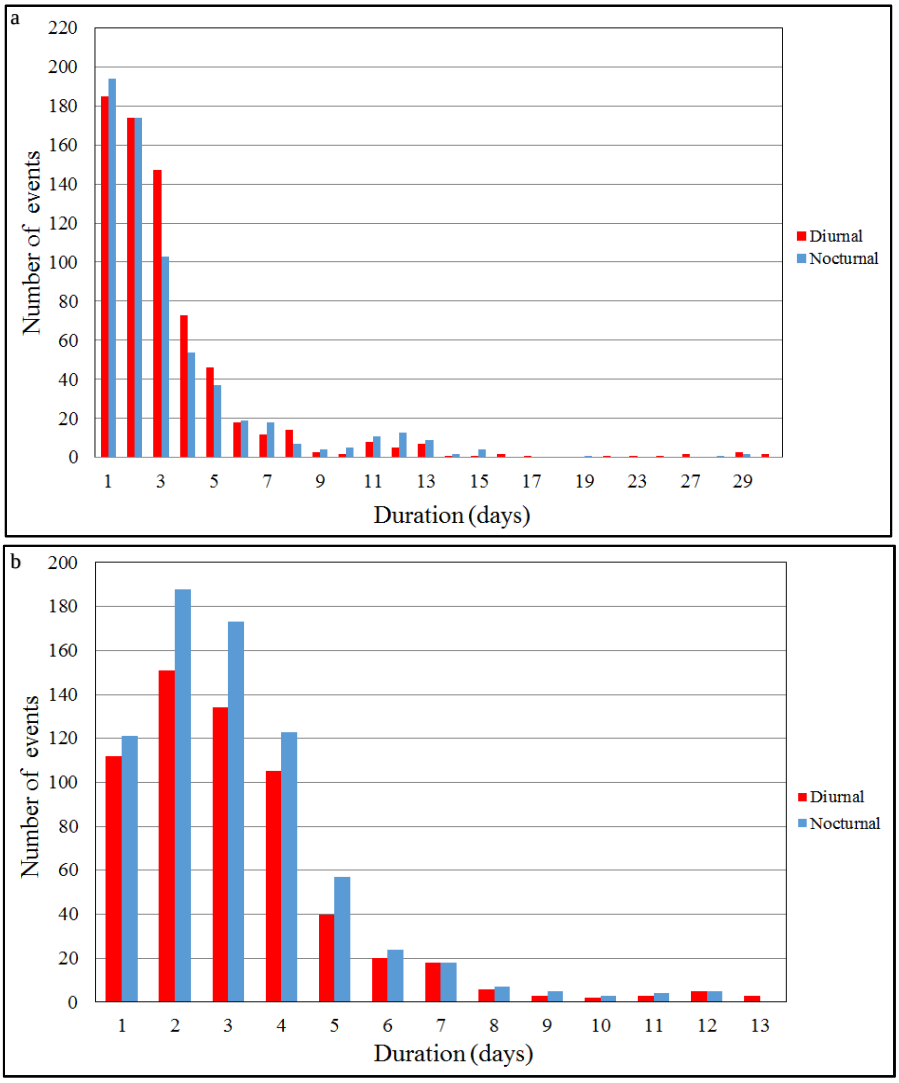

Figure 3.3: Duration of the diurnal (red) and nocturnal (blue): a) extreme hot events and b) extreme cold events.

About 80% of the cold events persisted between one and three days, with 2-day durations being the most frequent, followed by 3-day durations. Episodes of up to 13-day durations

were recorded (Fig. 3.3b), but all the episodes of more than 9 days were registered in 2012, with the exception of two cases. A significant positive trend ($p \leq 0.1$) of 26.1 days/decade (0.2 days/decade per grid point) for diurnal events and 27.6 days/decade (0.21 days/decade per grid point) for nocturnal events has been obtained. The persistence of cold events also shows an increasing trend, intensified in the last years. This upward trend is in consonance with the more general conclusion that there is no apparent trend towards fewer extreme cold events on either continent, which was observed by Walsh *et al*. (2001) for the 1948-1999 record. However, our result differs from the above-mentioned work by Brunet *et al.* (2007), in which a negative trend was obtained in the IP, probably due to the different length of the analysed periods.

The Spearman rank, Kendall's tau and the Pearson's correlation were applied for detecting whether the climatic indices (NAO, AO and WeMO) correlated in any way with the number of extreme events as well as with the annual average extreme temperature for all the grid points. No significant correlations were found between the number of hot days and NAO, AO, WeMO (annual and winter indices) and summer NAO (not shown). On the other hand, a significant positive correlation ($p < 0.01$) was found between the annual average of the extreme hot temperatures and annual WeMO (Kendall: 0.328; Spearman: 0.455).

Regarding the cold events, a significant ($p < 0.01$) negative correlation was found between the number of cold days and the annual indices for NAO (Kendall: -0.345; Spearman: -0.502; Pearson: -0.429) and AO (Pearson: -0.415). However, no correlation was found with WeMO. On the other hand, neither were any significant correlations found between the annual indices and the annual average of the extreme cold temperatures. Several studies have focused on the influence of climatic indices in precipitation over the IP; however, little has been done so far with temperatures and extreme temperatures. Nevertheless, due to the fact that NAO modulates the intensity of westerlies into Europe, negative values of the NAO index have been considered as features common to European cold outbreaks (Walsh *et al.*, 2001). According to our results, the number of days with extreme cold temperatures in the IP would decrease (increase) in years with positive (negative) phases of NAO or AO. This is in concordance with the lower cyclone frequency, less cloud cover and, therefore, the greater insolation in the western Mediterranean region that is attributed to a positive NAO phase (Hurrell *et al.,* 2013). This is also in accordance with the result obtained for hot events showing higher (lower) extreme temperatures in years with a positive (negative) WeMO phase,

since WeMO affects the region in a similar way as NAO and AO. On the other hand, our results would differ from those of Rodrigo (2015), in which a significant increase in minimum winter temperatures under the negative phase of the NAO was found for the period 1956-2005. They explained this as a result of lower radiative cooling during the NAO negative phase resulting from greater cloudiness. On the other hand, El Kenawy *et al.* (2013) found a significant relationship between the negative phase of WeMO and maximum temperatures during the warm season in the north-eastern region of the IP for the period 1920-2006, In contrast, they did not find any significant correlation for minimum winter temperatures. This disagreement with our results could be due to the different length of the analysed period and the fact that they focused on a specific region of the IP.

3.2.2. Trajectory densities

Back-trajectories were computed, with origins on the grid points at the time of episode onset. The results indicate that cold-event trajectories were faster than those of hot events. With a median of 772 km at 100 m and 1250 km at 1500 m a.s.l., the travel distances of the trajectories four days before the hot events are clearly less than the corresponding median distances of 2476 km and 2665 km, respectively, of the cold events. These differences also exist ten days before the episodes, with a median of 2255 km at 100 m and 2600 km at 1500 m a.s.l. for hot events, while for cold events they are, respectively, 4315 km and 4357 km.

The pathway pattern and source regions associated with the air masses responsible for extreme events were analysed by superimposing a grid mesh of 1ºx1º over the integration domain of the back-trajectories and by computing the trajectory densities, i.e., the number of back-trajectory time steps per grid box (1º×1º). Densities were computed for 4-day and 10-day length back-trajectories at 100 m and 1500 m a.s.l. The 4-day length results are shown in Fig. 3.4. No important meridional advection involving the production of hot extremes is observed. At 100 m (Fig. 3.4a), the densities have a more marked Mediterranean component than at 1500 m (Fig. 3.4b), in which the densities are higher in the SW region of the IP. In general, most of the trajectories at the two levels remain within the IP region and its nearby surroundings during the days prior to the hot events,

indicating that the local recirculation of warm air masses is mainly responsible for the high temperatures rather than the occasional entrance of North African air masses.

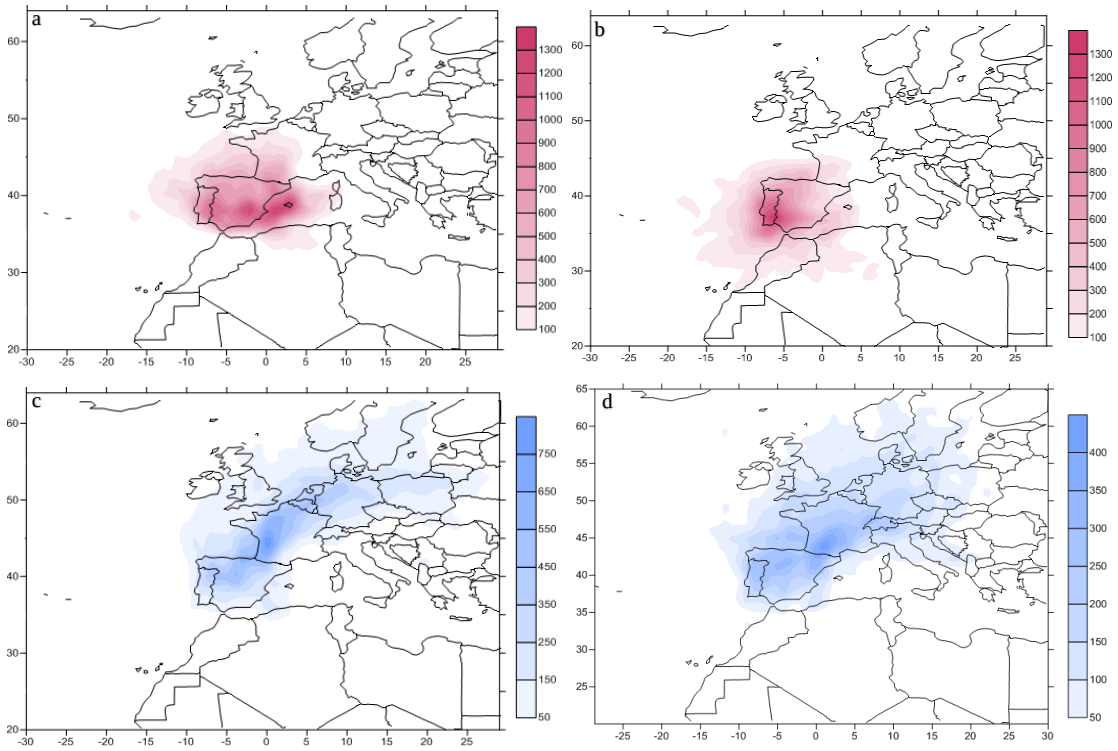

Figure 3.4: Trajectory density patterns (number of one-hour time-steps per grid box) for extreme hot events of 4 days at a) 100 m, b) 1500 m, and for extreme cold events of 4 days at c) 100 m, d) 1500 m.

The density map obtained for 10-day lengths is very similar (Figs. 3.5 a and b). Other studies (Millán *et al.*, 1997; Jorba *et al.*, 2004; Izquierdo *et al.*, 2015), regarding the seasonal patterns of the atmospheric regimes in the IP, showed similar results, which agree on the occurrence of predominantly slow-moving recirculation flows from the W and SW in summer.

The meridional and zonal displacements at 100 m can be better appreciated in Fig. 3.6, where the differences between the latitude and longitude at the origin and in the different time steps are represented for the median, the upper and lower quartiles, and the 5th and 95th percentiles. A latitudinal decrease of about 5 K is observed for the median, as well as a longitudinal decrease from west to east of 20 K (Figs. 3.6a and b).

The extreme cold events are principally associated with a north-eastern advection of air masses from central and northern Europe. Figures 3.4c and d show the 4-day length trajectory densities at 100 m and 1500 m a.s.l. As in the case of hot events, the distribution

of densities is similar to those of a 10-day length, which is shown in Figs. 3.5c and d. These figures indicate that the main flow through the NW European Atlantic coast comes from the Baltic regions at low levels while it has a more southerly component at high levels. The meridional and zonal displacements of the cold air masses along the trajectories are in general greater than for the hot air masses. Figures 3.6c and d represent the median, the upper and lower quartiles, and the 5th and 95th percentiles of the differences between the latitude and longitude at each time step and their respective origin values, at 100 m a.s.l. The longitudinal (from east to west) and latitudinal (from north to south) differences for the median are about 20 K in the 10 days of the back-trajectories, indicating an advection of cold air masses from the Arctic and Scandinavia. The latitudinal shift is produced mainly in the four days before the cold events. This result is consistent with situations in which large 'blocking' anticyclones over Scandinavia and north-western Russia drive easterly winds over Europe, which has been identified as an important synoptic-scale cause of winter cold spells (Cattiaux *et al.*, 2010; Sillmann *et al.*, 2011; Andrade *et al.*, 2012; Croci-Maspoli *et al.*, 2007).

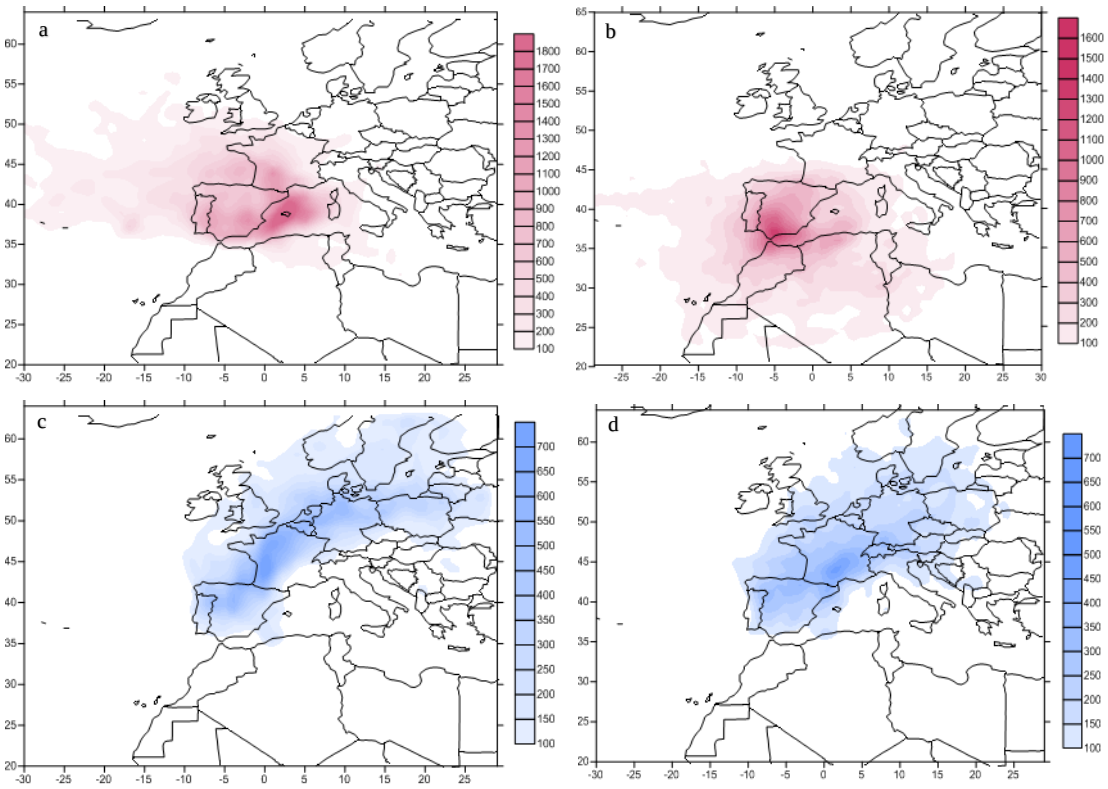

Figure 3.5: Trajectory density patterns (number of one-hour time-steps per grid box) for extreme hot events of 10 days at a) 100 m, b) 1500 m, and for extreme cold events of 10 days at c) 100 m, d) 1500 m.

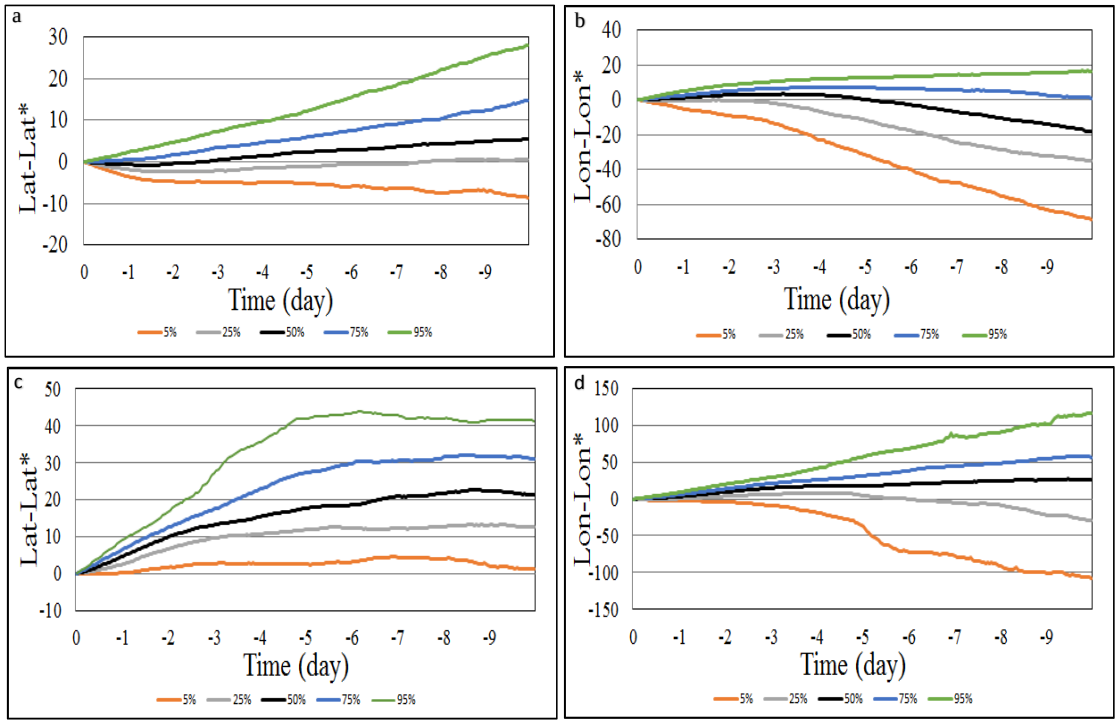

Figure 3.6: Meridional and zonal movement corresponding to the 100 m back-trajectories of the air masses causing hot (a and b, respectively) and cold (c and d) extreme events in the IP, in terms of differences regarding latitude and longitude at event origin (lat* and lon*). Black lines represent the median; grey and blue correspond to the upper and lower quartiles; and orange and green to the 5th and 95th percentiles, respectively.

3.2.3. Evolution of the physical variables for hot events

The evolution of the physical variables has been analysed along the 100 m height back-trajectories. As in the previous section, temperature and potential temperature are represented by the median, the upper and lower quartiles and the 5th and 95th percentiles of the differences between the values of the variables at each time step and their values at the time the extreme events were produced. Mixing-layer height, relative humidity and downward solar radiation have also been evaluated.

The analysis of the evolution of the temperature (T, Fig. 3.7a) shows that there was a steady warming of the air mass along the trajectories, with a diurnal cycle that was more pronounced during the three days before the extremes. The temperature difference for the median in the ten days was about 15 K. The evolution of the potential temperature (θ, Fig. 3.7b) was similar, indicating that there was diabatic heating of the air mass due to the absorption of sensible heat from the ground on days of intense solar radiation. Figure 3.7c represents the evolution of the height, T and θ for the median, where we can clearly see the parallel evolution and strong diurnal heating during the three days prior to the

onset, during which the air mass recirculates above the IP, and thus leads to in-situ heating due to the absorption of sensible heat from the ground.

The mixing-layer height (Fig. 3.7d) remains near constant throughout the greater part of the path. However, in the three days leading up to the hot events, there is a progressive increase in its height and its diurnal cycle, indicating the greatest convection when the air mass enters the IP, three days prior to the events for the 95th percentile and one day prior for the median.

The evolution of relative humidity (Fig. 3.7e) shows stable high values from days 10 to 7 before the onset of the extremes (median of near 80%) and a progressive decrease from day 6, which is more accentuated in the two days prior to the warm events when the air mass enters the IP and its humidity drastically drops to median values of 30-55%. In accordance with back-trajectory densities, this suggests a maritime origin of the air mass and a prolonged stay above the sea in the West Mediterranean, Alboran Sea and Atlantic Ocean near Gibraltar, all of which probably favour sea/land-breeze development. Recirculation induced by the breeze occurs when air is carried landward by the sea breeze during daylight hours and seaward by the land breeze at night. If the coastal zone is a region of significant relative relief, as in the IP, topographically forced circulations interact with sea/land-breeze circulations to further obstruct large-scale air mass advection. In this case, the air mass advected shoreward by the sea breeze is eventually caught in upslope flows that enhance the sea-breeze strength. Breeze recirculation times are on the order of 24 hours with a horizontal scale of approximately 130 km (Steyn, 1998). However, the spatial extent and intensity of the episodes can be reinforced by the diurnal development of the Iberian thermal low. A quasi-steady downward solar radiation flux along the back-trajectories occurs (Fig. 3.7f), and this can be explained by the proximity between the regions that are crossed by the air masses.

In summary, the trajectory densities and the evolution of the physical variables indicate that the production of hot episodes is due to progressive warming caused by air masses of long residence times over the IP during recirculation processes on summer days of weak baric gradient, rather than Saharan dry and warm air masses entering the IP from North Africa, which play a secondary role in producing hot extremes.

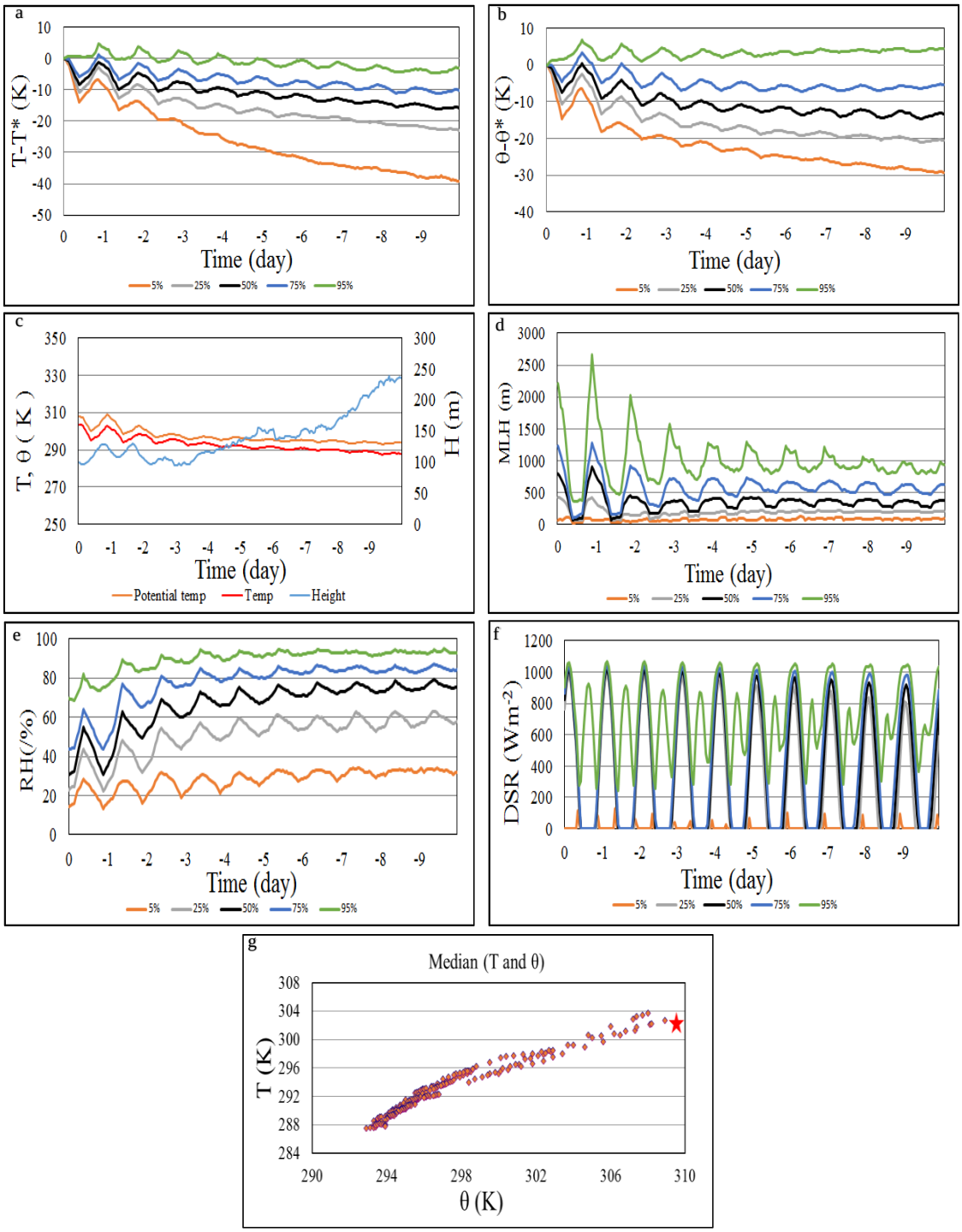

Figure 3.7 (cont): Evolution along the back-trajectories of hot events at 100 m of a) temperature and b) potential temperature for hot extremes in terms of differences regarding the temperature and potential temperature at the origin. c) Evolution of the median values of potential temperature (θ, in orange), temperature (T, in red) and height (H, in blue) for hot extremes. d) Evolution of the mixing-layer depthe) relative humidity; and f) downward solar radiation for hot extremes. g) Adiabatic and diabatic temperature change for hot extremes where each point represents the T and θ median of the set of trajectories at each specific time step. The star indicates the values at time step 0. Colors in e) and f) as in Fig. 3.6.

3.2.4. Evolution of the physical variables for cold events

The temperature increases progressively along the trajectories during cold events, with a difference in the median of about 15 K over ten days (Fig. 3.8a). The behaviour of the median potential temperature (Fig. 3.8b) is different in two ways. First, it shows radiative cooling of about 5 K from days 10 to 3 before the extremes, when the air mass crosses Scandinavia and northern Europe; and, second, diabatic warming of about 3 K occurs in the three days prior to the events. The evolution of the median for height, temperature and potential temperature is represented in Fig. 3.8c, where it can be seen more clearly that the subsidence causes adiabatic heating by means of air mass compression. The warming is accentuated in the 2 or 3 days prior to the extremes, when the potential temperature also increases, suggesting diabatic heating of the air mass during its passage over the IP or its surrounding oceanic waters. Subsidence of several hundred hPa has been described as typical for trajectories of the coldest air that reach the surface in Europe's affected regions, with the source regions being over northern Asia (Walsh *et al*., 2001; Pfahl and Wernli, 2012). In our study, a median subsidence of 150 hPa has been obtained for the 10-day back-trajectories (not shown). This indicates that the air near the surface would have been even colder than it was if it were not for the adiabatic warming associated with the subsidence.The evolution of the mixing-layer height shows (Fig. 3.8d) a less marked diurnal cycle than in the warm extremes. From days 10 to 5 before the extreme, this oscillation is almost imperceptible for the median and becomes more accentuated three days prior to the events. The general trend is positive, showing an almost continuous increase from the start of the trajectories ten days before the events. Lower values occur over northern Europe, which is associated with high latitudes and the influence of the cold north Atlantic waters, whereas higher values occur when the air mass travels over the IP due to the high topography and low soil moisture.

Relative humidity shows (Fig. 3.8e) moderate values. There is a slight increase in the two first days of the path (days 10 and 9 before the events), which is probably due to contact with the Baltic and North Atlantic Ocean. In addition, the values remain almost constant

in the central part of the path, where the air mass crosses continental Europe, followed by a new increase on the day prior to the extremes.

In contrast with hot events, the downward solar radiation flux for cold events (Fig. 3.8f) exhibited low values, namely zero in the case of the median for days 10 and 9 before progressively increasing as the back-trajectories approached the IP, thus reflecting the high latitudes of origin for these air masses.

The evolution of the physical variables along the back-trajectories indicates that the production of cold events is driven by mechanisms that are different from those driving hot ones. Air mass advection from northern European regions is the main process. The diabatic and adiabatic changes in temperature are represented through the evolution of T vs. θ for the median. The hot events (Fig. 3.7g) show progressive diabatic warming, which becomes more pronounced 3 days before onset (as indicated by the greater separation between points), with a total increase of 16 K along the path. Regarding the cold events, Fig. 3.8g shows diabatic radiative cooling with a decrease of about 4 K in the potential temperature during the first days of the path, when the air mass crosses the high latitude regions. Along this first part of the path, there is also adiabatic warming by subsidence of the air mass, with a final balance of +6 K. In the three days prior to onset, the adiabatic warming by subsidence continues and is still more pronounced, but it is also accompanied by a diabatic contribution of nearly 5 K as the air mass approaches the IP. The total temperature change in the median over these 10 days is +16 K. The westward migration of the European cold air masses has already been related (Walsh *et al*., 2001; Pfahl and Wernli, 2012) to the intensity of the eastward airflow reaching Europe from the North Atlantic, and the NAO index is a natural measure of this intensity.

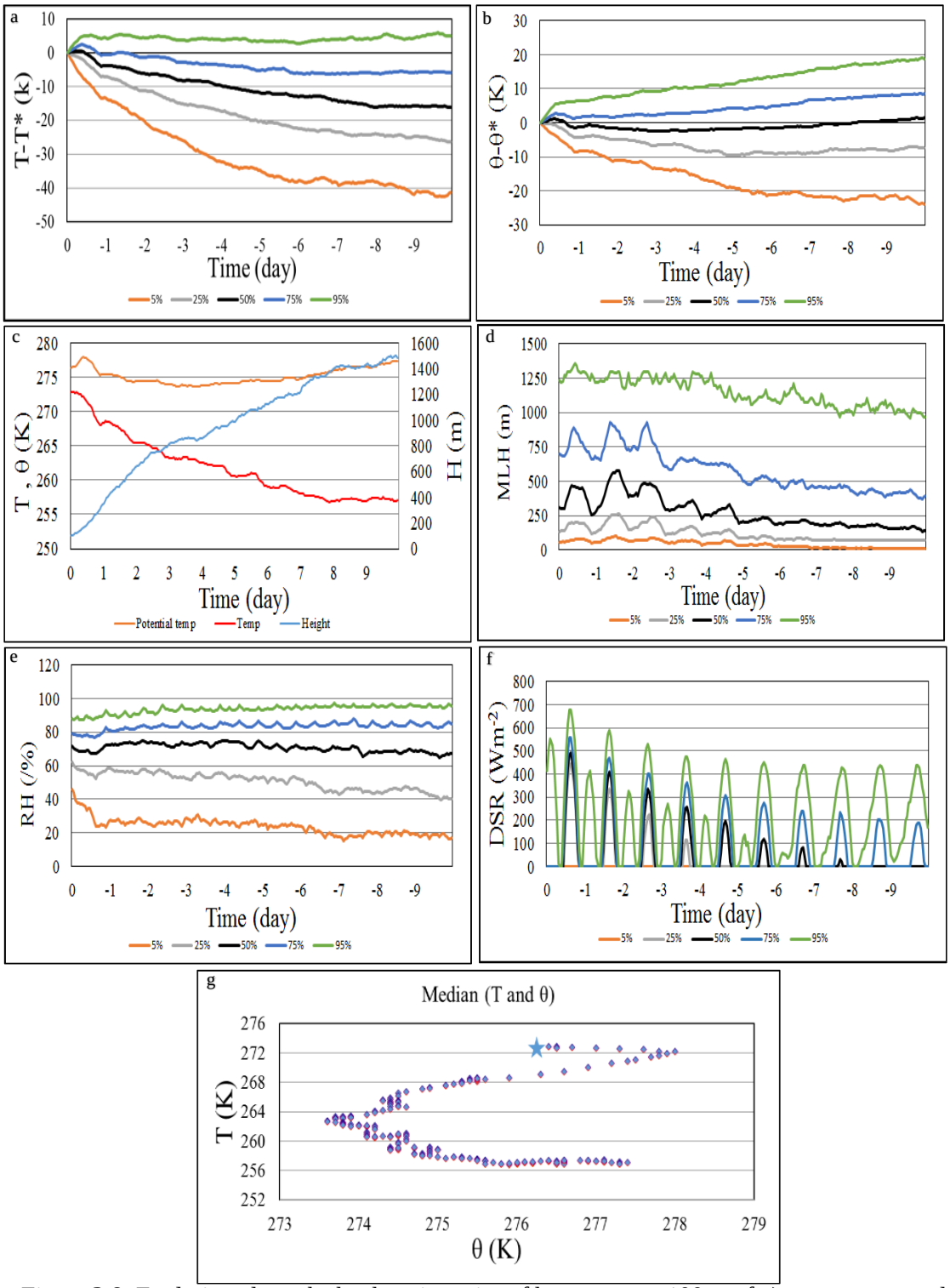

Figure 3.8: Evolution along the back-trajectories of hot events at 100 m of a) temperature and b) potential temperature for hot extremes in terms of differences regarding the temperature and potential temperature at the origin. c) Evolution of the median values of θ (orange line), T, (red line) and height (H, blue line) for hot extremes, d) Evolution of the mixing-layer depth and e) relative humidity; f) downward solar radiation for hot extremes. g) Adiabatic and diabatic temperature change for cold extremes where each point represents the T and θ median of the set of trajectories at each specific time step. The star indicates the values at time step 0. Colors in a) b) d) e) and f) as in Fig. 3.6.

3.2.5. Synoptic situation for hot events

3.2.5.1.Principal component analysis

PCA in S-mode gives a spatial regionalization of the main characteristics of the time evolution of a variable (Compagnucci *et al.*, 2001): mean sea level pressure (MSLP)and 850 and 700 hPa geopotential height, in our case. That is, it allows us to first isolate regions of grid-points that covary similarly and, second, to identify regions that are homogeneous in terms of time variability. The first two principal components (PC1 and PC2) that were obtained here in S-mode represent 45% of the total cumulative variance for the MSLP, and 40% and 35%, respectively, for geopotential at 850 hPa and 700 hPa. PC1 (25% of total variance) revealed a strongly positive temporal correlation with the time series of local MSLP in central and southern Europe, extending to the West Mediterranean Sea and North Africa, while there was a weaker negative correlation in the Atlantic Ocean directly off the North African coast (Fig. 3.9a). The PC1 pattern correlations at 850 hPa and 700 hPa (Fig. 3.9b and c) were similar but showed a shift in which the positive correlations displaced southward and the negative to the northeast. The correlation pattern for PC2 (20% of total variance) of MSLP was positive in the North Atlantic Ocean facing France and extending to NW IP, while it was weakly negative in the East Mediterranean Sea and North Africa (Fig. 3.9d). In the second component, the correlation pattern at 850 hPa and 700 hPa showed highly positive correlations in the northern regions and centred in the British Islands, while the correlations were negative in North Africa and the Mediterranean Sea (Figs. 3.9e and f).

In T-mode, PCA analysis determines the main spatial types. The two first principal components obtained for hot events in T-mode represented 70% of the MSLP total variance. The map of the loading values obtained for the first component (Fig. 3.9g) shows a low-pressure system centred over North Africa. Frequent in summer, this system is of thermal origin and displaces the almost permanent North African anticyclone to upper levels (Figs. 3.9h and i), causing a SE circulation in the central Mediterranean and southern IP at low levels. A ridge from the Atlantic anticyclone extends towards central Europe and drives a NW flow over the northern and western regions of the IP, blocking the entrance of Atlantic disturbances to the inner IP and Mediterranean. The Iberian thermal low, shaping up in the average MSLP map (not shown here), remains stationary over the area and increases blockage durations, leading to extreme warm episodes. The second component is related to a blocking situation, demonstrating the simultaneous presence of a deep low-pressure system over the south of Iceland and a high-pressure system over Scandinavia, inducing a null baric gradient in the IP, the Mediterranean Sea

and North Africa (Fig. 3.9j). This same situation is reproduced at 850 and 700 hPa (Figs. 3.9k and l).

The meteorological scenarios indicated by the two first principal components correspond to situations of atmospheric blocking, whose strong linkage with warm temperature extremes over mid latitude regions in the Northern Hemisphere has already been suggested by other authors (Pfahl and Wernli, 2012). These summer blocking situations, characterized by the presence of persistent anticyclonic systems, are associated with subsiding motions and thus clear-sky conditions (Trigo *et al.*, 2004), which enhance daytime solar heating. In the IP, these situations are accompanied by a reduction in precipitation and soil moisture, followed by a subsequent increase in the sensible heat flux from the surface to the atmosphere.

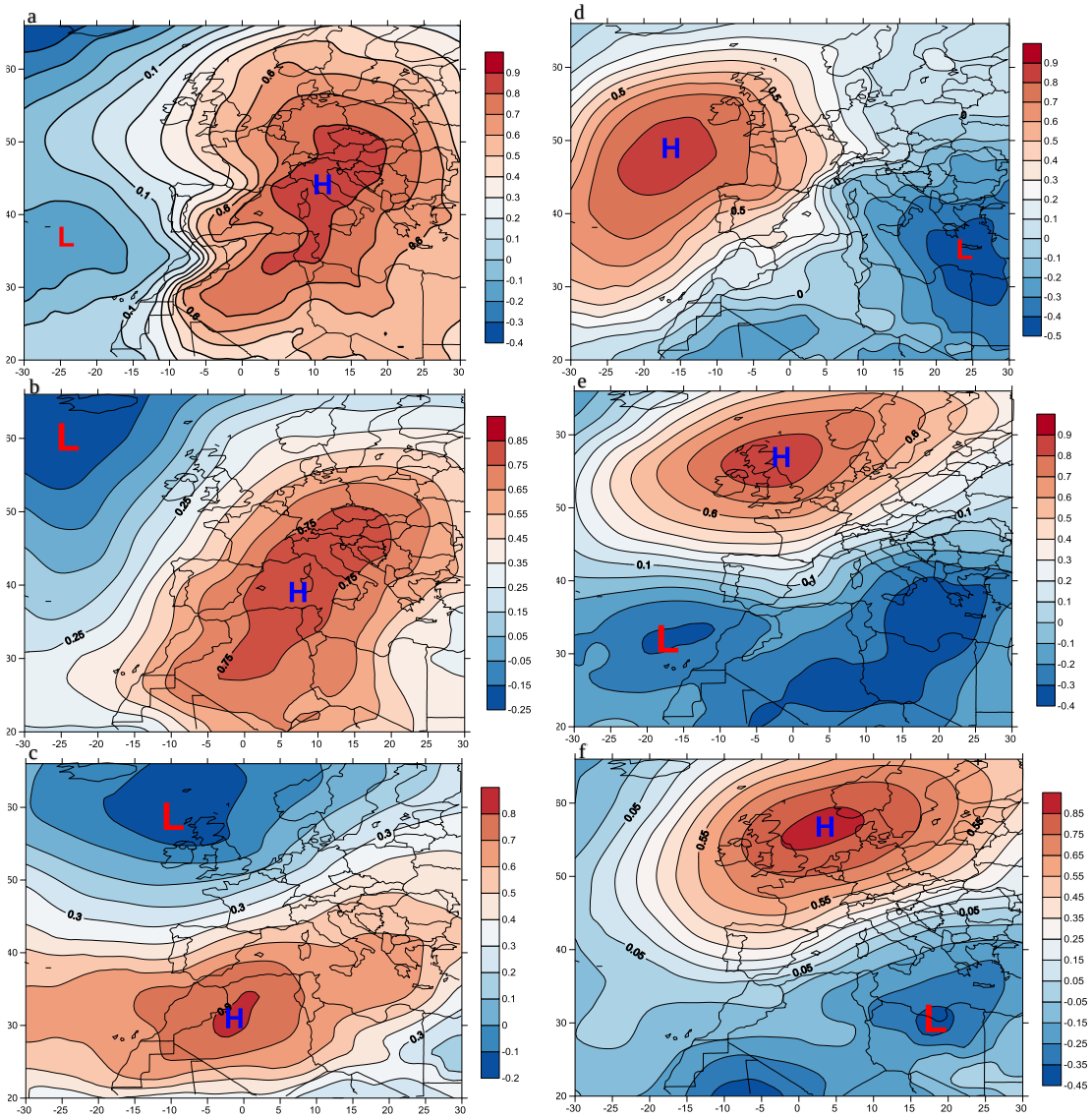

Figure 3.9: Correlation pattern for the hot episodes obtained in the S-mode for a) MSLP, b) geopotential height at 850 hPa, c) geopotential height at 700 hPa, corresponding to the first component (PC1). Correlation patterns obtained in the S-mode for d) mean sea level pressure, e) geopotential height at 850 hPa, f) geopotential height at 700 hPa, corresponding to the second component (PC2).

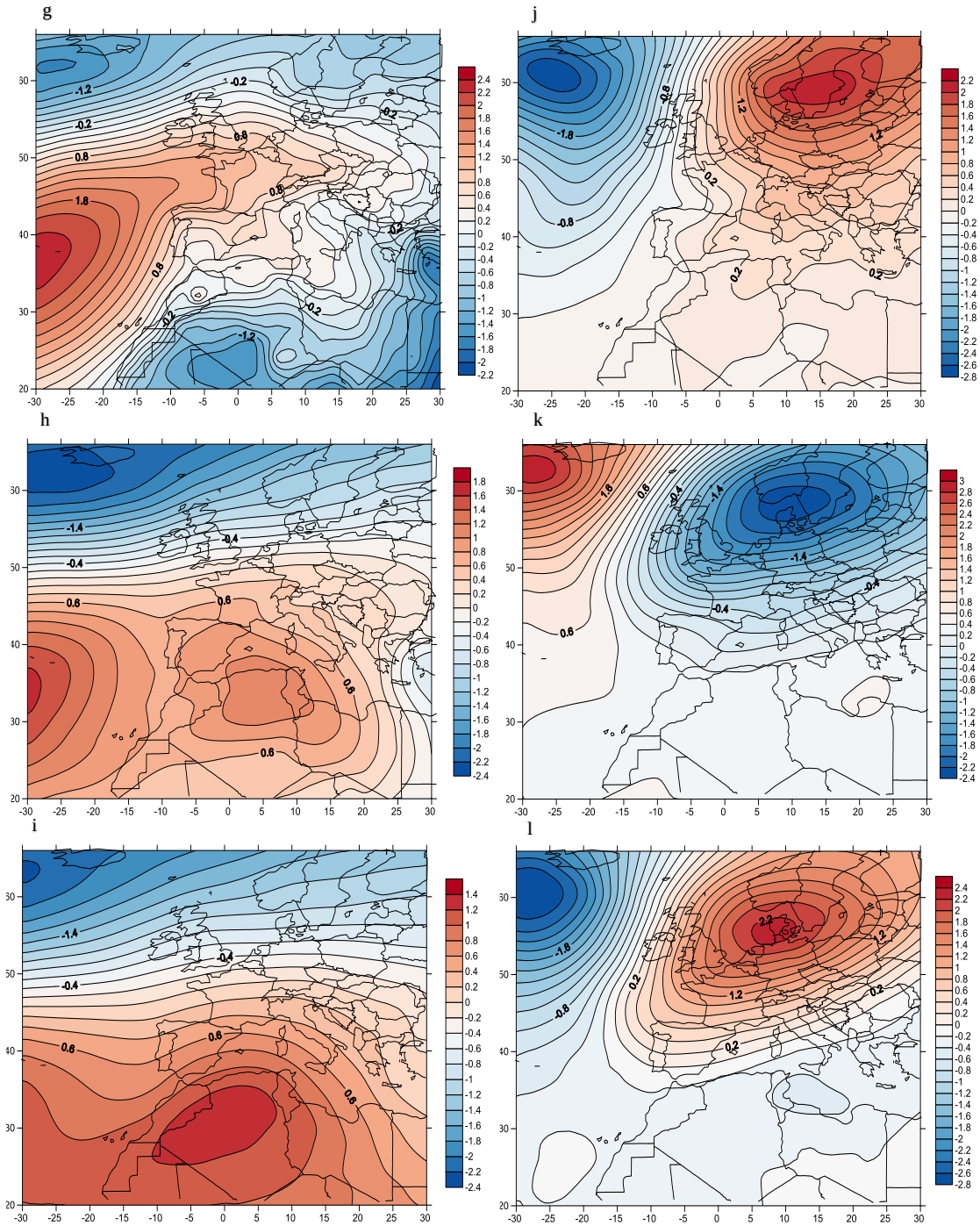

Figure 3.9: (cont.) Loading values in T-mode obtained for PC1: g) MSLP, h) geopotential height at 850 hPa, i) geopotential height at 700 hPa, and PC2: j) mean sea level pressure, k) geopotential height at 850 hPa, l) geopotential height at 700 hPa.

3.2.5.2. Weather regimes

The weather classification based on the Hess-Berezovsky (HB) catalogue (Hess and Brezowsky, 1977; Gerstengarbe *et al.*, 1993, 1999), also known as Grosswetterlangen (GWL) distinguishes 29 different weather types defined from 3 macro-circulation groups: 1) Zonal, 2) Meridional and 3) Mixed. The Zonal circulation is characterized by flows from west to east in low-pressure areas; that is, the wind moves from the east Atlantic Ocean to north continental Europe. The Meridional circulation is characterised by less active winds, producing areas of blockage and barometric swamp situations. Finally, the mixed circulation corresponds to the presence of both types of circulations.

The synoptic situations of the extreme events were classified based on this catalogue, and the results are shown in Table 3.1. Between the three major types, the most abundant corresponded to the Mixed/Central European High macro-circulation group, which constituted a total of 49% of the cases, followed by the Meridional/East at 29% and the Zonal/West at 23%. Among them, the most abundant synoptic type (25%) was the 'Zonal Ridge across Central Europe' (BM) type, belonging to the 'Mixed Circulation/Central European high' major type. BM is characterized by the presence of a ridge over NW Europe, entering from the North Atlantic, at high levels (not shown) and two closed anticyclone systems over West France and Central Europe at low levels (Fig. 3.10a). This produces easterly flows in northern Europe and a stagnant situation over the IP, reinforced by the presence of an anticyclone system in the central North Atlantic. August is the month in which the BM type is most frequent, followed by September and July (total in JAS 31%). The second most abundant type (17%) belongs to the 'West Zonal Circulation' major type, the 'Cyclonic Westerly' (WZ), in which a deep cyclone centred in the North Atlantic between Scandinavia and Iceland produces a westerly flow over NW Europe (Fig. 3.10b), while the IP and the Mediterranean basin are affected by a barometric swamp. WZ situations do not have a marked seasonality, with about 25% of them being produced in summer. The Meridional macro-circulation group represented 28% of the warm situations, but none of the types showed a major presence.

Table 3.1: Classification of the synoptic patterns related to hot events according to the GWL catalogue.

Zonal Circulation/West		
WZ	19	17%
WA	7	6%
Mixed Circulation/Central European High		
HM	4	4%
BM	27	25%
TM	3	3%
SWA	1	1%
SWZ	9	8%
NWA	6	5%
NWZ	3	3%
Meridional Circulation/East		
HB	5	5%
HFA	5	5%
HFZ	2	2%
HNA	2	2%
HNZ	1	1%
NEZ	1	1%
NZ	2	2%
SEA	1	1%
TRM	6	5%
TRW	6	5%

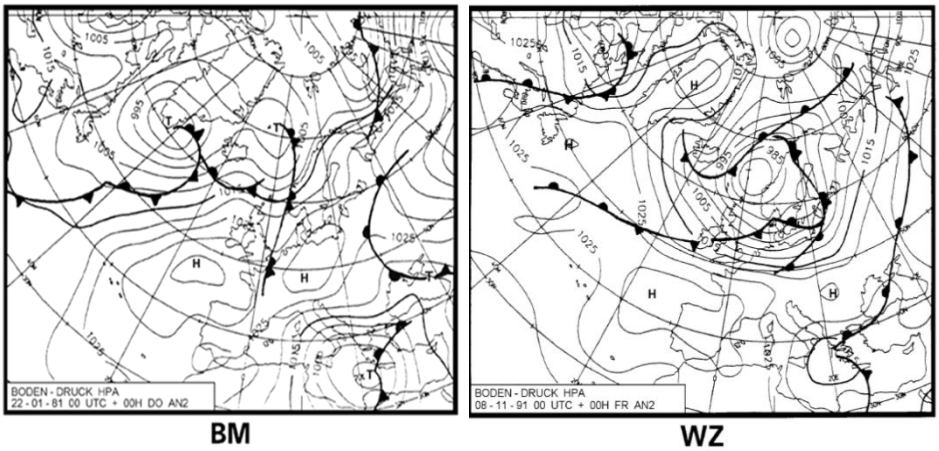

BM WZ

Figure 3.10: Synoptic situation corresponding to 'Zonal Ridge across Central Europe' (BM) type and 'Cyclonic Westerly' (WZ) type, according to the GWL

3.2.6. Synoptic situation for cold events

3.2.6.1. Principal component analysis

The first two PC in S-mode of m.s.l pressure and 850 hPa geopotential represented 51% and 50%, respectively, of the total cumulative variance. At both levels, PC1 (32% and 31% of total variance) revealed a strong positive correlation in the Mediterranean Sea region, encompassing southern Europe and north-western Africa (Figs. 3.11a and b). There were also strong but negative correlations in the North Atlantic Ocean, south of Iceland. A similar configuration showed the correlation map at 700 hPa (Fig. 3.11c). In the second component (PC2), the most positively correlated region was northern Europe (British Islands and Scandinavia), while the region with negative correlations covered North Africa and included the IP, although with low values (Figs. 3.11d, e and f). These two configurations associated with PC1 and PC2 correspond to the two main mechanisms leading to cold spells in the IP: the first one (PC1) affecting southern Europe, Mediterranean regions and northern Africa, and the second one (PC2) affecting central and northern Europe and more tangentially the southern regions. These mechanisms are identified in the following T-mode analysis.

The first and second PC in T-mode represented 50% of the total cumulative variance. The representation of the loading values corresponding to PC1 shows MSLP characterized by the presence of a high system centred over western Europe, inhibiting the westerly flow over the IP and displacing it to higher latitudes (Fig. 3.11g). At 850 hPa a trough appears and becomes more clearly visible at 700 hPa (Figs. 3.11h and i), with its axis crossing central Europe from the northeast to southwest and inducing a northern circulation over the IP. The circulation obtained from the second component (PC2, Figs. 3.11j, k and l) is dominated by a dipole whose centres are in the North Atlantic (south of Iceland) and the Ligurian Sea, generating a north-easterly flow from Scandinavia and Siberia to the IP. The presence of the North Atlantic high-pressure system is in agreement with different works (Walsh *et al.*, 2001; Sillmann *et al.*, 2011; Buehler *et al.*, 2011). These authors suggest a close connection between eastern North Atlantic blocking and cold extremes in Europe, induced by the northerly advection on the eastern flow of the block (Pfahl and Wernli, 2012).

The analysis in T-mode concurs with that of S-mode, indicating that southern Europe and the Mediterranean are the regions more sensitive to Polar air-mass intrusions, while northern, western and central Europe are sensitive to the western Siberian fluxes.

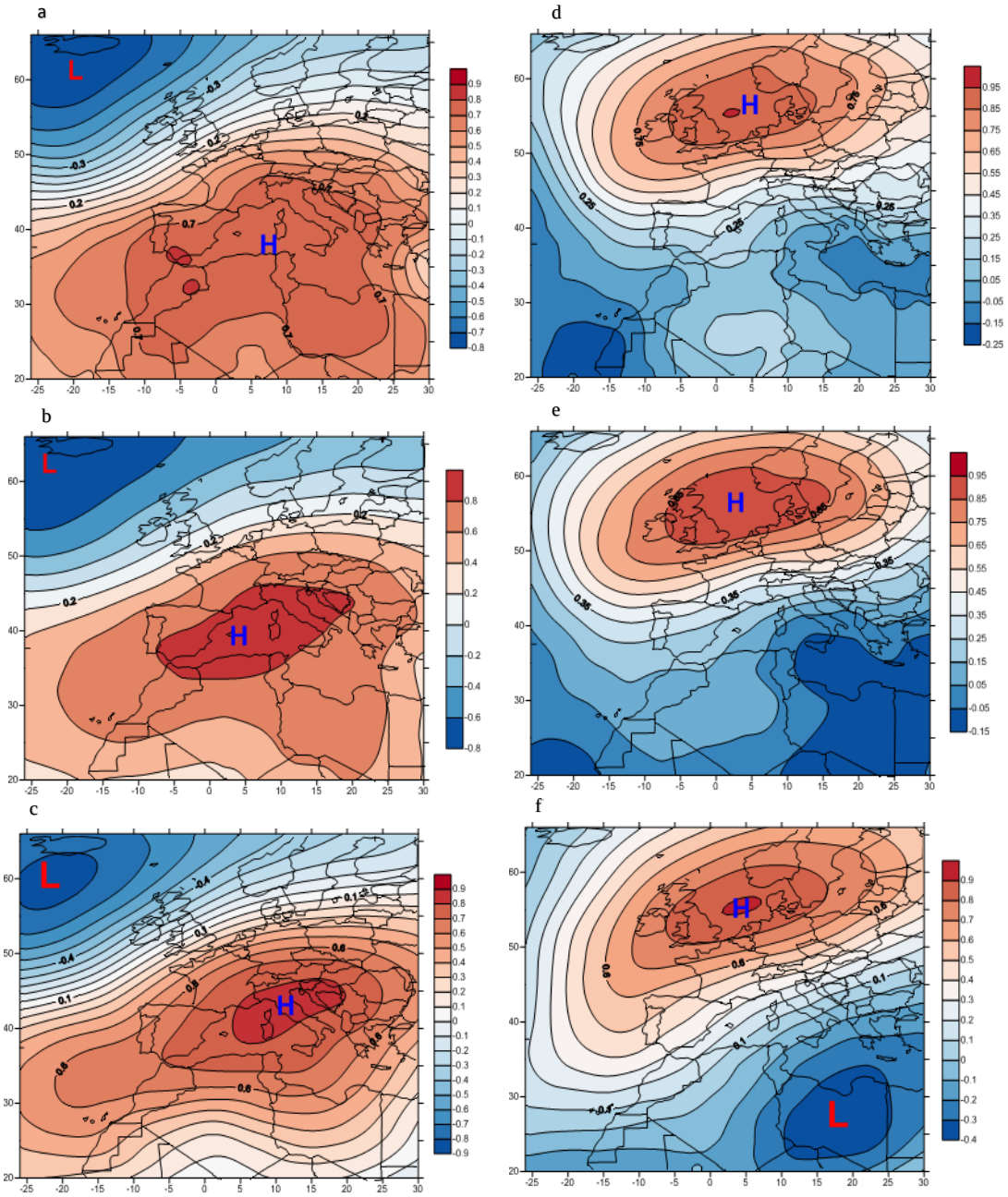

Figure 3.11: Correlation pattern for the hot episodes obtained in the S-mode for a) MSLP, b) geopotential height at 850 hPa, c) geopotential height at 700 hPa, corresponding to the first component (PC1). Correlation patterns obtained in the S-mode for d) mean sea level pressure, e) geopotential height at 850 hPa, f) geopotential height at 700 hPa, corresponding to the second component (PC2).

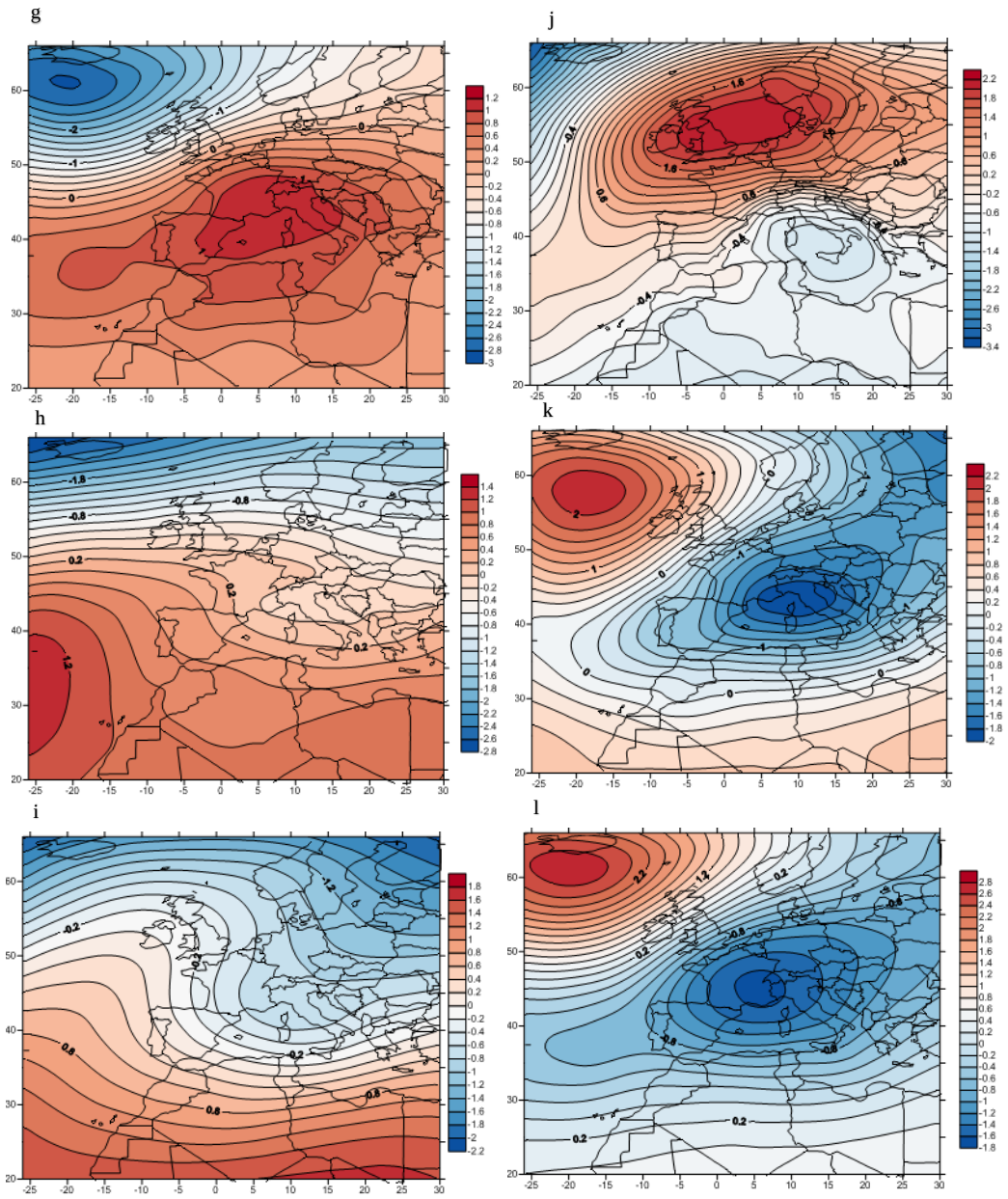

Figure 3.11: (cont.) Loading values in T-mode obtained for PC1: g) MSLP, h) geopotential height at 850 hPa, i) geopotential height at 700 hPa, and PC2: j) mean sea level pressure, k) geopotential height at 850 hPa, l) geopotential height at 700 hPa.

3.2.6.2. Weather regimes

The weather classification based on the Hess-Berezovsky (HB) catalogue showed more than 70% of the synoptic patterns distributed between Meridional (59%) and Mixed (33%) macro-circulation groups, highlighting the Meridional circulation/North 'Central European trough' (TRM) type (22%), and the Mixed circulation 'Zonal Ridge across Central Europe' (BM) type (14%) (Table 3.2). In the TRM type, a trough over Northern and Central Europe is flanked by higher air pressure above the eastern North Atlantic and west Russia (Fig. 12). A frontal zone runs from the north-west to northern France and

southern central Europe, then from there to the northeast. This produces individual disturbances, which are weak over the Mediterranean and stronger over eastern central Europe (Gerstengarbe and Werner, 2010). The BM type is already described in the hot weather regimes.

Table 3.2**:** Classification of the synoptic patterns related to cold events according to the GWL catalogue.

Zonal Circulation West		
WZ	3	5%
WA	4	6%
WW	1	2%
Mixed Circulation Central European High		
HM	3	5%
BM	9	14%
SWA	1	2%
SWZ	2	3%
NWA	2	3%
NWZ	4	6%
Meridional Circulation East		
HB	5	8%
HNA	3	5%
HNFZ	5	8%
NEA	1	2%
NEZ	1	2%
NZ	3	5%
SA	1	2%
SZ	1	2%
TRM	14	22%
TRW	2	3%

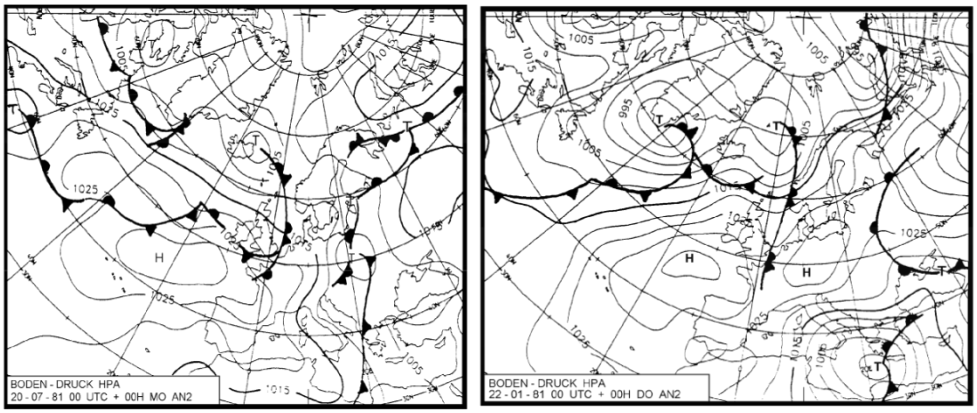

Figure 3.12: Synoptic situation corresponding to 'Central European trough' (TRM) type and 'Zonal Ridge across Central Europe' (BM) type, according to the GWL catalogue.

3.3. Summary and conclusions

The mechanisms underlying the occurrence of extreme hot and cold events for the 20-year period 1994-2013 in the Iberian Peninsula have been analysed using a Lagrangian approach. The synoptic conditions during the events have been characterised by means of Principal Component Analysis of the MSLP and geopotential fields at 850 and 700 hPa. The hot/cold episodes were selected based on the $99.9^{th}/0.1^{th}$ percentile of the 2-m height temperature from the ERA-Interim reanalysis data.

The study shows that there is a positive trend in the occurrence and persistence of both hot and cold events, with the slope of the trending lines being more pronounced for the period comprising the last ten years.

The analysis of the influence of the main climatic patterns affecting southern Europe showed that the annual number of cold extremes correlated negatively ($p < 0.01$) with NAO and AO annual indices, indicating that in years of positive (negative) NAO and/or AO, the production of cold extremes is lower (higher). On the other hand, a significant positive correlation ($p < 0.01$) was found between annual WeMO and the annual average temperature of hot events. Then, in years with a positive WeMO phase, the values of the extreme hot temperatures are higher, and vice versa.

No important meridional advection is involved in the production of hot extremes. Most of the back-trajectories remained within the IP and its close surroundings during the two or three days prior to the hot events. The evolution of the physical variables indicated that the occurrence of hot extremes was due to diabatic warming caused by air masses of long

residence time over the IP and to recirculation processes on summer days of weak baric gradient. The entrance of Saharan warm air masses from northern Africa seems to have less relevance and a more occasional character, as in the case of the August 2003 extreme temperatures.

Cold event back-trajectories were faster than those of hot events, and they were mainly associated with the advection of air-masses from northeast and northern Europe. The evolution of the median temperature versus median potential temperature showed that in the first days the air-masses experienced diabatic radiative cooling during their passage through the high latitude regions. This was followed by adiabatic warming due to subsidence, which was persistent until the start of the episodes.

While synoptic situations control the occurrence of cold events, hot events seem to be driven by mesoscale characteristics. This could explain why the persistence of cold events reaches the maximum frequency in two days, while for hot events this occurs in one day. However, there are a similar number of cold and hot episodes with a persistence of between one and three days, about 80%.

The Principal Component Analysis of the pressure and geopotential fields revealed two synoptic configurations causing cold air-masses to enter the Iberian Peninsula: the first one was associated with the presence of an anticyclonic system over central and northern Europe at low levels, as well as a trough in height. This configuration induces Polar winds over southern Europe and the western Mediterranean, and it coincides with the TRM pattern of the GWL European weather classification catalogue, which is the most frequently repeated during cold events. The second configuration corresponds to the formation of a blocking dipole with centres over the North Atlantic (south of Iceland, Scandinavia or north-western Russia) and central Europe. It impels north-easterly winds from the Siberian region to Western Europe and is related to the BM pattern of the GWL catalogue. This configuration, with a blocking system in the North Atlantic, has been widely associated with the occurrence of European winter cold extremes, characterised by subsident westward trajectories involving the retardation and/or reversal of the North Atlantic westerlies impinging upon Europe.

To better understand the mechanisms leading to extreme temperatures in the IP, the next chapter will focus on analysing two specific extreme cases: an episode that simultaneously affected most of the grid points, and another one that affected only a single

point, in order to determine the differences in the physical mechanisms involved in these situations. To this end, a more accurate characterization will be carried out through an analysis of these specific situations by means of the WRF mesoscale model.

Chapter 4

Chapter 4:

Analysis and simulation of two hot extreme events in the Iberian

4.1. Introduction

Hot extreme events can have implications on human comfort, environment, agriculture and hydrology (Schindler, 1997). For example, the heat wave that hit Europe during the summer of 2003 led to the destruction of large forest areas, the interruption of electricity, and affected water availability, ecosystems and agricultural production. That heat wave also claimed thousands of lives (UNEP, 2004). Between 1880 and 2005, the length of summer heat waves doubled and the frequency of hot days almost tripled over Western Europe. Moreover, daily mean temperatures have been rising over the Alps, Spain, and almost all of Europe in general (Dankers and Federer, 2008). At southern Europe and IP the mean temperature change was even higher than at central and Western Europe (Della–Marta *et al*., 2007).

The dynamics, occurrence, and effects of extreme hot events in general have been the focus of recent research (Jolly *et al*., 2005; Bieli *et al*., 2014; Santos *et al*., 2014), while more thorough investigations using the WRF model targeted both hot and cold events, heat waves, and temperature anomalies (Gladich *et al*., 2008; Pan *et al*., 2012; Mazon *et al*., 2014). Over Europe, an omega blocking system – usually described as a tri–synoptic system of a central high-pressure ridge and double side-troughs distributed in the west-east direction and lasting from a single day up to weeks – is usually associated with such heat waves (Bono *et al*., 2003; Escudero *et al.*, 2005; Francis *et al*., 2011; Salvador *et al*., 2014; Ceballos *et al*., 2016).

This chapter focuses on the study of two different hot–extreme events in IP occurring during the period 1994–2013. The events are selected based on the 12–hourly maximum temperatures at 2 m height obtained from the ERA–Interim reanalysis database. The

characterization of the meteorological conditions has been done by means of: 1) a Lagrangian approach to determine the air–mass pathways; 2) the study of the evolution of the physical variables along the back–trajectories; 3) the identification of the synoptic situations, and 4) WRF (Skamarock *et al.*, 2008) mesoscale numerical simulations.

4.2. Results and discussions

4.2.1. Evolution of the number of hot–extreme events

The annual number of hot extreme events divided by the number of grid points per region has been computed. The map with the four climatic regions is shown in Fig. 2.1 (chapter 2). Two different periods can be identified in the evolution of the number of hot events (Fig. 4.1): from 1996 to 2002 only 19% of events occurred, while the second half of the period (2003-2013) recorded 81%, occurring 30% of the hot extremes on 2003. This year,

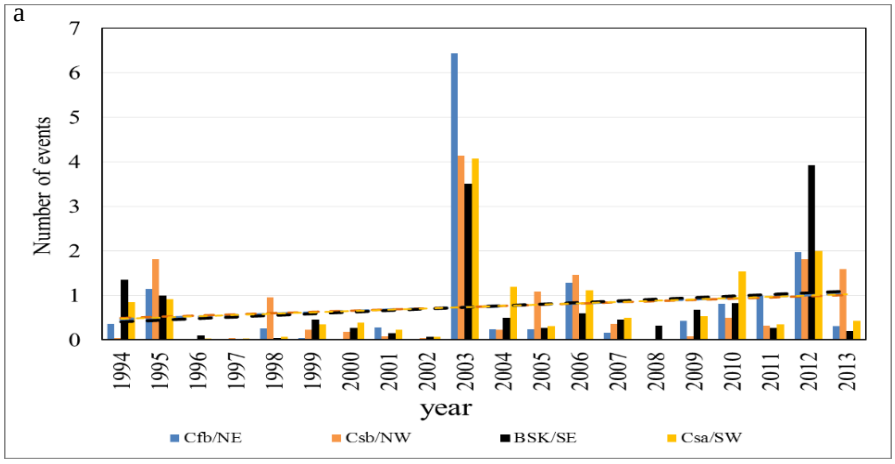

Figure 4.1: Annual number of hot extreme events divided by the number of grid points per region. Dashed lines show the trend, which is very similar for the 4 regions.

a heat wave hit Europe during the summer producing extensive damages at crops and forests and claiming thousands of lives (García-Herrera *et al.*, 2010; D'Ippoliti *et al.*, 2010).

The general trend of the number of hot events for the four climatic regions is positive: a positive trend of 0.3 day/decade for NE (Cfb), 0.2 day/decade for NW (Csb), 0.3.6 day/decade for SE (BSK) and 0.29 day/decade for SW (Csa) have been obtained. Regarding the temperature values during the hot events, the trend is positive for the whole IP (Fig. 4.2). This positive trend was also observed by Del Río *et al.* (2011) for the period 1961-2006. The specific trend for each of the four climatic regions is: 0.54 K/decade for NE (Cfb), 0.53 K/decade for NW (Csb), 0.8 K/decade for SE (BSK) and 0.07 K/decade

for SW (Csa). All the correlations were significant at the 0.01 level. According to these results, the increase of temperature is larger in the SE part of IP compared with the other regions.

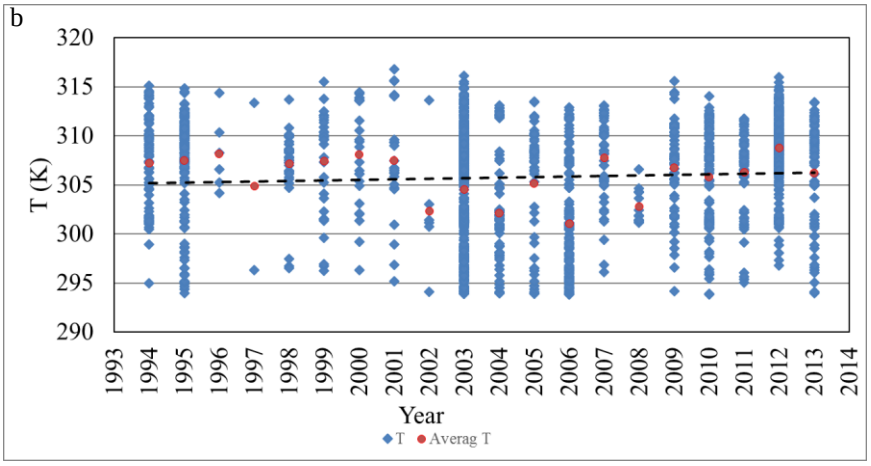

Figure 4.2: Temperature of the hot extreme events. Dashed line shows the trend and red dot represent the average temperature for each year.

4.2.2. The hot event on 10 August 2012

Figure 4.3 shows the grid points where the hot extreme event occurred on 10 August 2012 at 15 UTC (red stars), according to the criteria explained in Section 2.1. That day 53 grid points, covering 90% of IP, presented a hot extreme event. This is the episode that affected simultaneously to the highest number of grid points in the 20–analysed years.

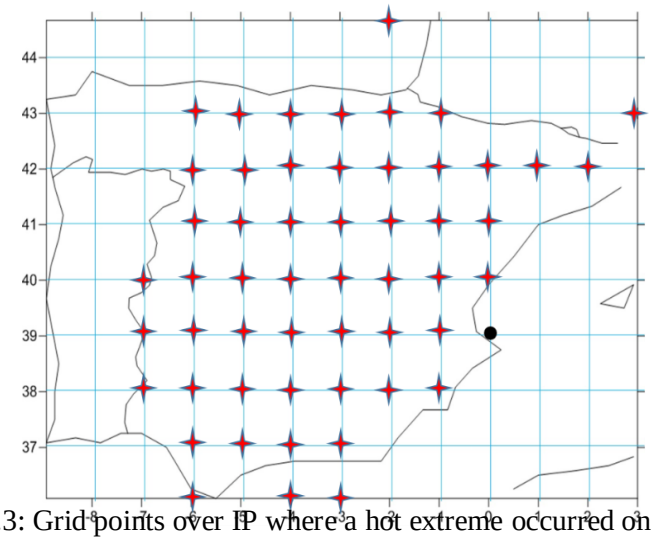

Figure 4.3: Grid points over IP where a hot extreme occurred on 10 August 2012 at 15 UTC (star) and the single grid point of the episode on 15 August 2012 at 15 UTC (black dot).

Figure 4.4a shows the simulated 2–m temperature, and wind field at 10 m in domain 1 (D1) on 10 August 2012 at 15 UTC. As can be observed, high temperatures occur in most of IP, except at the NW due, probably, to the clouds that covered that area. This can be clearly observed in the near–infrared image of the NOAA–19 satellite at 12:44 UTC (Fig. 4.4b). Cloudiness produce a decrease in the sensible heat flux (SH) in the NW region, with values around 120 Wm^{-2}, while in the centre and the southern region, SH reaches 320 Wm^{-2}, as can be observed in Fig. 4.4c.

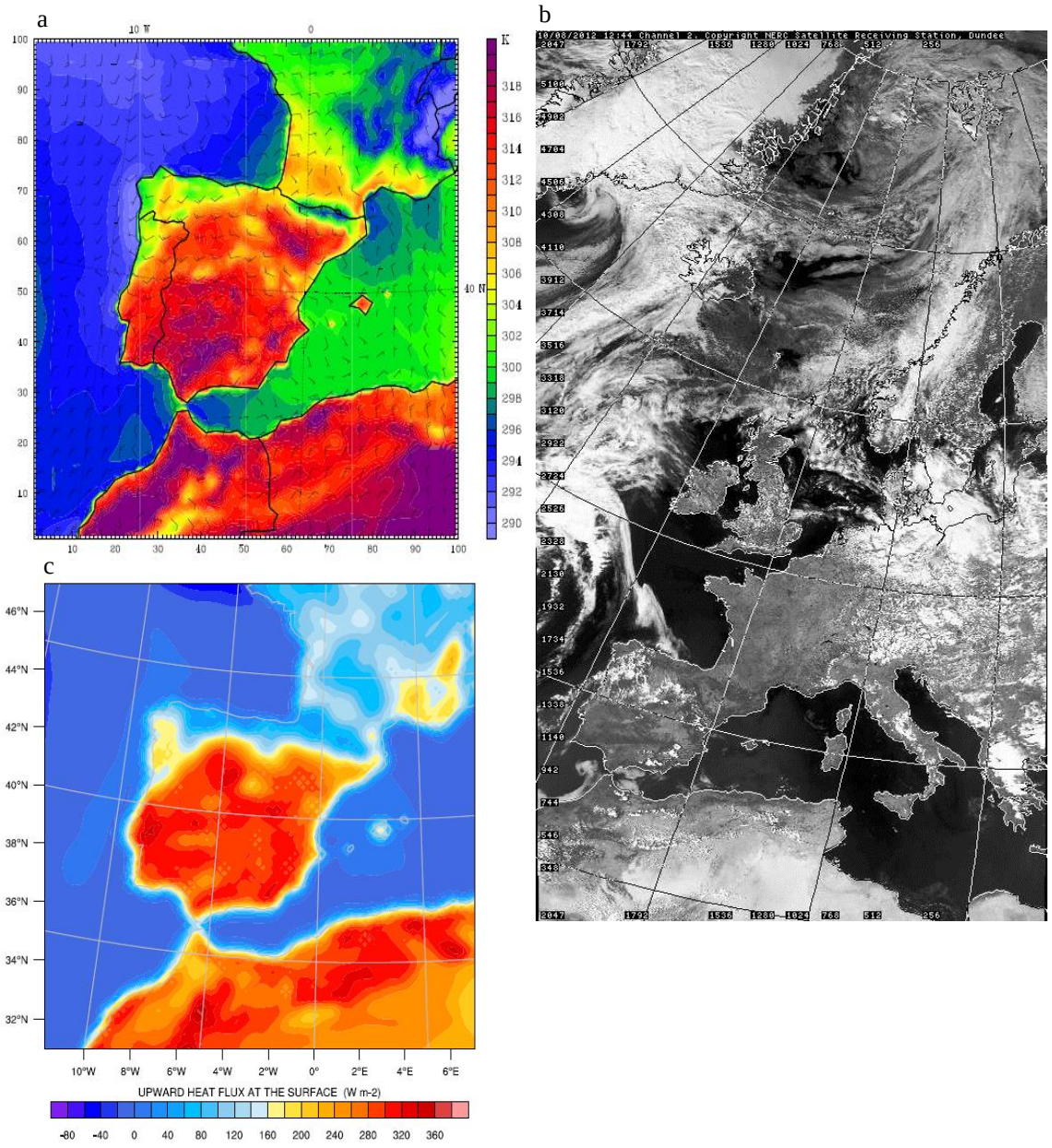

Figure 4.4: (a) Simulated 2–m temperature (K) (colour contour) and wind field at 10 m (barbs) in D1 on 10 August 2012 at 15 UTC. (b) Near–infrared image taken by the Advanced Very High–Resolution Radiometer on board NOAA–19 satellite at 12:44 UTC on 10 August 2012. (c) Simulated sensible heat flux (Wm^{-2}) in D1 on 10 August 2012 at 15 UTC.

On 10 August 2012 surface low–pressure areas covered the NW side of IP and East Europe and a strong anticyclone was over the western part of the British Islands suggesting an omega blocking system (see Fig. 4.5). Furthermore, the Azores anticyclone extended from eastern North Atlantic to western Iberian Peninsula inducing southerly air advection. The omega–shaped wave that also can be observed at 850 and 700 hPa (not shown) favoured the transport of warm dry air from north Africa to Europe, while the North Atlantic anticyclone prevented air mass movements, making the air mass stationary above the Iberian Peninsula and thus raising the temperatures. This omega–shaped blocking system moved on 11, 12 and 13 August 2012 (not shown) to the East, producing a decrease along these days in the number of grid points at the western part of IP affected by the extreme temperatures.

Back–trajectories are computed with origin at the grid points at the time of the episodes

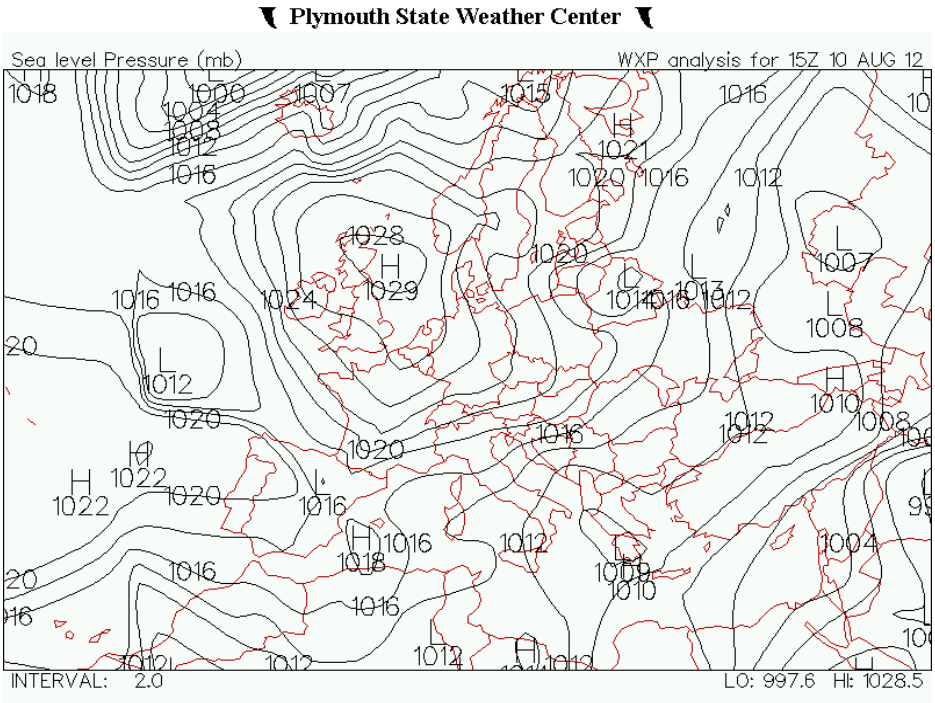

Figure 4.5: Sea–level pressure map on 10 August 2012 at 15 UTC over Europe. (Source: Plymouth weather centre)

onset. Table 4.1 shows sectors of provenance for the 4– and 10–days back–trajectories (i.e. the position of the time steps 96 and 240, respectively) reaching the 53 grid points with a hot extreme event on 10 August 2012 at 15 UTC. As it can be observed (highlighted in bold), advection from the Atlantic Ocean dominated at all the regions 10 days before

the extreme event, with an increasing influence of eastern circulation during the last 4 days before the extreme events.

Table 4.1: Number of 10– and 4–day back–trajectories with origin in each sector, with respect IP, that reach a point, where an extreme event occurred on 10 August 2012 at 15 UTC, in the different climatic regions. Highlighted in bold the dominant sectors.

	10–day					**4–day**				
Climatic region/ Origin	Csa (SW)	Cfb (NE)	BSK (SE)	Csb (NW)	**Total**	Csa (SW)	Cfb (NE)	BSK (SE)	Csb (NW)	**Total**
N	**4**	5	3	0	12	**4**	**6**	0	2	12
NE	**4**	0	0	0	4	0	0	0	0	0
NW	2	**8**	**15**	**7**	**32**	0	3	0	0	3
E	0	1	1	0	2	2	3	**16**	2	**23**
S	0	0	2	0	2	**4**	1	3	0	8
W	0	1	0	0	1	0	2	2	**3**	7
Total	10	15	21	7	53	10	15	21	7	53

4.2.2.1. Trajectory densities

Trajectory density, i.e., the number of back–trajectory time steps per grid box ($1^o \times 1^o$) was computed for the back–trajectories of 10 days, 4 days and 12 hours length, at 100 m a.s.l. corresponding to the 53 grid points presenting hot extreme on 10 August 2012 at 15 UTC (see Figs. 4.6a, b and c, respectively). The maximum density for the 10-day back-trajectories (Fig. 4.6a) can be observed north of the Pyrenees, over the Mediterranean and south of IP; smallest values occur at the North Atlantic Ocean. For the 4–days back–trajectories, large densities occur over the Mediterranean and at southern IP (Fig. 4.6b). Finally, for 12-hour, almost all the trajectories are confined over IP (Fig. 4.6c). In general, most of the trajectories remain within the IP and its close surroundings during the two days before the hot events due to the influence of the omega blocking system. Consequently, local recirculation of warm air masses is the main responsible for the achievement of high temperatures, rather than the punctual entrance of North African air masses. This fact was already suggested by Millán *et a*l. (1997), Jorba *et al*. (2004) and Izquierdo *et a*l. (2015), who showed the occurrence of predominant slow–moving recirculation flows from W and SW in summer.

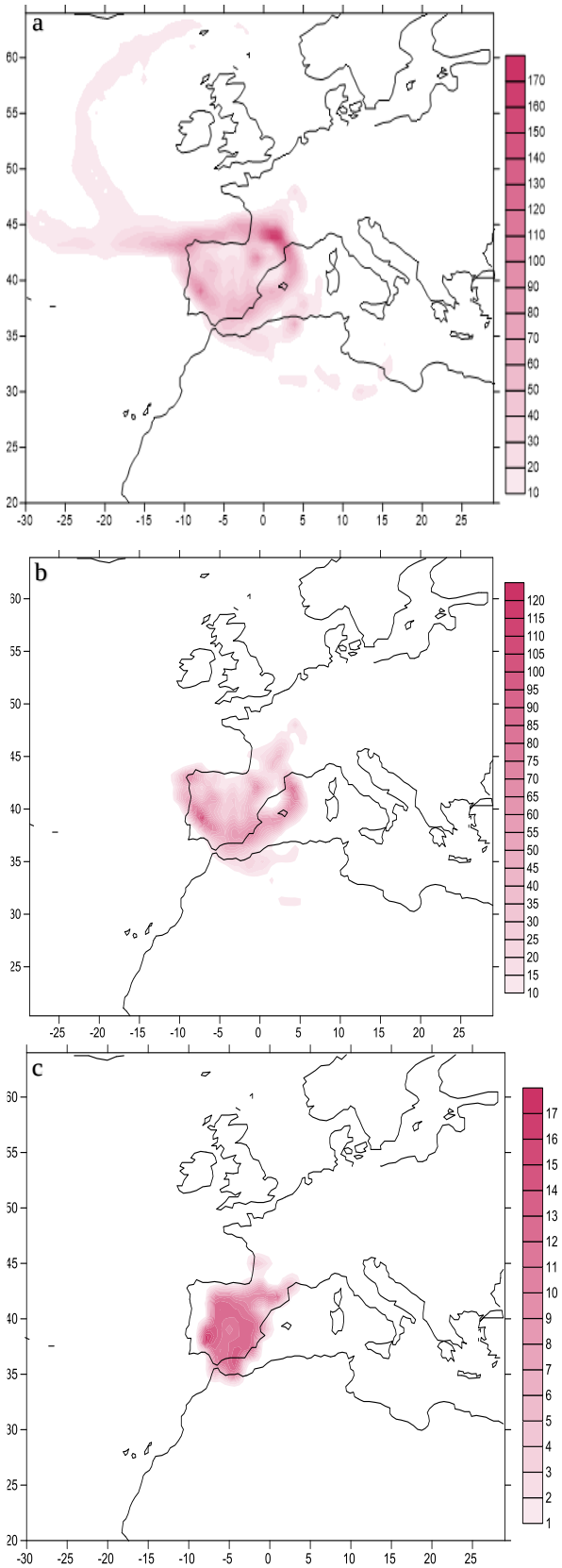

Figure 4.6: (a) 10–day, (b) 4–day and (c) 12–hour back–trajectory densities (number of time steps per grid box) arriving at 100 m for the hot–extreme events occurred on 10 August 2012 at 15 UTC.

The 4–days trajectory density for the four climatic regions classified according to the Köppen –Geiger climate types (see Fig. 4.7) shows that only for the NW region (Fig. 4.7b) recirculation over the IP occurs. For the other three regions, air masses move over regions outside the IP: western Mediterranean Sea, South of France or North Africa.

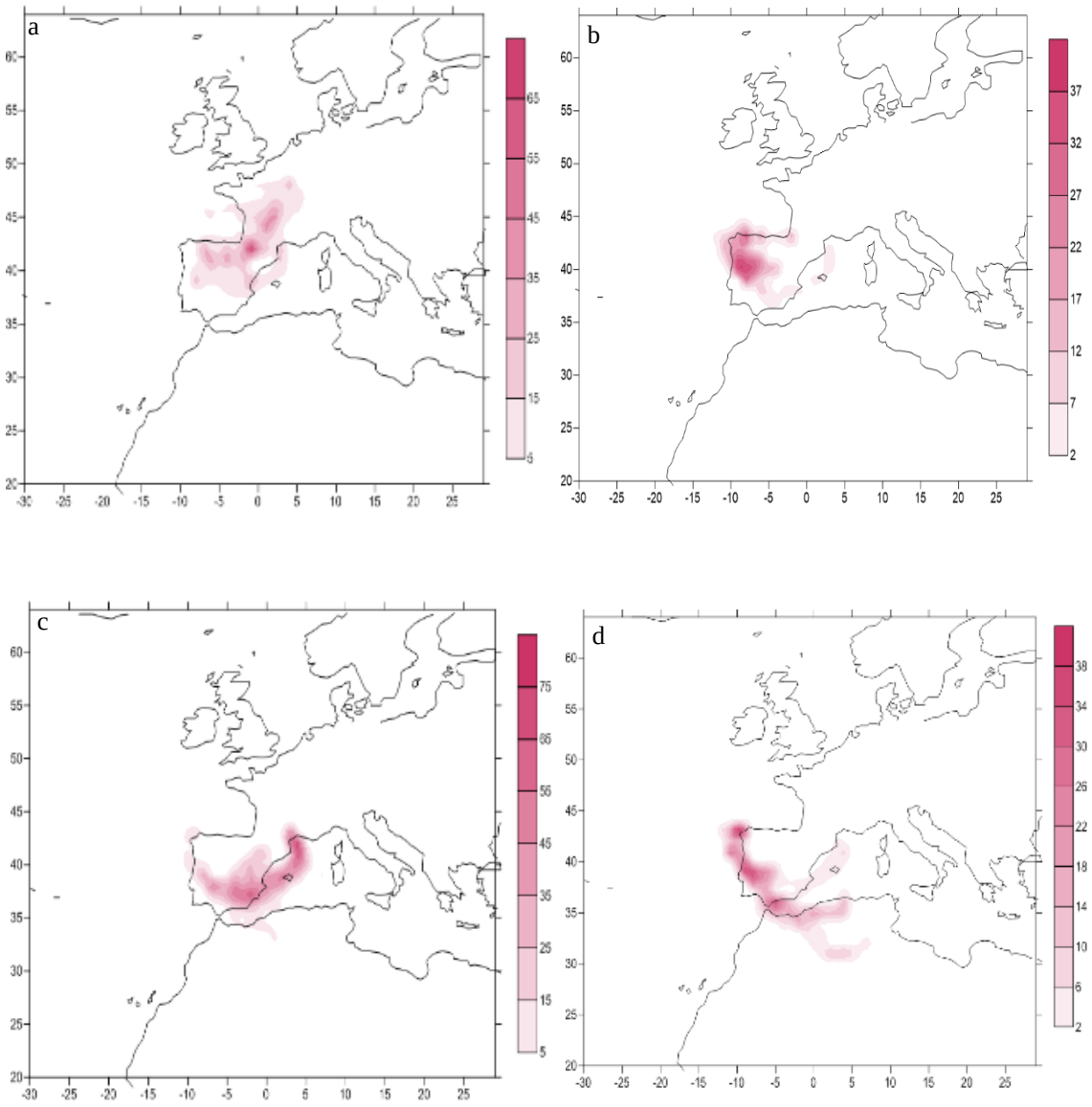

Figure 4.7: 4–day back–trajectory densities (number of time steps per grid box) arriving at 100 m for the hot–extreme events occurred on 10 August 2012 at 15 UTC at (a) NE (Cfa), (b) NW (Csb), (c) SE (BSK), and (d) SW (Csa).

4.2.2.2. Evolution of physical variables along the trajectories

Figure 4.8 shows the meridional and zonal displacements of the 5th, 25th, 50th (median), 75th, and 95th percentiles of the 10-day back–trajectories reaching the 53 grid points where the extreme event occurred on 10 August 2012. The median of the 10–days back–trajectories comes from the Atlantic, southwest of Ireland, and experiences a latitudinal decrease of about 10º and a longitudinal increase of 10º. From the 10th to the 4th day, the median air mass moves to the east with almost constant latitude. Then, the air mass moves to the south and to the west entering the IP.

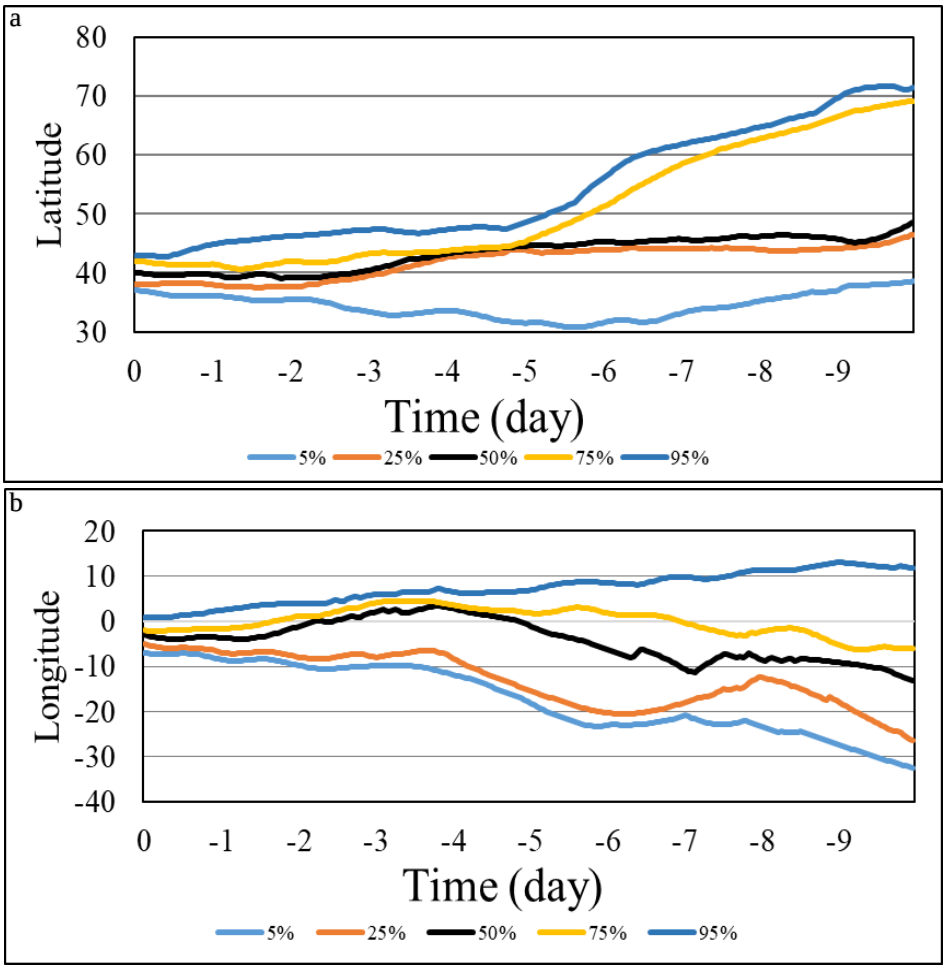

Figure 4.8: a) Meridional and b) zonal movement of the 5th, 25th, 50th, 75th and 95th percentile of the back–trajectories causing a hot extreme event in the 53 grid points of IP on 10 August 2012 at 15 UTC.

The evolution of T, θ and mixing–layer height along the 10–days median back–trajectory is shown in Fig. 4.9. From the 10th day to 3rd day before the event, the air masses move mainly over the North Atlantic Ocean, at an almost constant height (not shown) and temperature and potential temperature do not change, probably because there is a low sensible heat flux over the ocean. In contrast, during the last three days, when the air mass

enters the IP, there is a clear diurnal cycle and a significant increase of the temperature (red line), and the mixing–layer height (blue line). The evolution of the potential temperature follows a similar pattern (Fig. 4.9, orange line), indicating that diabatic heating is the main warming mechanism produced by the absorption of sensible heat flux.

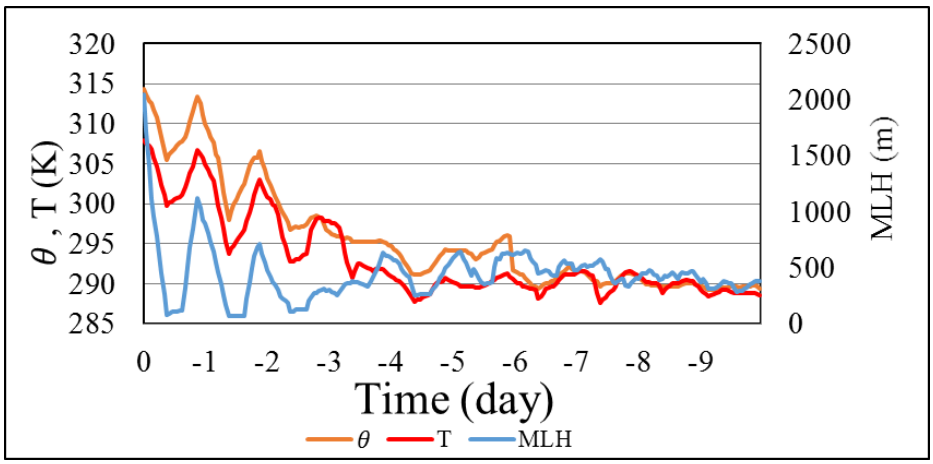

Figure 4.9: Evolution of the temperature, potential temperature and mixing–layer height along the median 10–days back–trajectory for the hot extreme events occurred on 10 August 2012 at 15 UTC.

The meridional and zonal displacements of the median back–trajectory reaching the four climatic regions are shown in Fig. 4.10. For the NE and NW regions, the median originates at the North Atlantic, near the Polar Circle, following a latitudinal decrease of about 30º, observed mainly during the first five days; longitude fluctuates indicating some zonal circulation. The last three days before 10 August 2012, the median of the trajectories arriving these regions show almost constant latitude and a little variation of around 5º of longitude, indicating recirculation over IP. For the median of the back–trajectories reaching SE and SW regions, the origin is at the North Atlantic but further south, west of the Irish coast. During the 10 days, latitude decreases around 10º and longitude increases around 25º and 5º for SE and SW regions, respectively, moving from west to east. Four days before the event, the median of these two air masses begin to move towards the west. The last twelve hours before the extreme event, the median of the four regions show approximately the same evolution.

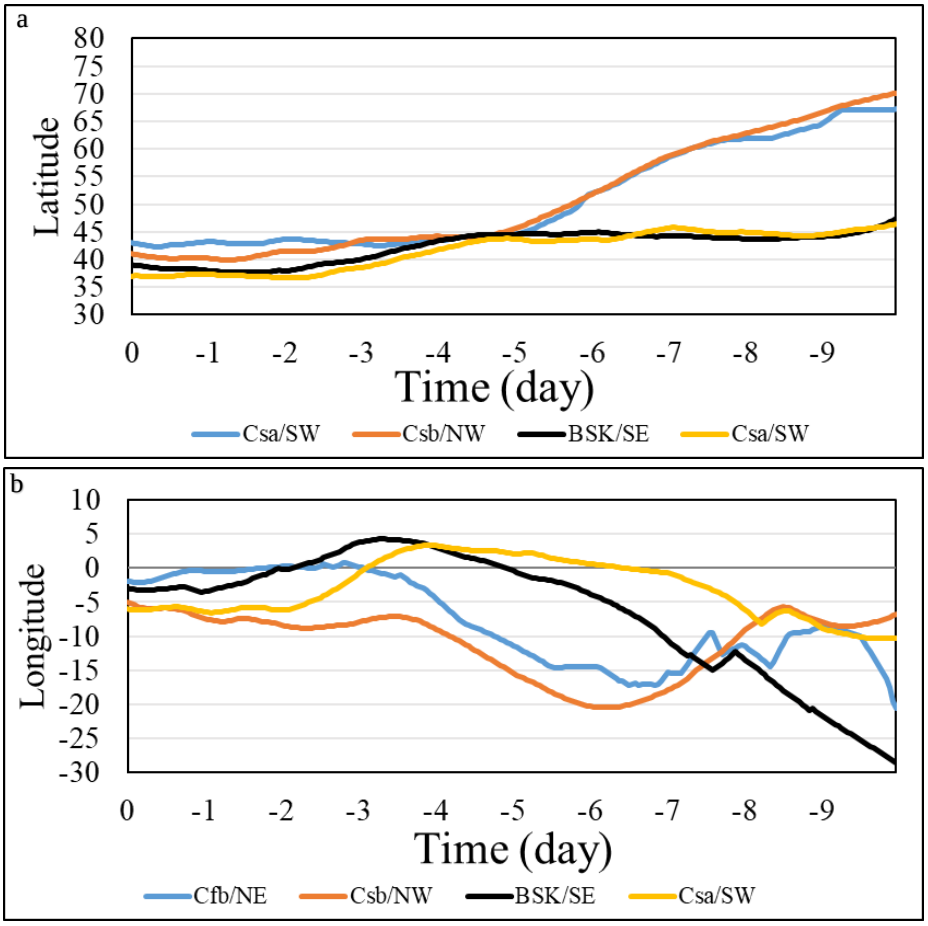

Figure 4.10: a**)** Meridional and b) zonal movement of the air masses during the 10–day back–trajectory causing the hot extreme events in the four climatic regions of IP on 10 August 2012 at 15 UTC.

Figure 4.11 shows the evolution of the temperature along the median 10–days back–trajectories for the four climatic regions. There are differences in the temperature evolution along the trajectories between the median trajectories reaching the southern regions (black and yellow lines) and northern (blue and orange) ones. A diurnal cycle can be observed in all the median trajectories, especially during the last three days. As can be observed, origin of the median back–trajectory clearly influences the temperature of the air mass 10 days before the event. Temperature increase is larger along the back–trajectory reaching the northern regions (25 versus 20 K) since the final temperature for both northern and southern is similar but was lower that of the northern ones. The air temperature evolution along the trajectories arriving at SE and SW regions shows that during the first 5 days temperature does not present large variations (specially for SE) because sensible heat flux is small (the air mass is over sea) and height is almost constant (not shown). In contrast, very strong and rapid diabatic warming (the air mass is over IP) during the three days before the extreme cause to raise the temperature more than 12 K.

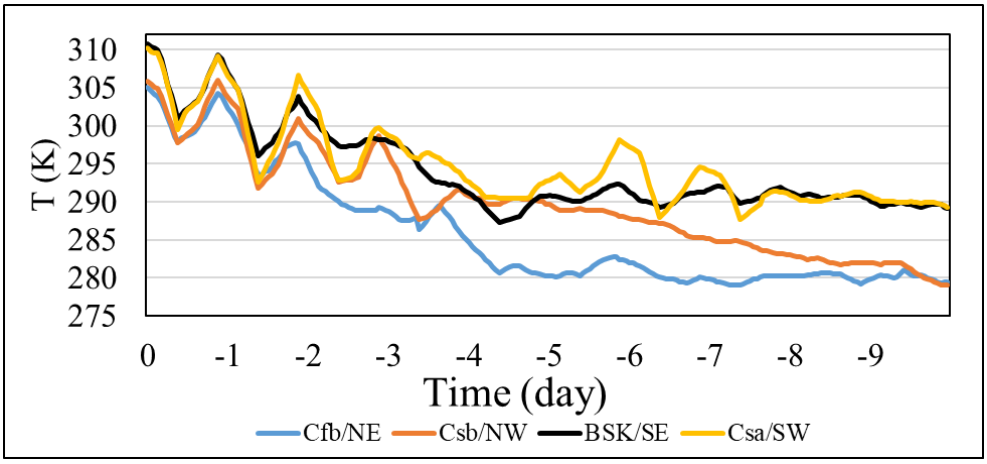

Figure 4.11: Evolution of the air temperature of the air masses along the median 10–day back–trajectory causing the hot extreme events in the four climatic regions of IP on 10 August 2012 at 15 UTC.

The evolution of the mixing–layer height along the median back–trajectory for the four regions is shown in Fig. 4.12. Mixing–layer height fluctuates around 500 m during the first 6 days. However, in the three days before the hot events, there is a progressive increase of the maximum mixing–layer height and a marked diurnal cycle, indicating large convection when the air mass enters the IP. The final values of the mixing–layer height for the air masses arriving to SE and SW is double than for the trajectories reaching the NE and NW regions. This is probably associated to the mainly land use of the SE and SW regions, arid land, that produces a larger SH. On the other hand, these two regions, located in the south of IP, are more affected by the warm flow coming from North Africa.

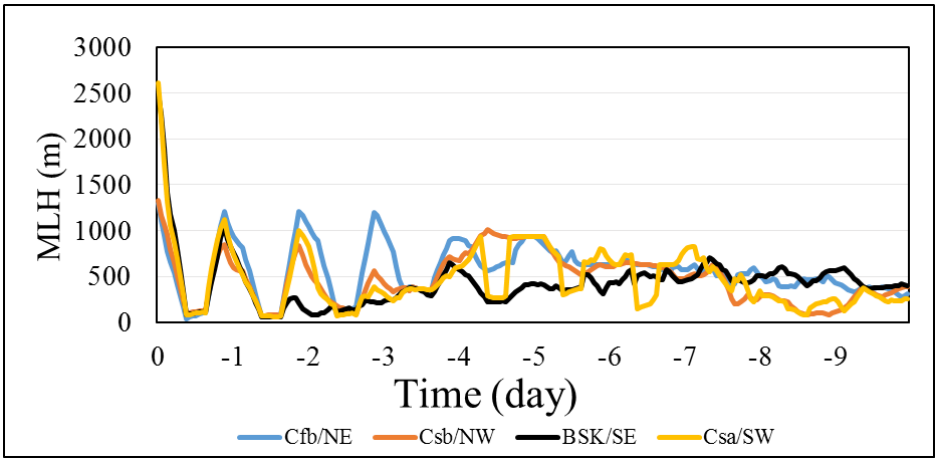

Figure 4.12: Evolution of the mixing-layer height in four regions along the median 10–day back–trajectory causing the hot extreme events in the four climatic regions of IP on 10 August 2012 at 15 UTC.

4.2.3. The event on 15 August 2012

4.2.3.1.Back–trajectories

The location of the grid point (39°N–00º, point A, hereinafter), where the extreme hot event occurred on 15 August 2012 at 15 UTC, is showed in Fig. 4.3 and in some of the figures below. Figure 4.12 shows the 10-day meridional and zonal movements of the air mass reaching point A calculated by HYSPLIT (black lines). The longitudinal displacement is remarkable (from 40°W to 00°), while the latitudinal variation is much smaller. The air mass travels from mid-latitudes in the North Atlantic Ocean entering to the IP at the western coast 48 hours before the event and moves over IP shifting to the South and then to the North at the eastern part of IP. Fig. 4.13 also shows the median meridional and zonal displacement of the trajectories corresponding to all the grid points in the IP (yellow lines). As can be observed, the evolution is similar and westerly winds prevailed for all the IP.

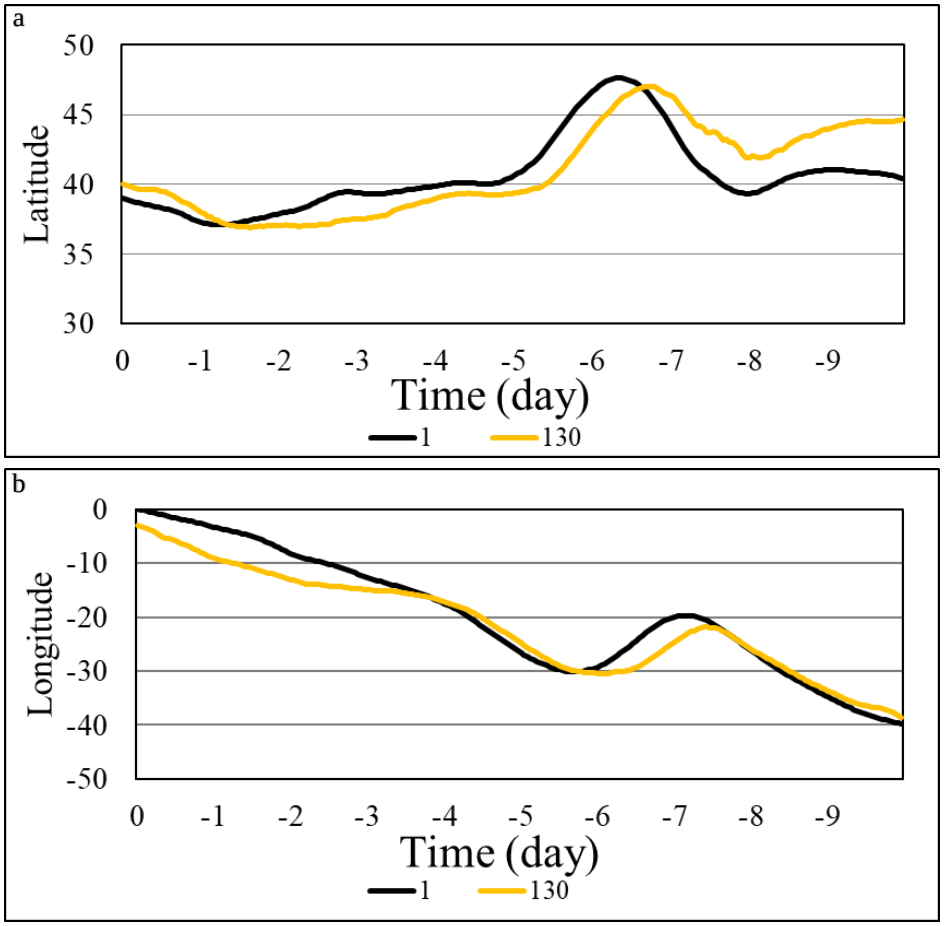

Figure 4.13: Evolution of (a) latitude and (b) longitude along the trajectory reaching 39ºN–0º at 15 UTC on 15 August 2012 (black lines) and of the median of the back–trajectories reaching all the 130 points defined in the Iberian Peninsula at the same time (yellow lines).

Temperature and potential temperature evolution calculated by HYSPLIT along the trajectory reaching point A increase by about 20 K (Fig. 4.14, black lines). 48 hours before the extreme event, when the air mass moves over land, a diurnal cycle can be noticed and T and θ rapidly increase. The maximum values of T and θ along the back trajectory occur 24 hours before the extreme event with 307 and 303 K respectively, then decline 3 and 2 K, respectively, at point A on 15 August 2012 at 15 UTC. From the 10th to the 3rd day before the event, T and θ along the median back–trajectory reaching all the points of IP show approximately the same evolution (Fig. 4.14, yellow lines). During the last three days before the extreme event, the diurnal cycles of T and θ are smoothed due to the average over all the trajectories reaching the IP.

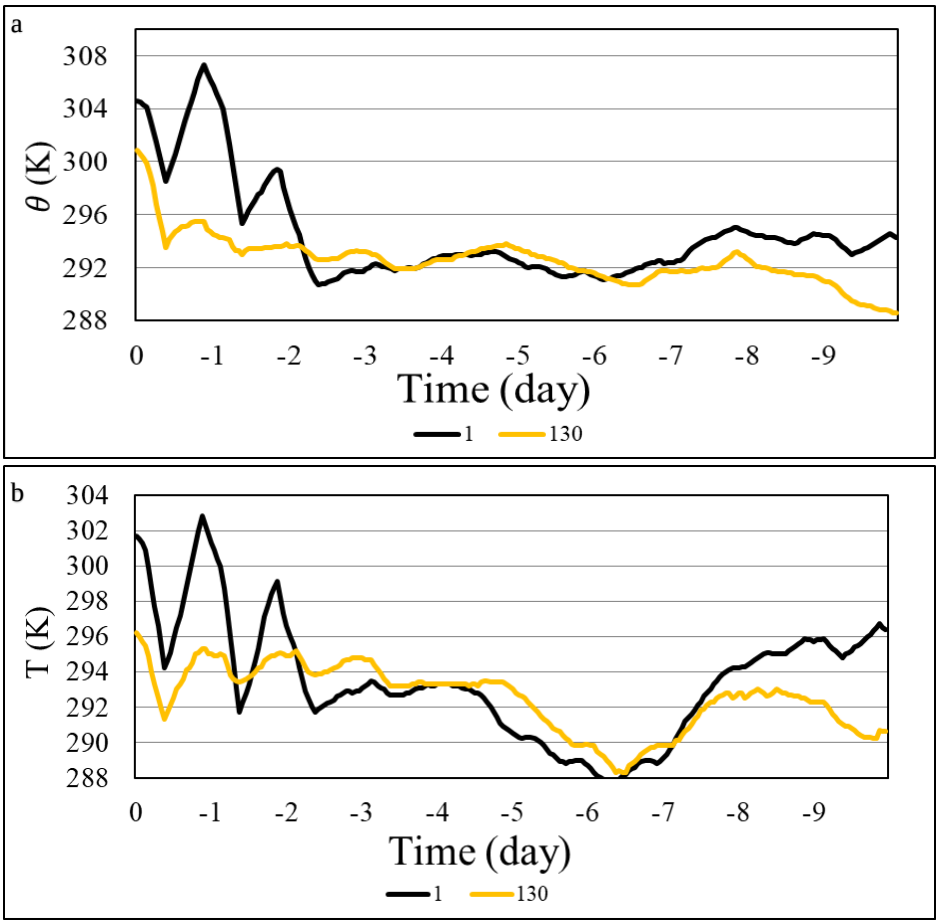

Figure 4.14: Evolution of (a) θ and (b) T along the back–trajectories represented in Fig. 4.13.

We have also calculated, by using HYSPLIT, the 10–day back–trajectories for the four grid points: 39ºN–1ºW, 39ºN–1ºE, 38ºN–00º and 40ºN–00º, surrounding point A, to analyse if there are differences in the pathway for the nearest points to A. The back–trajectories reaching the four grid points surrounding point A do not show significant

differences when comparing with the back–trajectory reaching A (Fig. 4.15), they have mainly a zonal movement during the last three days, and the physical variables along the different pathways are very similar (not shown). Consequently, the extreme occurred at point A can be due to local conditions or it's only a statistical effect of the analysis and a consequence of the synoptic conditions.

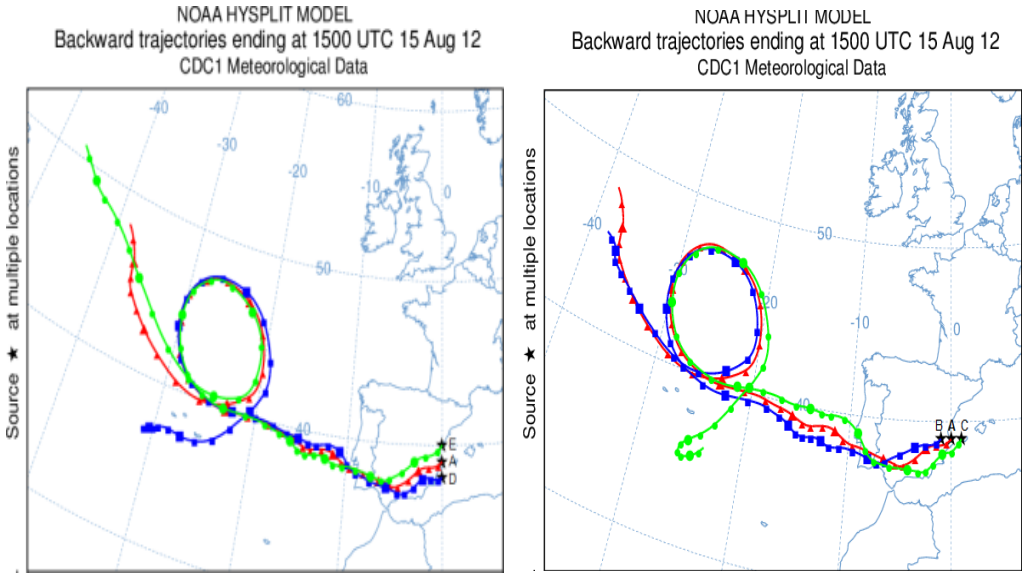

Figure 4.15: 10-day back-trajectory reaching five different points on 15 August 2012 at 15 UTC: 39ºN-0º (A), 39ºN-1ºW (B), 39ºN-1ºE (C), 38ºN-0 (D) and (40ºN-0 (E) using HYSPLIT model.

However, the assumption about the influence of local features on the extreme event cannot be demonstrated by using the HYSPLIT model because the model does not have enough horizontal resolution.

To analyse this local conditions, surface fluxes and wind field have to be analysed but HYSPLIT model does not provide information about these variables. Therefore, we will use the WRF mesoscale model, having higher resolution, to analyse the atmospheric conditions three days before the extreme event.

4.2.3.2. WRF mesoscale numerical simulation

The horizontal cross–sections of 2–m temperature, and wind field at 10 m from 13 to 15 August 15 UTC simulated in D1 are shown in Fig. 4.16. It can be observed how daytime 2-m temperature increases since 13 August, especially at the central and eastern parts of IP. On 15 August T decreases at the west and centre of IP due to the existence of altostratus clouds.

The simulated sensible heat flux (SH) in D1 domain is shown in Fig. 4.17. On 13 and 14 August at 15 UTC, the highest value of SH is obtained at the western part of IP: around 320 Wm^{-2} and 280 Wm^{-2}, respectively (Figs. 4.17a and b), while, on 15 August at 15 UTC, the highest value of SH occurred at the eastern part of IP and is around 220 Wm^{-2} (Fig. 4.17c).

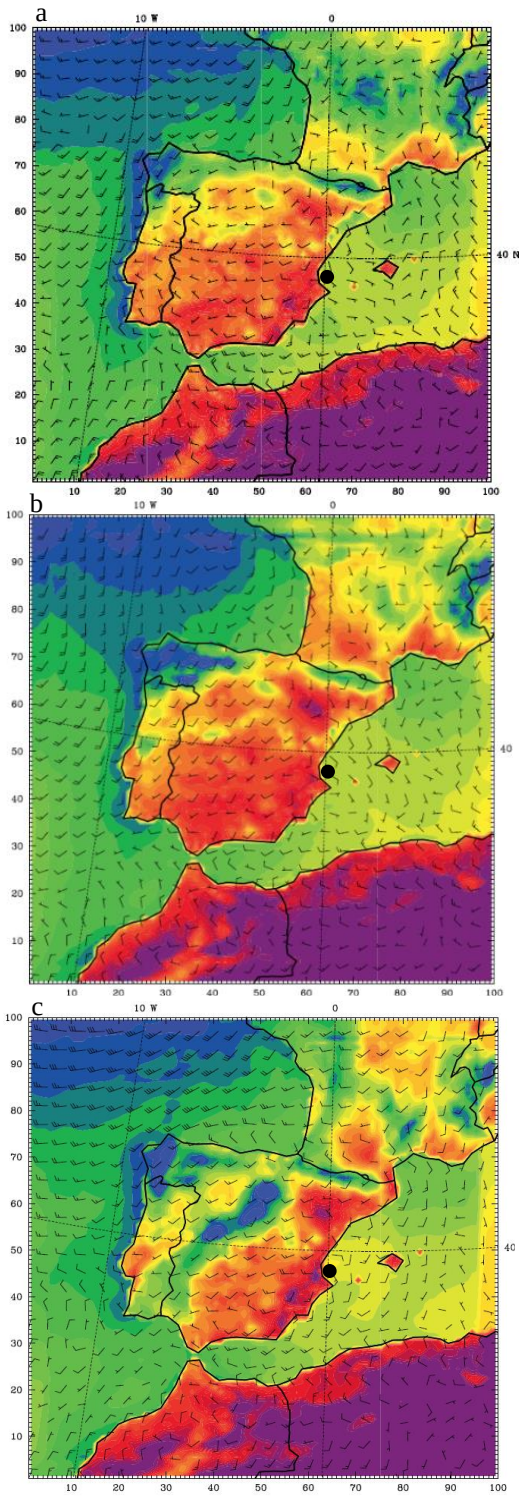

Figure 4.16: Simulated 2–m temperature (colour contour), and wind field at 10 m (barbs) for domain 1 at 15 UTC on a) 13, b) 14 and c) 15 August 2012. The location of point A is marked by a black dot.

In this figure it can be also observed the lower values of SH (about 40 Wm^{-2}) in the central region, due to the clouds covering IP from southwest to northeast. This can be clearly observed in the near–infrared image of the NOAA-19 satellite at 13:31 UTC (Fig. 4.17d). On 15 August, despite the fact that the SH is lower and the advection of sea breeze from the Mediterranean Sea might help to decrease the temperature along the coastline, temperature at the central eastern coast is high enough to produce an extreme at point A.

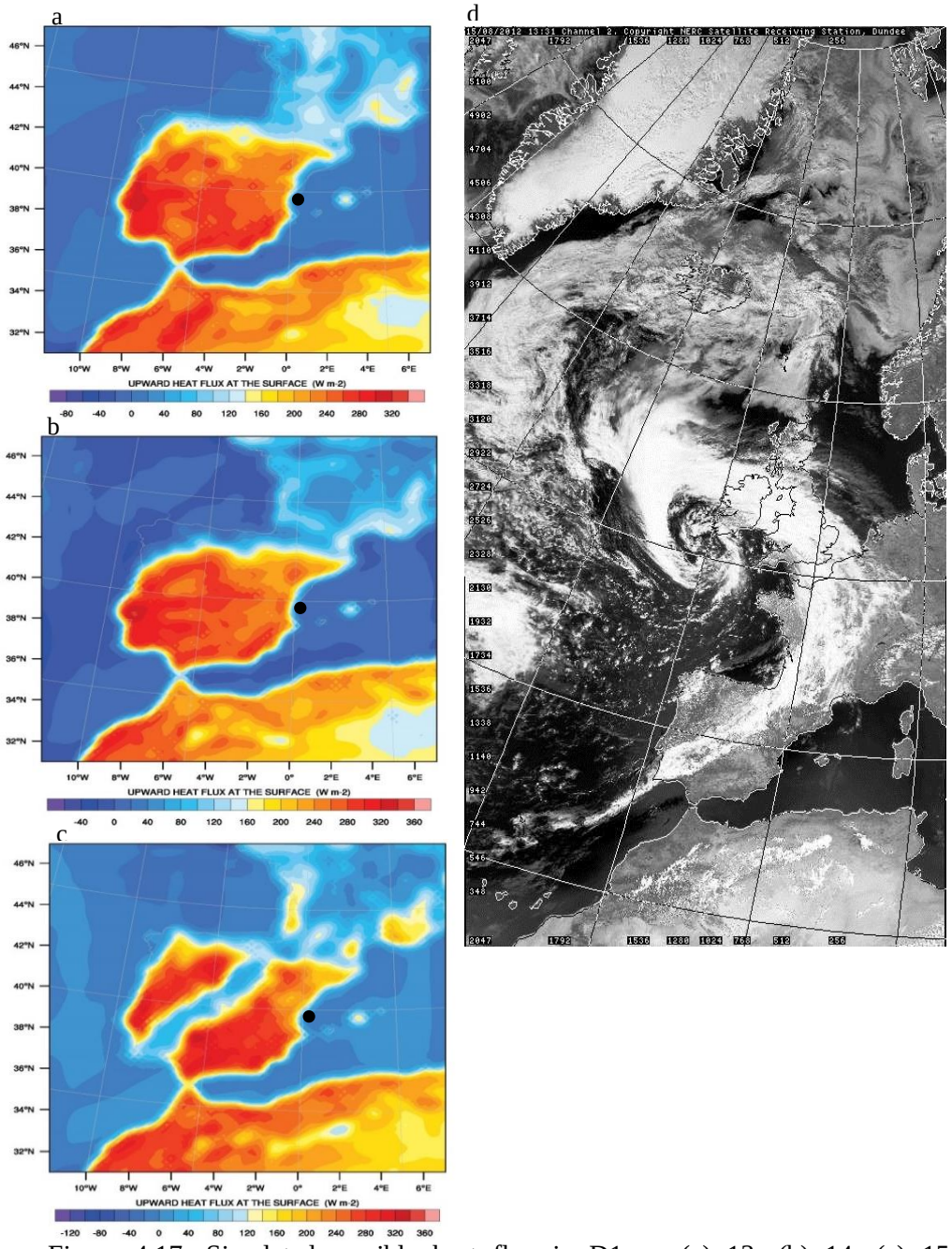

Figure 4.17: Simulated sensible heat flux in D1 on (a) 13, (b) 14, (c) 15 August 2012 at 15 UTC and (d) Near–infrared image taken by the Advanced Very High–Resolution Radiometer on board NOAA–19 satellite at 13:31 UTC on 15August 2012. The location of point A is marked by a black dot.

To analyse this in detail, Figs. 4.18a–d show the horizontal cross–section of the 2–m temperature, and wind field at 10 m simulated at domain 3 (D3) at 10, 13, 14 and 15 UTC on 15 August 2012. As mentioned before, HYSPLIT describes the air mass reaching A coming from the west, where high temperatures occur. However, WRF simulates a sea breeze at the central eastern coast that intensity increases from 10 to 15 UTC and being more powerful than the prevailing westerly wind. Consequently, the sea breeze prevents the air mass coming from the west to directly reach point A. According to WRF, during the hours leading up to the event, the responsible air mass reaching A comes from the S-SE, entering during a short period over land at the south of the domain (2-m temperature around 310 K), where the temperature of the air mass increases.

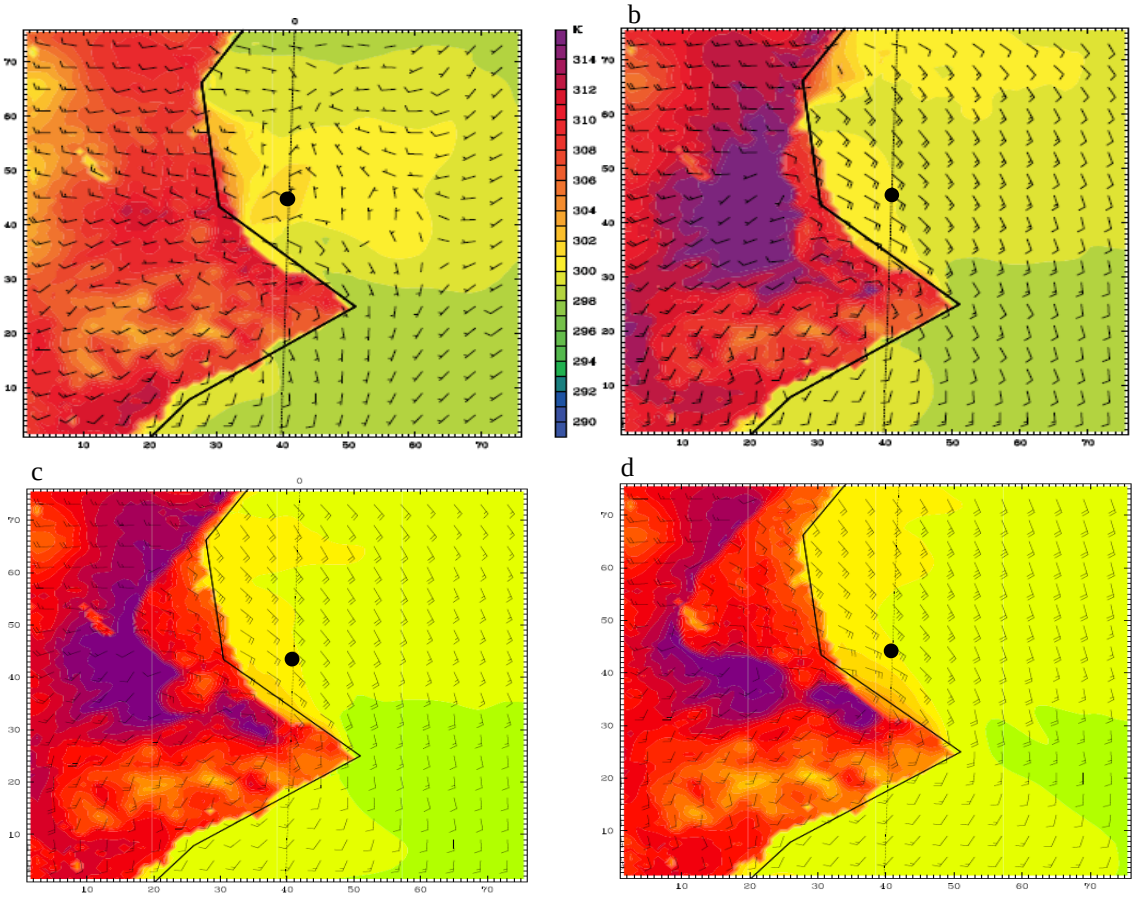

Figure 4.18: Simulated 2–m temperature (colour contour) and wind field at 10 m (barbs) in D3 on 15 August 2012 at (a) 10, (b) 13, (c) 14, (d) 15 UTC. The location of point A is marked with a black dot.

The back-trajectories for the four points surrounding point A have also been calculated with WRF (Fig. 4.19), indicating that the air mass reaching this area come from the west but during the last 12 hours come from the south and south west, when the temperature experience a large increase.

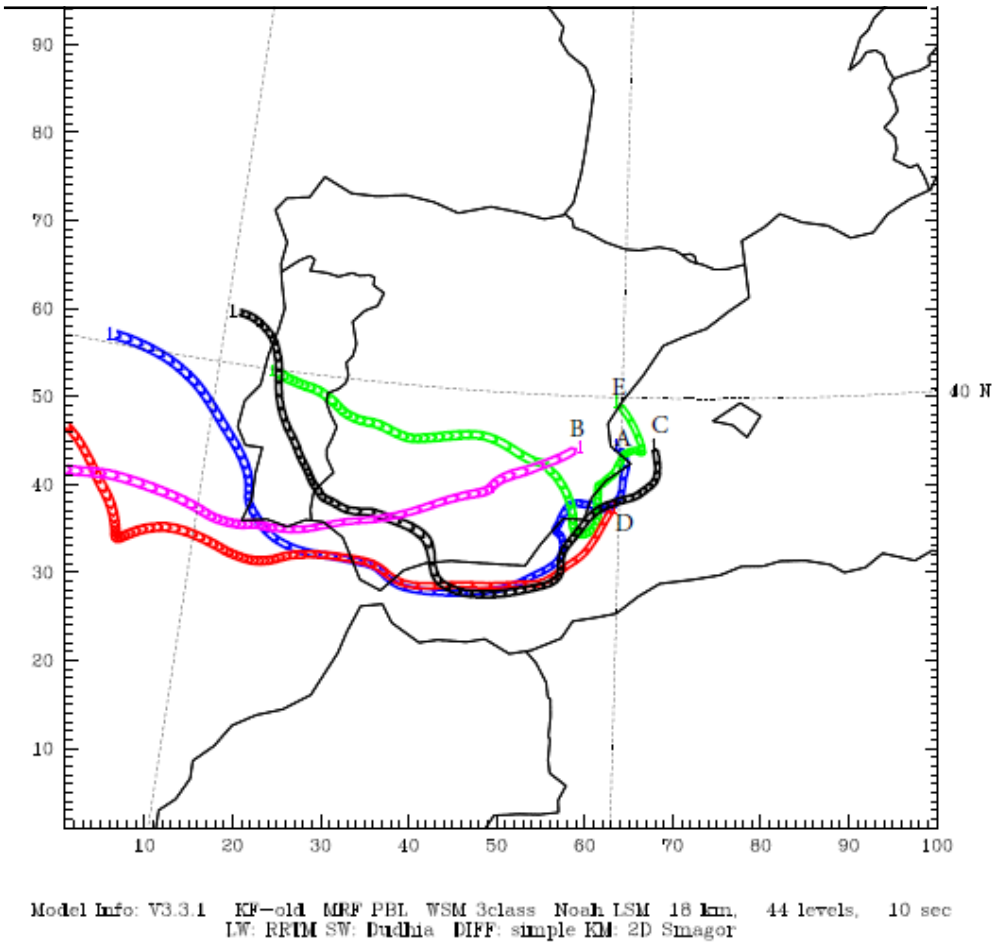

Figure 4.19: 4-day back trajectory reaching five different points on 15 August 2012 at 15 UTC: 39ºN-0º (A), 39ºN-1ºW (B), 39ºN-1ºE (C), 38ºN-0 (D), and (40ºN-0 (E) using WRF model and RIP4 software (http://www2.mmm.ucar.edu/wrf/users/docs/ripug.htm).

The simulated SH in D3 at 13, 14 and 15 UTC on 15 August 2012 is shown in Figs. 4.20a, c and e. Despite there is a decrease of SH from 13 to 15 UTC, strong diabatic warming near the surface occurred in this period, where the maximum value (440 Wm^{-2} at 13 UTC) occurs in the southern part of D3, the area crossed by the air mass reaching point A.

The latent heat (LE) flux in D3 at the same hours is shown in Figs. 4.20b, d and f. During the two hours previous to the extreme, LE increases rapidly, mainly due to: i) the southern warmer air mass which arrived to the area, that causes a decrease of the humidity, and ii) an increase in south-easterly wind speed in the area, near point A.

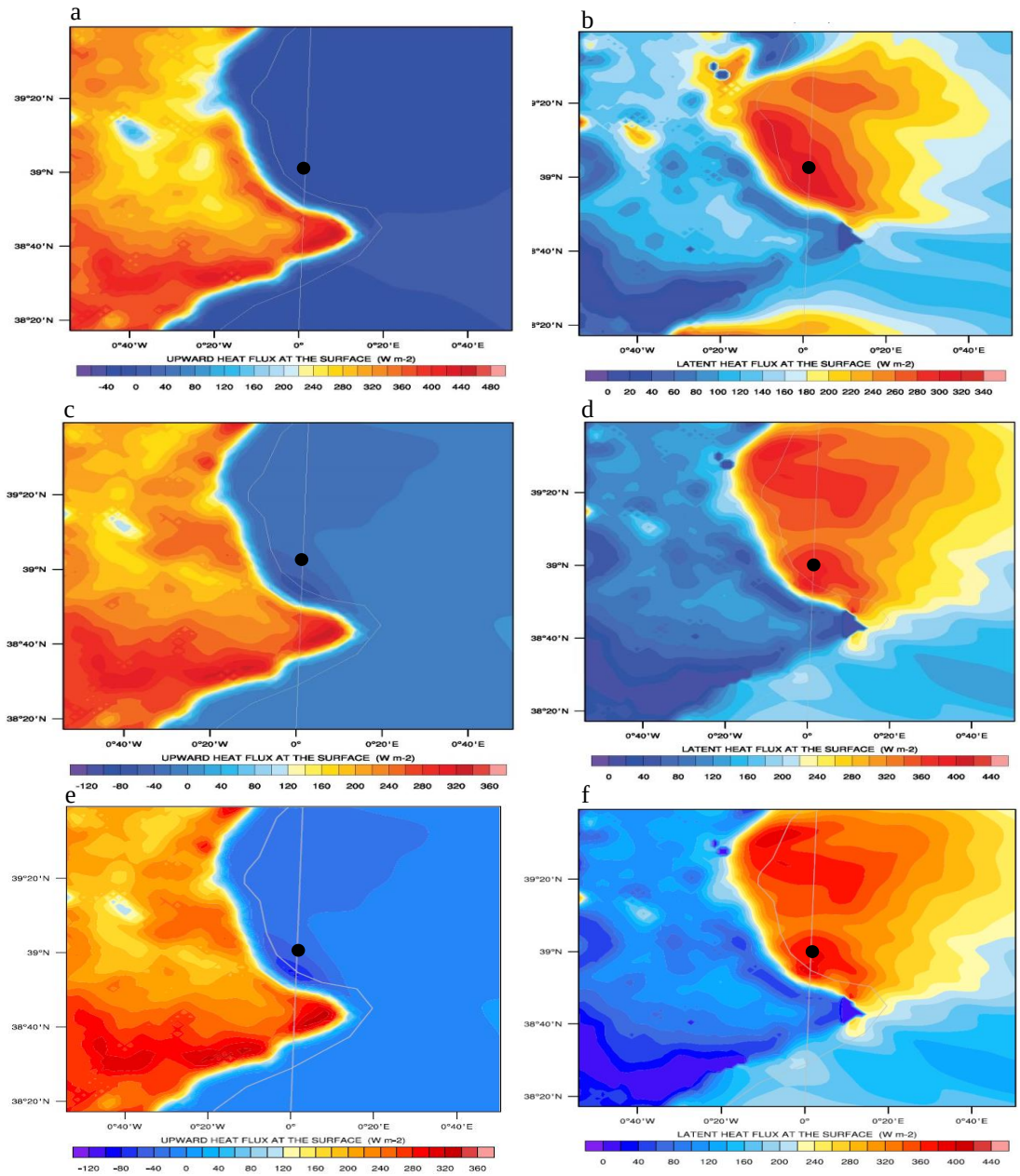

Figure 4.20: Simulated sensible (left) and latent (right) heat flux in D3 at 15 UTC on (top) 13, (middle) 14 and (bottom) 15 August 2012. Point A is marked by a black dot.

4.3. Summary and Conclusions

This study examines the mechanisms underlying the occurrence of hot extreme events in the Iberian Peninsula by using a Lagrangian approach and WRF numerical simulations. Temperatures in the 1%–tails of the empirical distributions at each grid point are considered for the period 1994 to 2013.

The general tendency in the number of hot events for the four climatic regions is positive but not significant, with very small differences between them. The general tendency of temperature during the hot events presents a larger increase at the south east part of IP.

The evolution of the annual mean number of hot–extreme events shows that most of the events occurred in the second part of the analysed period. There is a positive trend in the number of the hot extremes for the whole IP and for the four studied climatic regions.

Two days presenting temperature extremes have been selected: (1) 10 August 2012, when the highest number of grid points present extreme temperatures and (2) 15 August 2012, when only one grid point presents a hot extreme.

The extreme events occurring at 53 grid points on 10 August 2012 at 15 UTC have been studied by tracking the evolution of the physical variables along the 10–days back–trajectories ending at the grid points. In addition, the evolution of the variables has also been analysed independently for the median back-trajectories reaching the four climatic regions.

The synoptic situation on that day shows at the surface an anticyclone centred north-west of the British Islands and two low–pressure systems located at both sides of the anticyclone, over eastern Europe and the north Atlantic, suggesting an omega blocking system. This system induces a warm flux from the south-east of the Iberian Peninsula, reinforced by the presence of the Azores anticyclone

The back–trajectory density results for the 53 grid points presenting an extreme shows no important meridional advection, being local recirculation of warm air masses the main mechanism responsible for the occurrence of high temperatures.

The temperature evolution along the median back–trajectory shows a significant increase and a clear diurnal cycle when the air mass enters IP during the last two days before the event. The potential temperature evolution along the median back–trajectory shows a similar evolution suggesting temperature increases due to diabatic processes due to the absorption of sensible heat flux.

Regarding the evolution of the temperature along the median trajectory followed by the air masses reaching the different climatic regions, those arriving to the SE and SW regions show an increase of temperature by about 5 K lower than the air masses reaching NE and

NW during the 10 days before the extreme event, but the final temperature at SE and SW region is higher than the NE and NW temperature by about 5 K. These differences are related with the origin of the back–trajectories for the NE and NW regions at the North Atlantic, near the Polar Circle, while for the SE and SW regions the origin is at the North Atlantic but further south.

Summarizing, there are three reasons that could explain the extreme event on 10 August 2012: 1) an anticyclonic circulation centred over North Atlantic and extended to the Mediterranean Sea producing southern air advection over IP; (2) a deep omega–blocking wave over Northern Europe causing a stagnant situation; 3) diabatic heating produced large sensible heat flux.

For the second analysed event, the hot extreme at point A on 15 August 2012, it happened after several days when extreme events occurred at large areas of the IP: 53 extremes on 10 August, 31 on 11, 11 on 12 and 3 on 13 August. No extreme events occurred on 14 August. The possible causes for the only extreme on 15 August are related to: (1) the heat accumulation in the IP during the previous days, (2) the air masses arrive to the central eastern coast mainly after crossing the IP from west to east, specially following a path over the southern region in which the sensible heat flux is high, enhancing thus temperature and potential temperature, and (3) on 15 August 2012, a large part of IP (specially the central area) was covered by clouds preventing the temperature to rise in other areas, consequently, despite these conditions may produce extremes at several points of the eastern central coast of the IP, there is only an extreme on that day at point 39ºN–0ºE due to the statistical method used to select the extreme events during the 20–analysed years (T2MAX was above its 99.9^{th} percentile for the 20 years period 1994–2013).

Chapter 5

Chapter 5

Dynamical and physical processes involving hot and cold extreme events in Iraq

5.1. Introduction

Iraq has an arid climate and extreme temperatures are frequent in winter and summer. Summer temperatures have experienced an increase in the recent years (Salman. *et al.*, 2017). The extreme heat waves occurring in Iraq are related with a strong ridge of high pressure which usually stays over the Middle East during July (Nasrallah *et al*., 2004). Summer climate is usualy influenced by the Indian low-pressure system (monsoon low) which start in the mid of May and led to temperature increases over the Arabian Desert, while winter temperatures are usually related to the Siberian high pressure system (Nasrallah *et al*., 2004; and Khidher, 2015).

Despite Iraq has been listed as one of the most vulnerable countries to climate change in the Arab region (UNDP, 2010), few works have studied the underlying phenomena that cause extreme temperatures at the region. Robaa and Al-Barzanji (2015) evaluated the trends of surface air temperatures, Muslih and Błażejczyk (2016) estimated the inter-annual changes and the long-term trends of monthly temperatures and Salman (2017) assessed the trends in annual and seasonal daily average minimum and maximum temperatures.

Regarding the relation between the extremes in Iraq and the large-scale circulation modes, Salar *et al*. (2014) analysed the relation between circulation patterns leading to extreme events and hemispheric oscillation patterns, such as the North Atlantic Oscillation (NAO). They concluded that NAO positive phases causes the expansion of the desert climatic

region (Bwh) and, simultaneously, diminishes the surface of other climate regions (BSH and Csa). In contrast, few studies analysed the relationship between hot /cold events and the East Atlantic Index (EA) in eastern Mediterranean Sea and Iraq but Dragan-Burić *et al*. (2018) find a link between EA index and changes of air temperature over the western Mediterranean Sea. However, the synoptic and mesoscale conditions and the dynamics of the air masses causing the extreme temperatures have not been addressed yet.

This chapter is focused on the study of the hot/cold extreme episodes in Iraq for a period of 20 years (1994-2013), based on the 12-hous maximum/minimum temperatures at 2-m height obtained from the ECMWF ERA-Interim reanalysis database. The characterization of the hot/cold extremes has been done by means of: 1) a Lagrangian approach to determine the air mass pathways; 2) the study of the evolution of the physical variables along the trajectories.

5.2. Results and discussion

5.2.1. Annual distribution and correlation with climatic indices

Figure 5.1a shows the average temperature of hot extremes at each grid point. The highest values for the hot events correspond to the SE region and the lowest ones to the NE, with a difference between them of about 20 K. Regarding the cold events, Fig. 5.1b shows the average temperature of cold extremes at each grid point. The lowest values for the cold events correspond to the NE region and the highest ones to the S, with a difference between them of about 25 K.

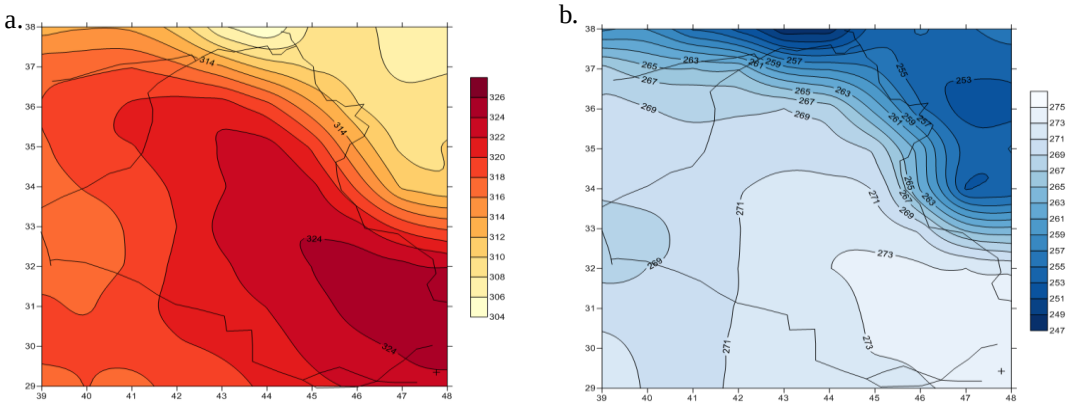

Figure 5.1: Geographical distribution of the average of extreme temperatures at each grid point for the 20-year period for a) hot, and b) cold extreme events.

The Spearman rank, Kendall's tau and the Pearson's correlation were applied for detecting correlations between the annual and winter climatic indices (NAO, AO and EA) and the number of extreme events, as well as the annual average extreme temperature for all the grid points. No significant correlations were found between the number of hot and cold extremes and NAO. On the other hand, a significant positive correlation ($p<0.01$) was found between the annual average hot temperature and the annual positive phase of the EA pattern (Kendall: 0.368; Spearman: 0.489; and Pearson: 0.678). Lim (2015) studied the dynamic mechanisms linking to the EA positive phase with hot extreme events over Siberia by studying the temporal correlation between the monthly-standardized extreme temperature for all grid points and the teleconnection pattern time series valid for the month of August. He concluded that the EA positive phase shows a strong zonal flow over the East Atlantic towards the east to central Europe and Turkey, reaching the Middle East and causing temperatures to rise above the regional means. These results are in agreement with our results, which suggest that median hot extreme events over Iraq are caused by warm air mass advection from Turkey towards the NW of Iraq (Shamal winds, Figs. 5.4 and 5.5c), similarly to a strong flow during the EA positive phase.

Regarding the cold extreme events, no correlations were found with NAO, AO and EA indices. This result differs from Al Khalid (2017) who found a relationship between the positive phase of NAO and temperature anomalies in winter over Iraq during the period 1979-2016, probably due to the different length of the analysed periods.

5.2.2. Annual distribution of hot/cold-extreme events according to the Koppen-Geiger climate classification

The number of grid points for each climatic region according to the Koppen-Geiger climate classification (Peel *et al*., 2007) is shown in Fig. 5.2. The Koppen classification presents three-main climates characterizing the Iraqi region. According to the used database for hot and cold events, the BWh, BSh and Csa regions present an average temperature of 320, 315and 309 K in the summer and 269, 263 and 256 K in the winter.

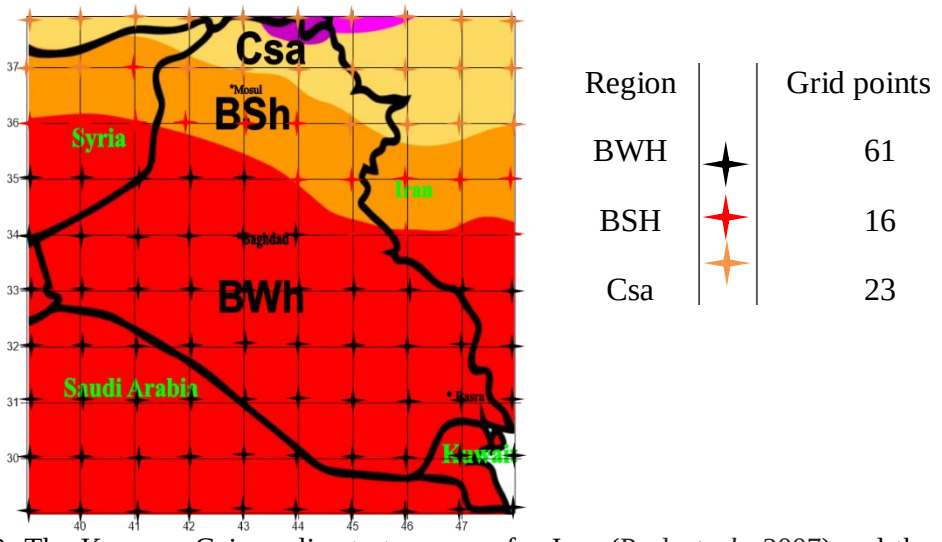

Figure 5.2: The Koppen- Geiger climate type map for Iraq (Peel *et al.*, 2007) and the number of grid points for each climatic region.

Figure 5.3a shows the annual distribution of the number of hot events divided by the number of grid points per region for the studied period (1994-2013). We can clearly identify the 1994-1997 period as the one with the lowest number of recorded events in all regions (2% of total events). Noticeable peaks of occurrence were recorded in the BWh region in the summers of 1998, 2000, 2001 and 2003 (65% of all BWh occurrences). The BSH and Csa regions did not register any increase in those years, with the exception of 2000. In general, the BWh region registered the highest number of extreme hot events over the full period with 61% of the total events, while the BSh and Csa regions recorded only 16% and 23% of events respectively. From 2008 to 2013, all regions recorded an increase in the number of hot extreme events, with a large peak recorded in 2011. The general trend of the number of hot events for all regions is positive: 5, 5 and 10.4 days/decade for BWh, BSh and Csa respectively. Regarding the evolution of the number of cold events divided by the number of grid points per region over the period 1994-2013 (Fig. 5.3b), 67% of the events occurred during the second decade. In all regions there are important peaks in the number of cold events in 1994, 1997 and 2008, representing 57% of the total number of events. All regions show an exceptional peak during the winters of 1997 and 2008 (55% of all the events that occurred in BWh, 51% in BSh, and 35% in Csa). From 2009 to 2013, all regions registered a decrease in the number of cold events – except in 2012, where only BWh registered a peak. The general trend of the number of cold events for all regions is positive: 12, 4 and 3 days/decade for BWh, BSh, and Csa, respectively.

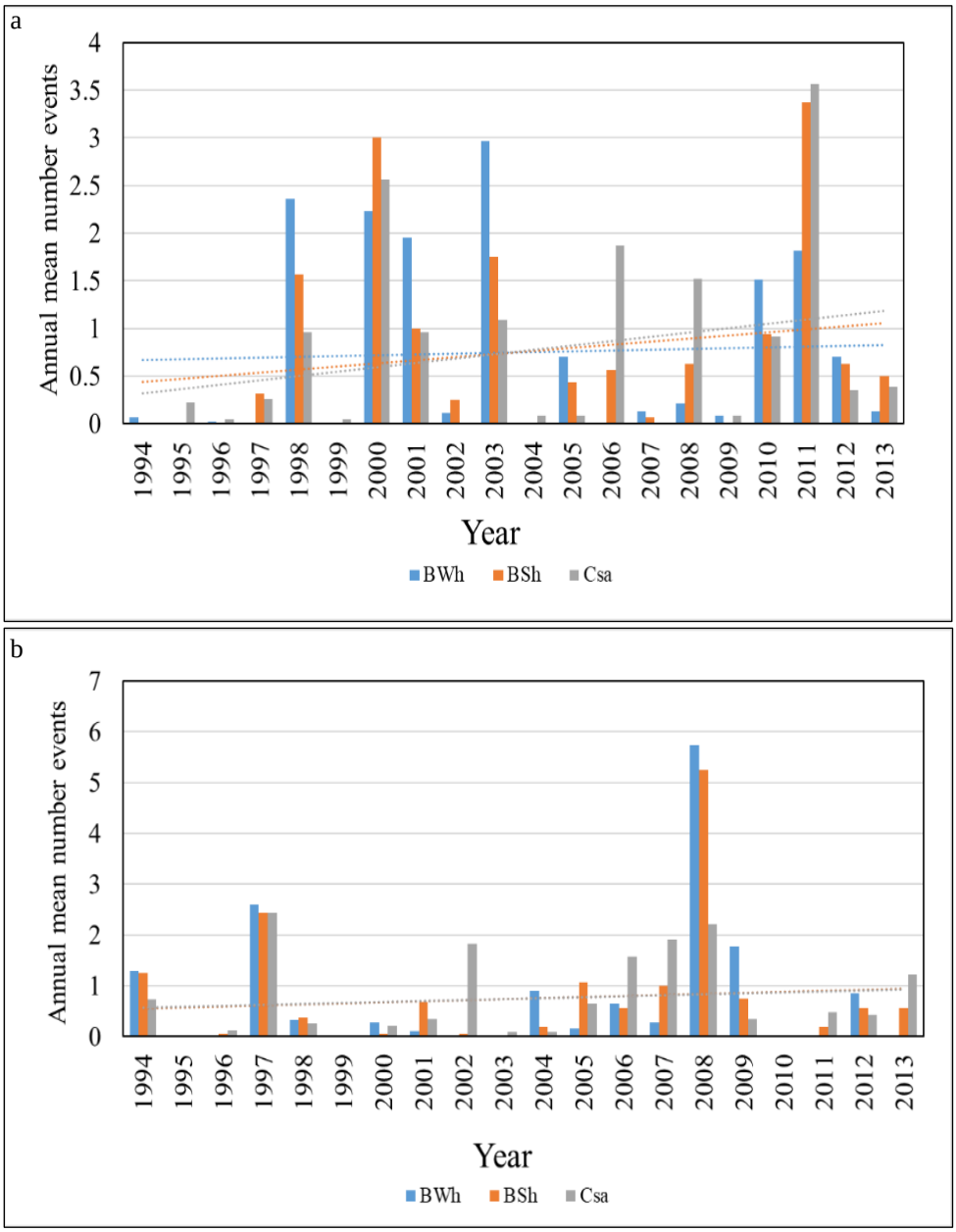

Figure 5.3: Annual number of extreme events divided by the number of grid points per region for each climatic region for a) hot b) cold extreme events.

5.2.3. Trajectory densities

Back-trajectories were computed using the coordinates of the grid points as final destination at the time the episodes occurred. For hot extremes, the distance travelled by the median of the 4-day back-trajectories is 940 km at 100 m a.s.l. and 850 km at 1500 m

a.s.l. For the cold events, the distance travelled by the median is 1325 km and 2740 km at 100 and 1500 m a.s.l., respectively. For 10-day back-trajectories, these distances are 2500 km at 100 m and 2220 km at 1500 m a.s.l. for hot events, and 3900 km and 6570 km for cold events. Thus, distances travelled by the cold trajectories are longer than those travelled by the hot ones. Cold-event trajectories are faster probably because are related to advection processes while for hot events recirculation over Iraq plays a more relevant role. The trajectory densities, i.e. the number of back-trajectory time steps per grid box ($1^o \times 1^o$) were calculated by superimposing a grid mesh of $1^o \times 1^o$ to the integration domain of the back-trajectories. Densities were computed for 4- and 10-day back-trajectories, at 100 and 1500 m a.s.l. The results corresponding to hot events for 4-day at 100 and 1500 m a.s.l. are shown in Figs. 5.4a, b. Density is higher on the north side of Iraq, extending from the Caspian Sea on the NE and from the East Mediterranean coast to the western borders. In general, for the two vertical levels, most of the trajectories remain within Iraq and its close surroundings during the days prior to the hot events, indicating that the local recirculation of warm air masses is the main cause for the extreme temperatures. The density map obtained over 10-days back-trajectories (Figs. 5.4c, d) is very similar to the 4-days, but the trajectory densities extend more towards Eastern Europe, Siberia, the east side of Iraq and to the Indian Subcontinent at the west side.

The meridional and zonal displacements of the hot events back-trajectories can be better appreciated in Fig. 5.5, where the evolution of latitude and longitude are presented for the 5^{th}, 25^{th}, 50^{th}, 75^{th} and 95^{th} percentiles of the back-trajectories at 100 m producing a hot extreme event. For the median trajectory (black line), a latitudinal decrease of about 15 degrees is observed, whereas there is a longitudinal increase of 3 degrees (Figs. 5.5a and b). The median air mass pathway starts over southern Russia and moves to Georgia, Azerbaijan, and Iran, before entering Iraq from the north 84 hours before the extreme events. Finally, it moves to the southern region of Iraq (Fig. 5.5c).

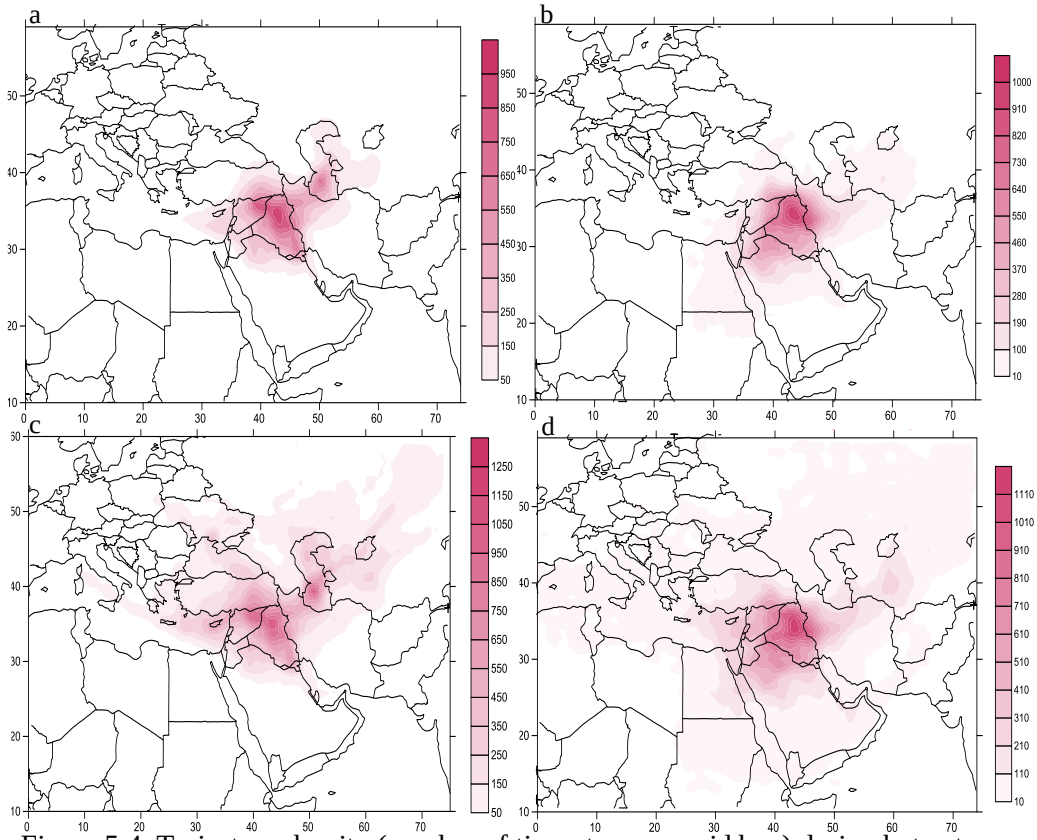

Figure 5.4: Trajectory density (number of time steps per grid box) during hot extremes for 4-days back-trajectories at a) 100 m b) 1500 m; and for 10-days back-trajectories at c) 100 m, d) 1500 m height.

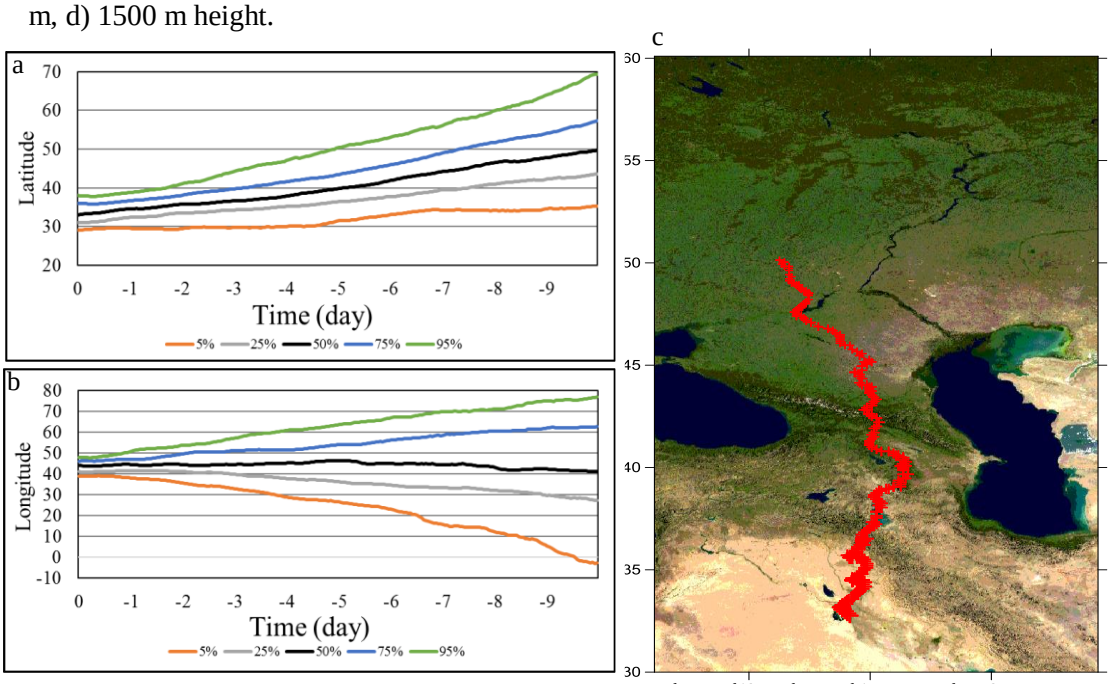

Figure 5.5: a**)** Meridional and b) zonal evolution of the 5th, 25th, 50th, 75th and 95th percentiles along the 100 m height back-trajectories of the air-masses causing hot extreme events in Iraq and c) median pathway.

Figures 5.6a and b shows the density of 4-days back-trajectories at 100 m and 1500 m a.s.l. for the cold events. As in the case of hot events, the distribution of densities is similar for the 10-days back-trajectories (Figs. 5.6c and d), and indicates that the main flow is from East Europe and Siberia, travelling over the Black Sea at low levels, while it shifts more to the north-west at high levels.

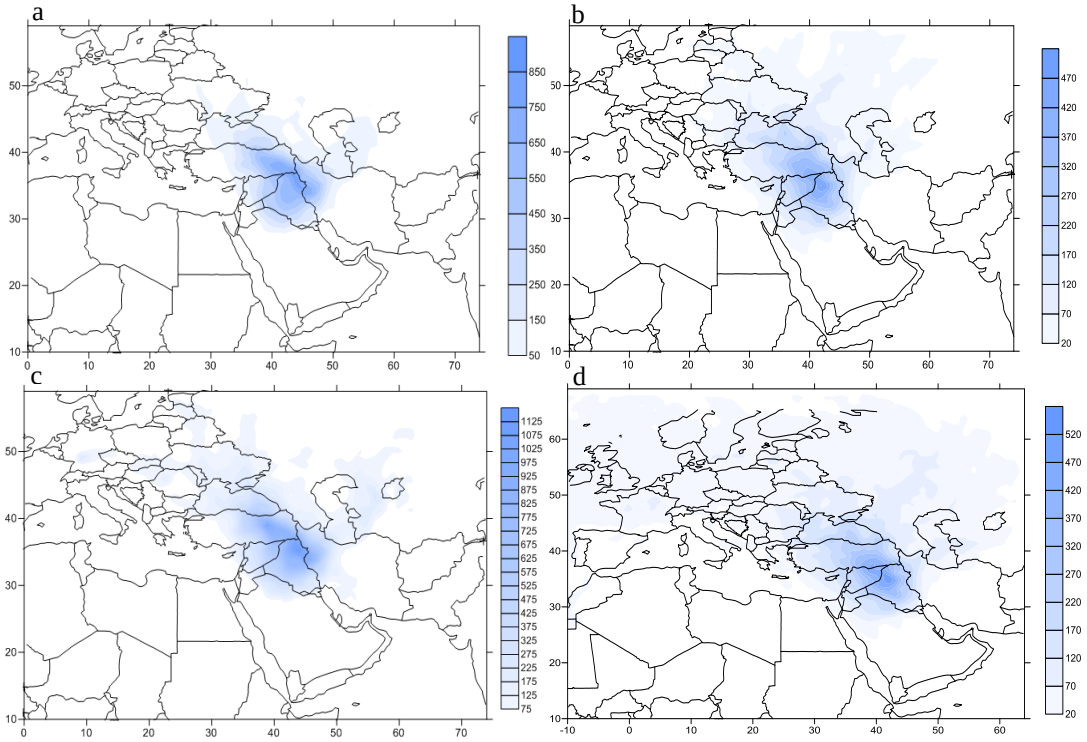

Figure 5.6: Trajectory densities (number of time steps per grid box) during cold extremes for 4-days back-trajectories at a) 100 m, b) 1500 m; and 10-days back-trajectories at c) 100 m, d) 1500 m height.

As mentioned above, the meridional and zonal displacements of the cold air masses along the trajectories are greater than for the hot air masses. Figures 5.7a and b show the evolution of latitude and longitude for the 5th, 25th, 50th, 75th and 95th percentiles for the back-trajectories arriving at 100 m and producing a cold extreme event. The longitudinal and latitudinal differences for the median are about 20 degrees during the 10 days, indicating advection of cold air masses from the Siberian regions and Europe. The latitudinal shift takes place mainly over the six days before the cold events (Fig. 5.7a). This result is consistent with situations in which large blocking anticyclone over the Siberian region and North-western Russia drives easterly winds over Europe and Middle East. This was identified as an important synoptic-scale cause of winter cold spells by Wallace *et al*. (2006) and Al-Hamawy *et al*. (2011). Figure 5.7c shows how the median

air mass pathway starts over Belarus and moves to Ukraine, and pass the Black see toured to Turkey, before entering Iraq from the north, 40 hours before the extreme events. Finally, it moves to Central Iraq.

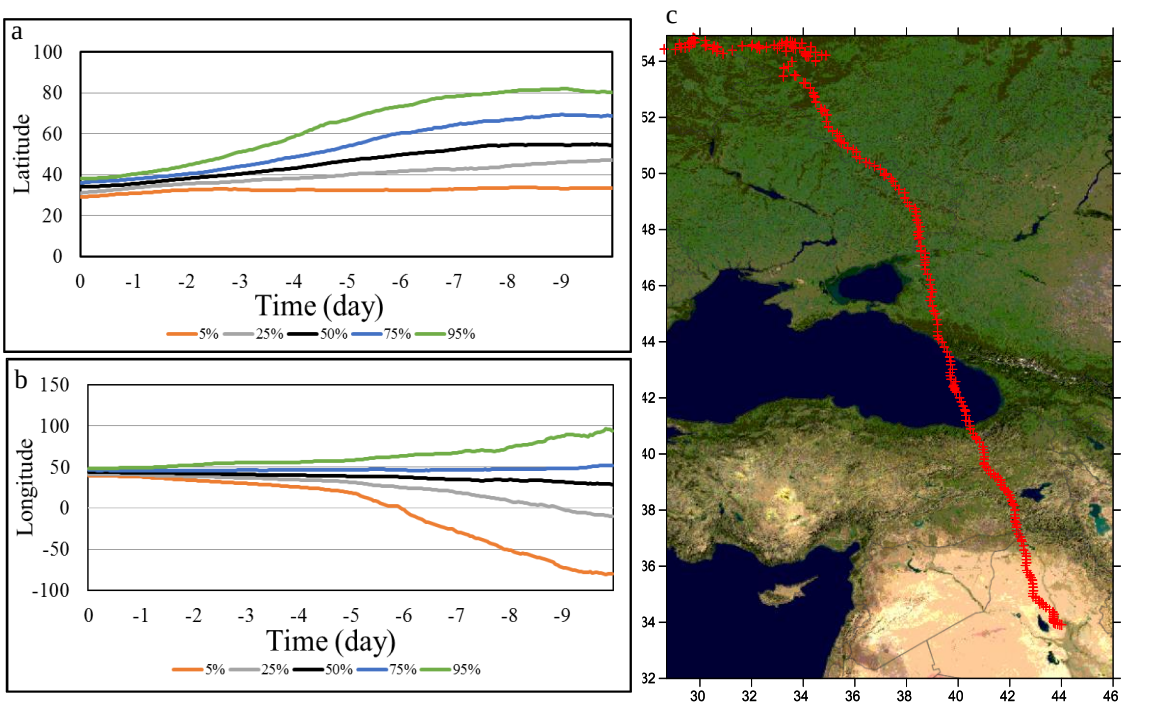

Figure 5.7: a) Meridional and b) zonal evolution of the 5th, 25th, 50th, 75th and 95th percentiles along the 100 m height back-trajectories of the air-masses causing cold extreme events in Iraq and c) median pathway.

5.2.4. Evolution of the physical variables for hot events

The evolution of temperature, potential temperature, mixing-layer height, relative humidity, and downward solar radiation for hot events has been analysed along the 100 m height back-trajectories. As in the previous section, the evolution is analysed by calculating the 5th, 25th, 50th, 75th and 95th percentiles of the variables at each time step. The evolution of the temperature along the median 10-day back-trajectory (Fig. 5.8a, in black) shows an increase of the air mass temperature along the trajectory, with a clear diurnal cycle during the 10 days before the extremes, which indicates the air mass did not travel over the water. Two different increasing periods can be distinguished: before entering Iraq, between 10 and 4 days before the extreme event, the median temperature rose by 11 K. Once the air mass entered in Iraq, the temperature increased by 14 K in three consecutive days. The evolution of the potential temperature (Fig. 5.8b) is similar,

indicating diabatic heating of air masses due to absorption of sensible heat from the ground.

Figure 5.8c shows the evolution of the mixing-layer height along the median trajectory. During the last four days before hot events, there is a progressive increase in its height and the diurnal cycle is clearer, indicating greater convection when the air mass enters Iraq (four days prior to the events in the case of the 95th, median and 75th percentiles; one day prior to the event in the case of the 25th and 5th percentile).

The downward solar radiation flux along the median back-trajectory (Fig. 5.8d) slightly increased during the 7 days before extreme events when the air mass moved to the south.

The evolution of the median relative humidity (Fig. 5.8e) follows, as expected, an opposite evolution to that of temperature; when the air mass enters Iraq its relative humidity drastically drops to values around 9%.

The diabatic and adiabatic changes in temperature can be analysed by observing Fig. 5.8f where the median temperature and the median potential temperature are represented for each trajectory time step. The red star indicates the beginning of the trajectory 10 days before the extreme events and the blue square at 72 hour before. It can be observed a diabatic warming becoming more pronounced 3 days before the extreme (indicated by the greater separation between points), with a total increase of 29 K along the path. During the 5 first days there is a pronounced subsidence (Fig. 5.8.g) but the air masses remain at approximatively a constant height the 4 days previous to the extremes. This indicates that although during the first days, a part of the warming is adiabatic by descend of the air-masses, in the last stages the main cause is the absorption of sensible heat. Consequently, hot episodes develop due to a progressive warming of air masses with long residence-times over the land and recirculation processes associated, probably, to summer days with weak baric gradient. This is not in agreement with the results of Al-Hamawy *et al*. (2011) who analysing 20 years of synoptic situations concluded that high temperatures in Iraq are mainly caused by the influence of a low-pressure system extending above Iran, which was developed over the Indian subcontinent and create a hot easterly flow towards the

Middle East region. This would imply that the spatial extent and intensity of the episodes are reinforced by the diurnal development of the monsoon thermal low.

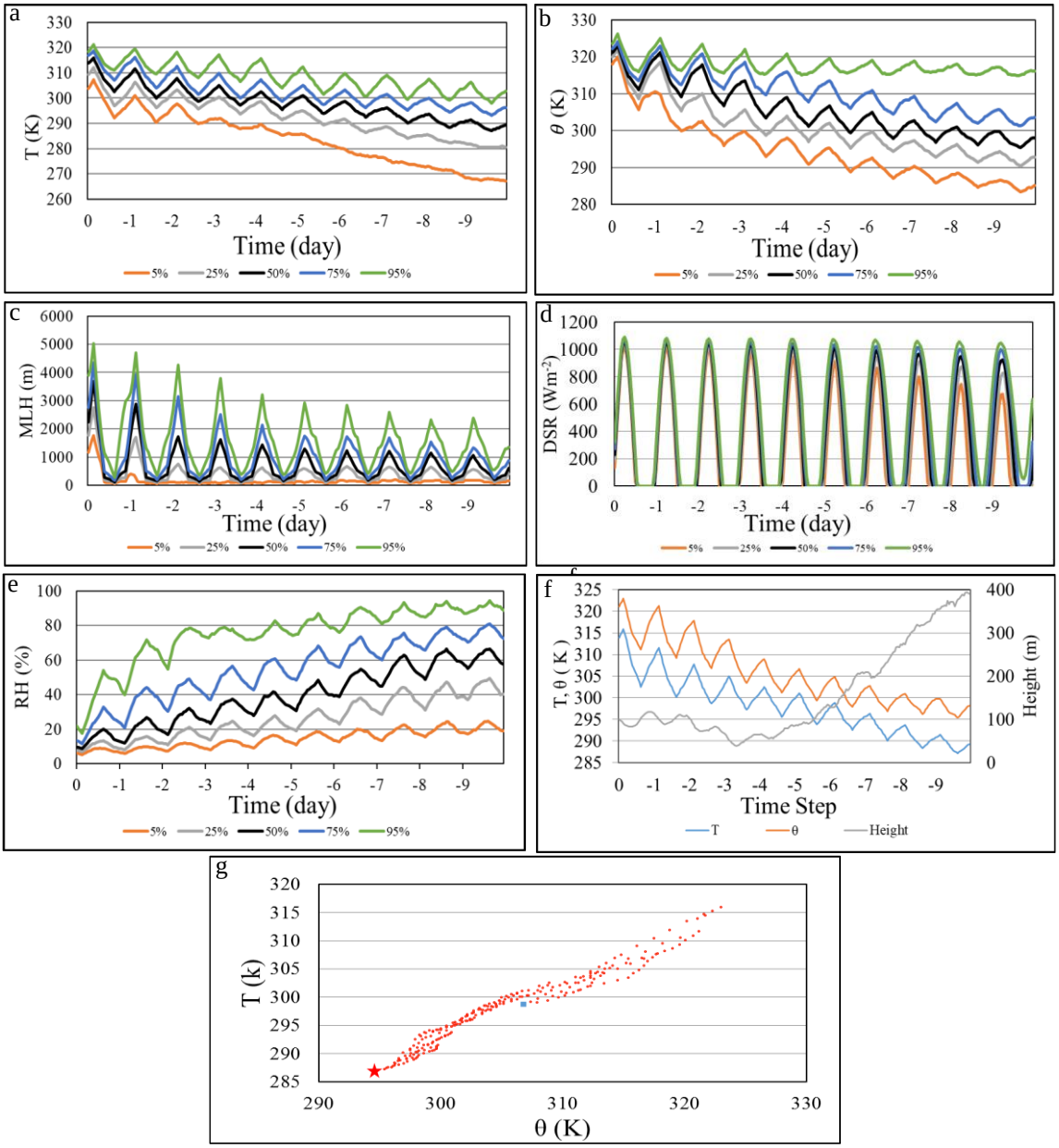

Figure 5.8: Evolution along the back-trajectories of hot events of the 5th, 25th, 50th, 75th and 95th percentiles of a) temperature; b) potential temperature; c) mixing-layer height; d) relative humidity; e) downward solar radiation, f) median temperature ,potential temperature and height and g) temperature vs potential temperature along the 10-day back-trajectories for hot extremes. Each point represents the T and θ median of all trajectories at a specific time step. The star indicates the beginning of the trajectory 10 days before the extreme events, and the blue square at 72 hours before.

5.2.5. Evolution of the physical variables for cold events

Figure 5.9 shows the evolution of temperature, potential temperature, mixing-layer height, relative humidity and downward solar radiation along the 5th, 25th, 50th, 75th and 95th percentiles of 10-day back-trajectories for the cold events. Temperature shows moderate diurnal cycle more pronounced during the days previous to the extreme events. There is a progressive increase of temperature as the air mass approaches Iraq: +28 K and +5 K for the 5th and 95th percentiles, respectively and +9 K for the median (Fig. 5.9a). Median potential temperature (Fig. 5.9b) shows a different evolution and consequently diabatic and adiabatic processes are involved during the median trajectory. Only during the last 14 hours before the event both temperatures present a similar evolution due to a diabatic process involving radiative cooling during the night once the air mass has entered Iraq.

The evolution of the mixing-layer height shows a less-pronounced diurnal cycle than for the warm extremes (Fig. 5.9c). From day 10 to 6 before the events, the mixing-layer height oscillation is almost imperceptible for the median and the values are lower. During these days the air mass is at high latitudes. Diurnal oscillation became more pronounced five days prior to the events, whereas higher values occur when the air mass travels over Turkey and it enters in Iraq.

In contrast to hot events, the median incident solar radiation flux for cold events displayed low values when the air mass is at high latitudes (days 10 to 9). Then it progressively increases as the air mass moves south, reflecting the large difference of incoming solar radiation during the winter between places with different latitude (Fig. 5.9d).

Relative humidity of the median trajectory shows large values remaining relatively constant over the central part of the path when the air mass crosses over continental Europe, followed by an increase the day prior to the events (Fig. 5.9e) due to inverse relationship between the temperature and relative humidity.

The evolution of temperature and potential temperature along the median back-trajectory (Fig. 5.9f) reflects the diurnal cycle of radiative heating/cooling, that is amplified as the air-masses approaches their destination in Iraq. Diabatic heating during the diurnal hours by absorption of sensible heat from the surface is particularly important during the last

two days, as well as the radiative cooling during night of the last 12 hours. On the other hand, subsidence is present in the entire path (Fig. 5.9g). Thus, an important contribution to the global temperature increase of 9 K is due to adiabatic warming by descent of the air masses. During the first three days in which the air masses move over high-latitudinal regions radiative cooling is compensated by adiabatic warming and the temperature remain approximately constant. Afterwards, a net increase in temperature is produced probably because the cooling is lower as the air masses cross regions of lower latitude, prevailing adiabatic warming.

The evolution of the back-trajectories and the associated physical variables indicates that cold events are caused by mechanisms different from those driving hot events: air mass advection from Siberia and Eastern Europe seems to be the main process that causes cold extreme events. This is in agreement with the presence of Siberian high-pressure systems centred over Turkey, covering most of the eastern Mediterranean and bringing cold air to Iraq, described by Al-Hamawy *et al*. (2011).

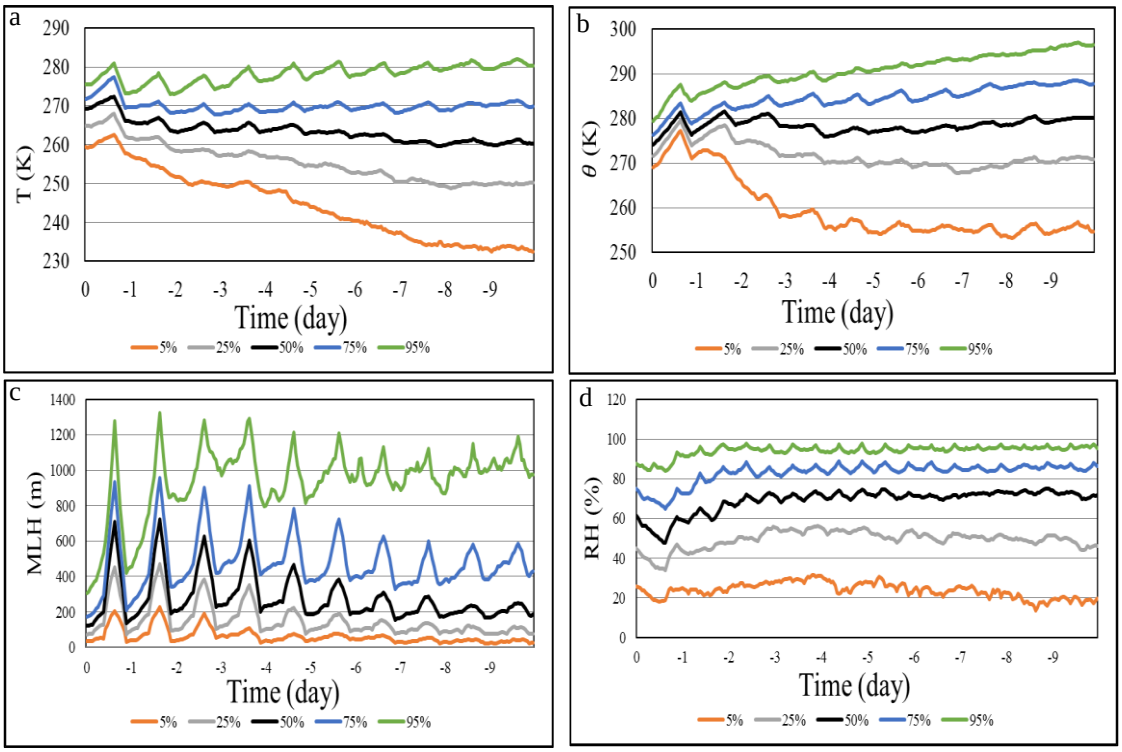

Figure 5.9: Evolution along the back-trajectories of cold events of the 5th, 25th, 50th, 75th and 95th percentiles of a) temperature; b) potential temperature; c) mixing-layer height; d) relative humidity.

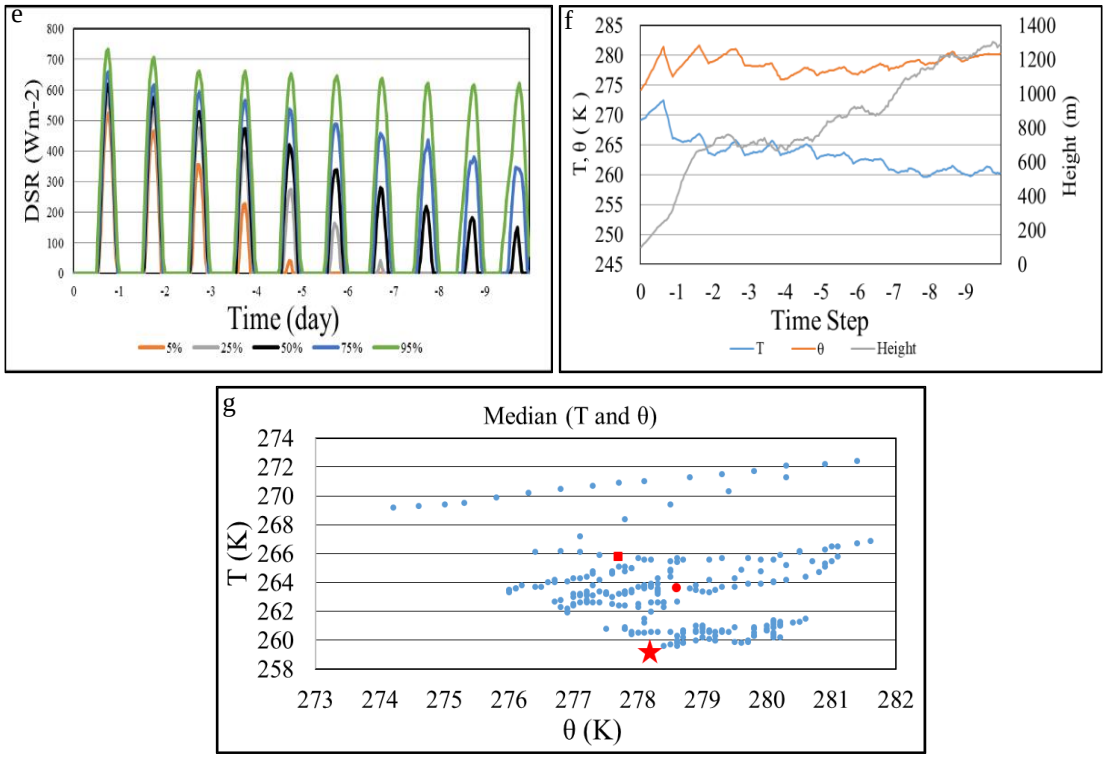

Figure 5.9:(cont) Evolution along the back-trajectories of cold events of the 5th, 25th, 50th, 75th and 95th percentiles of e) downward solar radiation, f) median temperature ,potential temperature and height and g) temperature vs potential temperature along the 10-days back-trajectories at 100 m for cold extremes. Each point represents the T and θ median of all trajectories at a specific time step. The star indicates the beginning of the trajectory 10 days before the extreme events, the blue circle 72 hours before and the red square 24 hours before extreme event.

5.3. Summary and Conclusions

A Lagrangian approach is used to investigate the driving mechanisms of hot and cold extreme events over a 20-year period (1994-2013) in Iraq, based on the 99.9th/0.1th percentile of the 2-m height temperature profiles of the ERA-Interim reanalysis data.

We find a positive trend in the number of both hot and cold events during the analysed period. The BWh region recorded the highest number of hot and cold extreme events over the course of the 20 years with 61%, while the BSh and Csa regions only recorded 16% and 23% of the events, respectively. Regarding the different regions, the trend for hot events is twice larger in the Csa region (North) when compared with the other regions (10.4 vs 5.2 days/decade). For the cold events the larger trend occurred in the BWh region (South) (10.2 vs 3.2 days/decade).

Concerning the influence of primary climatic patterns affecting the Middle East, the average temperature of hot extremes correlated positively ($p<0.01$) with EA. In contrast, no correlations with NAO and AO indices were obtained for hot extreme events, On the other hand, no correlations were found for cold events.

No significant meridional advection is involved in the production of hot extremes. Most of the back-trajectories remained within Iraq and its close surroundings during the two or three days prior to hot events.

The evolution of the physical variables indicates that the occurrence of hot extremes was due to diabatic warming caused by air masses of long residence over the Iraqi mainland, and due to recirculation processes induced probably by situations of weak baric gradient. Our results contrast with previous studies that attributed the phenomena to occasional monsoon influences from India.

The back-trajectories of cold events are associated to advection of air masses from Siberia and north-eastern Europe. The evolution of the physical variables along the back-trajectories indicates that the production of cold events is driven by different mechanisms than for the hot events. The evolution of the median temperature versus the median potential temperature shows that air masses experience radiative cooling during their passage over the northern regions that is approximately balanced by adiabatic heating associated with the descend of the air masses. Adiabatic warming due to subsidence prevails during the last days, and is persistent until the start of the episodes.

Chapter 6

Chapter 6

General conclusions and future work

This study examines the mechanisms underlying the occurrence of hot and cold events for the 20-year period 1994-2013 in the Iberian Peninsula and Iraq. The hot/cold episodes were selected at 15 UTC and 03 UTC by applying the criterion of the $99.9^{th}/0.1^{th}$ percentile in the 2-m height temperature obtained from the ERA-Interim reanalysis database. This yielded 1950 and 1500 hot/cold extreme events for IP and Iraq respectively. In both regions, a Lagrangian approach was used to analyse the trajectories of the air-masses causing the hot/cold extreme events.

The relationships between the annual number of extremes and the average annual extreme temperature and the NAO, AO, WeMO and EA indices were analysed.

For the case of IP, the synoptic conditions producing the events were characterised by means of Principal Component Analysis of the sea-level pressure and geopotential fields at 850 and 700 hPa. For one particular extreme event, WRF numerical simulations were used to describe in detail the atmospheric conditions.

The conclusions are organised as follows: first, the annual distribution and correlations with the climatic indices in IP and Iraq; second, the trajectory density and the physical mechanisms related with extremes in IP and Iraq; third, the synoptic situations leading to extremes in IP. Finally, the mechanisms involved in producing two study cases of hot events in IP.

6.1. Annual distribution and correlation with climatic indices in IP and Iraq

6.1.1. The number of hot events and annual mean temperature show a positive trend in each climatic region in IP and Iraq. This trend is double for the number of hot events in northern Iraq and eastern IP. In contrast, the difference in the number of hot events between the first decade of the study period (1994-2003) and the second one (2003-2013) shows that Iraq was recorded a small increase in the number of hot events in the second decade (41% vs 59 %), while the Iberian Peninsula has suffered a significant increase in the number of hot events during the second decade (19% vs 81%).

6.1.2. There is a positive trend in the number of cold events in IP and Iraq. Comparing the two decades, there is an important increase in the number of cold events during the second decade for IP, 70%, while in Iraq is 30%.

6.1.3. 70 % of hot and cold extreme events were recorded only in five different years during the study period in IP and Iraq.

6.1.4. For IP, the analysis of the influence of the main climatic indices shows that the annual number of cold extremes correlates negatively ($p < 0.01$) with annual NAO and AO. Moreover, a significant positive correlation ($p < 0.01$) was found between annual WeMO and the annual average temperature of hot events.

For Iraq, the annual average temperature of hot extremes correlated positively ($p<0.01$) with EA.

6.2.Trajectory analysis and evolution of the physical variables

6.2.1. The analysis of the back-trajectories for IP and Iraq shows that local recirculation of warm air-masses is mainly responsible for the high temperatures rather than the occasional entrance of North African air-masses. Most of the back-trajectories remained within the IP and Iraq and its close surroundings during the two or three days prior to the hot events.

Back-trajectories associated to cold events were mainly related with advection of air-masses from northeast and northern Europe for IP and northeast and eastern Europe for Iraq.

6.2.2. The evolution of the physical variables indicates that the hot extremes were mainly produced by diabatic warming during the last three days before the extreme.

The mechanisms producing cold events in IP and Iraq are also similar. In Iraq, between the days -10 and -9 before the extreme, the air-masses experienced diabatic cooling. This was followed by adiabatic warming due to subsidence, and finally radiative cooling during the two days before the event. While in IP, in the first days the air-masses experienced diabatic radiative cooling during their passage through the high latitude regions. This was followed by adiabatic warming due to subsidence, which persisted until the start of the episodes.

6.3. Duration and synoptic patterns in IP

6.3.1. Most of the hot extreme events in IP (80% for nocturnal and 70% for diurnal) persist between one and three days, with durations of one day being the most frequent.

6.3.2. For the cold events, about 80% persisted between one and three days, with 2-days durations being the most frequent.

6.3.3. The principal component analysis for hot events shows three synoptic configurations: a low-pressure system centered over North Africa; a ridge from the Atlantic anticyclone extending towards central Europe; and a deep low-pressure system over the south of Iceland and a high-pressure system over Scandinavia.

6.3.4. Two synoptic configurations are related to cold air-masses entering IP: the first one, associated with the presence of an anticyclonic system over central and northern Europe at low levels and a trough in height. The second configuration corresponds to the formation of a blocking dipole with centers in the North Atlantic (south of Iceland, Scandinavia or north-western Russia) and Central Europe.

6.4. Two study cases of hot extreme events in IP

For the extreme on 10 August 2012, the temperature evolution along the median back–trajectory for 53 grid points shows a significant increase and a clear diurnal cycle when the air mass enters IP during the last two days before the event due to diabatic heating produced by the absorption of sensible heat flux.

For the extreme event occurring at point A on 15 August 2012, there are three possible causes: (1) heat accumulation in the IP during the previous days, (2) the air-masses arriving to the central eastern coast mainly cross the IP at the southern part, in which the sensible heat flux is high, enhancing thus temperature and potential temperature, and (3)

a large part of IP (specially the central area) was covered by clouds preventing the temperature to rise in other areas.

The methodology presented here can be applied in the future to events selected by using a different criterion, such as the definition of heat wave, or to some particular extreme events of interest. Further research might get new insight by adding other air parameters not included in our study. For example, microphysics, suggested by Curry (1987), could play a fundamental role by increasing the lower troposphere cooling due to the presence of ice crystals. Another approach would be the study of particular years recording a high number of extreme events in Europe and their relation with other phenomena as El Niño and La Niña. It would also be interesting to simulate extreme events effecting different regions in Europe in order to determine the differences in the physical mechanisms leading to these situations.

Bibliography

Alexander, L.V., Zhang, X., Peterson, T.C., Caesar, J., Gleason, B., Klein Tank, A.M.G., Haylock, M., Collins, D., Trewin, B., Rahimzadeh, F., Tagipour, A., Rupa Kumar, K., Revadekar, J., Griffiths, G., Vincent, L., Stephenson, D. B., Burn, J., Aguilar, E., Brunet, M., Taylor, M., New, M., Zhai, P., Rusticucci, M. and Vázquez-Aguirre, J.L., 2006. Global observed changes in daily climate extremes of temperature and precipitation. *J. Geophys. Res*., 111: D05109, doi:10.1029/2005JD006290.

Al-Khalidi, J., Dima, M., Vaideanu, P. and Stefan, S., 2017. North Atlantic and Indian Ocean links with Iraq Climate. *Atmosphere*. 8(12): 235.

Andrade C, Leite SM, Santos JA., 2012. Temperature extremes in Europe: overview of their driving atmospheric patterns. *Nat. Hazards Earth Syst. Sci.* 12: 1671-1691.

Badry, M.M., Mehdi, M.S., Khawar, J.M., 1979. Water resources in Iraq. In: Johl, S.S. (Ed.), Irrigation and Agricultural Development. A joint publication of ECWA, FAO and the Foundation for Scientific Research of Iraq. *Pergamon Press.*

Bieli M, Pfahl S, Wernli H., 2014. A lagrangian investigation of hot and cold temperature Extremes in Europe. *Q. J. Royal Meteorol. Soc.* 141: 98-108.

Bladé I, Liebmann B, Fortuny D, Van Oldenborgh GJ., 2011. Observed and simulated impacts of the summer NAO in Europe: implications for projected drying in the Mediterranean region. *Clim. Dynam.* 39: 709-727.

Belmonte, J., Alarcón, M., Àvila, A., Scialabba, E., and Pino, D., 2008. Long-range transport of beech (Fagus sylvatica L.) pollen to Catalonia (north-eastern Spain), *Int J Biometeorol*. 52: 675–687.

Brunet M, Jones PD, Sigró J, Saladié O, Aguilar E, Moberg A, Della-Marta PM, Lister D, Walther A, Lopez D., 2007. Temporal and spatial temperature variability and change over Spain during 1850–2005. *J. of Geophys. Res.* 112: 28–D12117.

Buehler T, Raible CC, Stocker TF., 2011. The relationship of winter season North Atlantic blocking frequencies to extreme cold or dry spells in the ERA-40, *Tellus*, Ser. A. 63: 212–222, doi:10.1111/j.1600-0870.2010.00492.x.

Capel J. J., 2000. El clima de la península Ibérica (2ª ed.). *Ariel Geografía, Barcelona, Spain.*

Castro–Díez, Y., Esteban–Parra, M.J., Staudt, M. and Gámiz–Fortis, S., 2007. Temperature and precipitation changes in Andalusia in the Iberian Peninsula and Northern Hemisphere context. In: Sousa A., García–Barrón L., and Jurado V. (eds) Climate change in Andalusia: trends and environmental consequences. *Consejería de Medio Ambiente (Junta de Andalucía).*

Cattiaux J, Vautard R, Cassou C, Yiou P, Masson-Delmotte V, Codron F., 2010. Winter 2010 in Europe: a cold extreme in a warming climate. *Geophys. Res. Lett.* 37(20).

Charron, A., Plaisance, H., Sauvage, S., Coddeville, P., Galloo, J. C., and Guillermo, R., 1998: Intercomparison between three receptor-oriented models applied to acidic species in precipitation, *Sci. Total Environ.* 223: 53–63.

Compagnucci RH, Araneo D, Canziani PO., 2001. Principal sequence pattern analysis: a new approach to classifying the evolution of atmospheric systems. *Int. J. Climatol.* 21: 197–217.

Cooney C M., 2012. Managing the risks of extreme weather: IPCC Special Report. *Environ. Health Perspect*. 120: a58.

Croci-Maspoli M, Schwierz C, Davies HC., 2007. Atmospheric blocking: space-time links to the NAO and PNA. *Clim. Dynam*. 29: 713-725.

Chen, F. and Dudhia, J., 2001. Coupling an advanced land surface–hydrology model with the Penn State–NCAR MM5 modeling system. Part I: Model implementation and sensitivity. *Mon. Weather Rev.*, 129: 569–585.

Curry, J., 1987. The contribution of radiative cooling to the formation of cold-core anticyclones. *J. atmos. scie.* 44(18): 2575-2592.

D'Ippoliti, D., Michelozzi, P., Marino, C., de'Donato, F., Menne, B., Katsouyanni, K., Kirchmayer, U., Analitis, A., Medina-Ramón, M., Paldy, A. Atkinson, R., Kovats, S., Bisanti, L., Schneider, A., Lefranc, A., Iñiguez, C. and Perucci, C. A., 2010. The impact

of heat waves on mortality in 9 European cities: results from the Euro HEAT project. *Environ. Health*, 9(1): 37.

Dankers R, Hiederer R., 2008. Extreme temperatures and precipitation in Europe: analysis of a high-resolution climate change scenario. *Office for Official Publications of the European Communities, Luxembourg, EUR*. 23291.

Dantart, J.; Stefanescu, C.; Àvila, A. and Alarcón, M., 2009. Long-distance wind-borne dispersal of the moth Cornifrons ulceratalis(Lepidoptera: Crambidae: Evergestinae) into the northern Mediterranean. *Eur. J. Entomol.* 106: 225-229.

Del Río S, Herrero L, Pinto-Gomes C, Penas A., 2011. Spatial analysis of mean temperature trends in Spain over the period 1961–2006. *Glob. Planet. Change* 78: 65-75.

Della-Marta PM, Luterbacher J, von Weissenfluh H, Xoplaki E, Brunet M, Wanner H. 2007. Summer heat waves over Western Europe 1880–2003, their relationship to large-scale forcings and predictability. *Clim. Dynam.* 29: 251-275.

Draxler RR, Rolph GD., 2003. HYSPLIT (HYbrid Single-Particle Lagrangian Integrated Trajectory) Model access via NOAA ARL READY website (http://www.arl.noaa.gov/ ready/hysplit4.html). *NOAA Air Resources Laboratory, Silver Spring, MD.*

Dudhia, J., 1989. Numerical study of convection observed during the winter monsoon experiment using a mesoscale two–dimensional model. *J. Atmos. Sci*., 46: 3077–3107.

Efthymiadis D, Goodess C M, Jones P D., 2011. Trends in Mediterranean gridded temperature extremes and large-scale circulation influences. *Nat. Hazard. Earth Sys.* 11: 2199-2214.

El Kenawy A, López-Moreno JI, Vicente-Serrano S.M., 2013. Summer temperature extremes in northeastern Spain: spatial regionalization and links to atmospheric circulation (1960–2006). *Theor. Appl. Climatol.* 113: 387-405.

FAO., 2003. Towards Sustainable Agricultural Development in Iraq: The Transition from Relief, *Rehabilitation and Reconstruction to Development.* (222 pp).

Favà V, Curto JJ, Llasat MC., 2016. Relationship between the summer NAO and maximum temperatures for the Iberian Peninsula. *Theor. Appl. Climatol.* 126: 77-91.

Fernández-Montes S, Rodrigo FS., 2011. Trends in seasonal indices of daily temperature extremes in the Iberian Peninsula, 1929–2005. *Int. J. Climatol.* 32: 2320-2332.

Font–Tullot, I., 2000. Climatología de España y Portugal (Vol. 76). *Universidad de Salamanca.*

Frich P, Alexander LV, Della-Marta P, Gleason B, Haylock M, Tank AK, Peterson T., 2002. Observed coherent changes in climatic extremes during the second half of the twentieth century. *Clim. Res.* 19: 193-212.

Furió D, Meneu V., 2011. Analysis of extreme temperatures for four sites across Peninsular Spain. *Theor. Appl. Climatol.* 104: 83-99.

García-Herrera, R., Díaz, J., Trigo, R.M., Luterbacher, J. and Fischer, E.M., 2010. A review of the European summer heat wave of 2003. *Crit. Rev. Env. Sci. Tec.* 40(4): 267-306.

Harsant J, Pavlovic L, Chiu G, Sultmanis S, Sage TL., 2013. High temperature stress and its effect on pollen development and morphological components of harvest index in the C3 model grass Brachypodium distachyon. *J. Exp. Bot.* doi:10.1093/jxb/ert142

Hoinka KP, Castro MD., 2003. The Iberian Peninsula thermal low. *Q. J. Roy. Meteor. Soc.* 129: 1491-1511.

Holton, J. R., 2004. An Introduction to Dynamic Meteorology. *Elsevier*, London, UK.

Hong, S.H., and Pan, H.L., 1996. Nonlocal boundary layer vertical diffusion in a medium–range forecast model. *Mon. Weather Rev*. 124: 2322–2339.

Hong, S.Y., Dudhia, J., and Chen, S.H., 2004. A revised approach to ice microphysical processes for the bulk parameterization of clouds and precipitation. *Mon. Weather Rev*. 132: 103–120.

Horton DE, Singh JD, Swain DL, Rajaratnam B, Diffenbaugh NS., 2015. Contribution of changes in atmospheric circulation patterns to extreme temperature trends. *Nature*, 522: 465-471.

Hurrell JW, Kushnir Y, Visbeck M, Ottersen G., 2013. An overview of the North Atlantic Oscillation. In: Hurrell JW, Kushnir Y, Visbeck M, Ottersen G (eds) The North Atlantic Oscillation: climate significance and environmental impact. *Geophys. Monograph Ser, American Physical Union, Washington, DC*. 1−35

Huth R., 1996. An intercomparison of computer-assisted circulation classification methods. *Int. J. Climatol.* 16: 893–922.

IPCC, Climate Change., 2013. The Physical Science Basis. Contribution of Working Group I to the Fifth Assessment Report of the Intergovernmental Panel on Climate Change, *Cambridge University Press, Cambridge, UK.*

Izquierdo R, Aguillaume L, Alarcón M, Avila A., 2014. Effects of teleconnection patterns on the atmospheric routes, precipitation amount and chemistry in the north-eastern Iberian Peninsula. *Atmos. Environ*. 89: 482–490.

Izquierdo R, Alarcón M, Periago C, Belmonte J., 2015. Is long range transport of pollen in the NW Mediterranean basin influenced by Northern Hemisphere teleconnection patterns?. *Sci. Total Environ.* 532: 771-779.

Jolly, W.M., Dobbertin, M., Zimmermann, N. E., and Reichstein, M., 2005. Divergent vegetation growth responses to the 2003 heat wave in the Swiss Alps. *Geophys. Res. Lett*. 32: 18409–18418.

Jones PD, Jonsson T, Wheeler D., 1997. Extension of the North Atlantic Oscillation using early instrumental pressure observations from Gibraltar and South-West Iceland. *J Climatol* 17:1433–1450.

Jorba O, Pérez C, Rocadensbosch F, Baldasano JM., 2004. Cluster analysis of 4-day back trajectories arriving in the Barcelona area, Spain, from 1997 to 2002. *J. Appl. Meteorol.* 43: 887–901.

Josey SA, Marsh R., 2005 Surface freshwater flux variability and recent freshening of the North Atlantic in the eastern subpolar gyre. *J Geophys Res. 110*: C05008. doi:10.1029/2004JC002521

Jung T, Vitart F, Ferranti L, Morcrette JJ., 2011. Origin and predictability of the extreme negative NAO winter of 2009/10. *Geophys. Res. Lett.* 38(7).

Katz RW, Brown BG., 1992. Extreme events in a changing climate: variability is more important than averages. *Clim. Change.* 21: 289-302.

Kebede AS, Dunford R, Mokrech M, Audsley E, Harrison PA, Holman IP, Nicholls RJ, Rickebusch S, Rounsevell MDA, Sabate S, Sallaba F, Sanchez A, Savin C, Trnka M, Wimmer F., 2015. Direct and indirect impacts of climate and socio-economic change in Europe: a sensitivity analysis for key land- and water-based sectors. *Clim. Change.* 128: 261-277.

Khidher, S.A. and Pilesjö, P., 2015. The effect of the North Atlantic Oscillation on the Iraqi climate 1982–2000. *Theor. Appl. Climatol*. 122(3-4): 771-782.

Knežević, S., Tošić, I., Unkašević, M. and Pejanović, G., 2014. The influence of the East Atlantic Oscillation to climate indices based on the daily minimum temperatures in Serbia. *Theor. Appl.Climatol*. 116(3-4): 435-446.

López-Bustins JA, Martín-Vide J, Sanchez-Lorenzo A., 2008. Iberia Winter rainfall trends based upon changes in teleconnection and circulation patterns. *Glob. Planet. Change.* 63: 171-176.

Luterbacher J, Dietrich D, Xoplaki E, Grosjean M, Wanner H., 2004. European seasonal and annual temperature variability, trends, and extremes since 1500. *Science.* 303: 499-1503.

Izquierdo, R.; Alarcón, M.; Mazón, J.; Pino, D.; Concepción De Linares, C.; Aguinagalde, X.; Belmonte, J., 2017. Are the Pyrenees a barrier for the transport of birch (Betula) pollen from Central Europe to the Iberian Peninsula? *Science of the Total Environment.* 575: 1183–1196

Malinowski, J.C., 2002. Iraq: A Geography.

Martín-Vide J, López-Bustins JA., 2006. The Western Mediterranean Oscillation and rainfall in the Iberian Peninsula. *Int. J. Biometeorol*. 26 (11): 1455-1475.

Mazon, J., 2014. The influence of thermal discomfort on the attention index of teenagers: An experimental evaluation. *Int. J. Biometeorol*. 58: 717–724.

Meehl, G. A. and Tebald, C., 2004. More intense, more frequent and longer lasting heat waves in the 21st century. *Science.* 13: 994–997.

Millán MM, Artíñano B, Alonso LA, Navazo M, Castro M., 1991. The effect of meso-scale flows on regional and long-range atmospheric transport in the western Mediterranean area. *Atmos. Environ.* 25: 949-963.

Millán MM, Salvador R, Mantilla E, Kallos G., 1997. Photo-oxidant dynamics in the Mediterranean basin in summer: results from European research projects. *J. Geophys. Res.* 102: 8811–8823.

Mlawer, E.J., Tubman, S.J., Brown, P.D., Iacono, M.J., and Clough, S.A., 1997. Radiative transfer for inhomogeneous atmospheres: RTM, a validated correlated–k model for the long wave. *J. Geophys. Res*. 102: 663–682.

Muslih, K.D., Błażejczyk, K., 2016. The inter-annual variations and the long-term trends of monthly air temperatures in Iraq over the period 1941–2013. *Theor. Appl.Climatol.* 1–14. doi:10.1007/s00704-016-1915-6.

Nasrallah, H.A., Nieplova, E., Ramadan, E., 2004. Warm season extreme temperature events in Kuwait. J. *Arid Environ*. 56 (2): 357–371. doi:10.1016/S0140-1963(03)00007-7.

Glickman, T.S. and Zenk, W., 2000. Glossary of meteorology. *American Meteorological Society*.

Peel, M. C., Finlayson, B. L. and McMahon, T. A., 2007, Updated World Map of the Koppen-Geiger Climate Classification Updated world map of the K ¨ oppen-Geiger climate classification, *Hydrology and Earth System Sciences*. doi: 10.5194/hess-11-1633-2007.

Pfahl S, Wernli H., 2012. Quantifying the relevance of atmospheric blocking for co-located temperature extremes in the Northern Hemisphere on (sub-) daily time scales. *Geophys. Res. Lett*. 39: L12807.

Prieto L, Herrera RG, Díaz J, Hernández E, Del Teso T., 2004. Minimum extreme temperatures over Peninsular Spain. *Glob. Planet Change* 44: 59-71.

Quadrelli R, Pavan V, Molteni F., 2001. Wintertime variability of Mediterranean precipitation and its links with large-scale circulation anomalies. *Clim Dyn* 17: 457–466

Robaa, E.S.M., Al-Barazanji, Z., 2015. Mann-Kendall trend analysis of surface air temperatures and rainfall in Iraq. *Idojaras.* 119 (4): 493–514.

Rodrigo FS., 2015. On the covariability of seasonal temperatures and precipitation in Spain, 1956-2005. *Int. J. Climatol.* 35: 3362-3370.

Rodríguez-Puebla C, Encinas AH, García-Casado LA, Nieto S., 2010. Trends in warm days and cold nights over the Iberian Peninsula: relationships to large-scale variables. *Clim. Change.* 100: 667-684.

Sanaa Abbas-Alhamawy., 2011. *The nature and influence of Mediterranean pressure system on eastern Mediterranean region.* Doctorate degree in atmospheric science, college of science. *mustansiriyah university*.

Sáenz J, Zubillaga J, Rodríguez-Puebla C., 2001. Interannual winter temperature variability in the north of the Iberian Peninsula. *Clim. Res.* 16: 169-179.

Salman, S.A., Shahid, S., Ismail, T., Chung, E.S. and Al-Abadi, A.M., 2017. Long-term trends in daily temperature extremes in Iraq. *Atmos. Res*. 198: 97-107.

Schindler DW., 1997. Widespread effects of climatic warming on freshwater ecosystems in North America. *Hydrol. Process.* 11: 1043-1067.

Schönwiese CD, Rapp J., 1997. Climate Trend Atlas of Europe Based on Observations 1891–1990. Kluwer Academic publishers, *Dordrecht*. 235 pp.

Seibert, P., Kromp-Kolb, H., Baltensperger, U., Jost, D.T., Schwikowski, M., Kasper, A. and Puxbaum, H., 1994. Trajectory analysis of aerosol measurements at high alpine sites. *Transport and Transformation of Pollutants in the Troposphere*. 15: 689-693.

Serra C, Burgueño A., Lana X., 2001. Analysis of maximum and minimum daily temperatures recorded at Fabra Observatory (Barcelona, NE Spain) in the period 1917–1998. *Int. J. Climatol.* 21: 617–636.

Sillmann J, Croci-Maspoli M, Kallache M, Katz RW., 2011. Extreme cold winter temperatures in Europe under the influence of North Atlantic atmospheric blocking. *J. Clim.* 24: 5899-5913

Skamarock, W.C., Klemp, J.B., Dudhia, J., Gill, D.O., Barker, D.M., Duda, M., Huang, X.Y. and Powers, J.G., 2008. A Description of the Advanced Research WRF Version 3; Technical Report TN–475+STR; NCAR: *Boulder, CO, USA*.

Stefanescu, C., Alarcón, M., and Àvila, A., 2007. Migration of the Painted Lady butterfly Vanessa cardui to north-eastern Spain is aided by African wind currents, *J Anim Ecol*. 76: 888–898.

Steyn DG., 1998. Scaling the vertical structure of sea breezes. *Bound.-Layer Meteor.* 86: 505-524. doi:10.1023/A:1000743222389.

Stohl, A., 1996: Trajectory statistics - A new method to establish source-receptor relationship of air pollutants and its application to the transport of particulate sulfate in Europe, *Atmos Environ.* 30: 579–587.

Stohl A., 1998. Computation, accuracy and applications of trajectories - a review and bibliography, *Atmos. Environ.* 32: 947-966.

Tomassini L, Gerber EP, Baldwin MP, Bunzel F, Giorgetta M., 2012. The role of stratosphere-troposphere coupling in the occurrence of extreme winter cold spells over northern Europe. *J. Adv. Model. Earth Sy*. 4(4).

Trigo RM, Trigo, JF, DaCamara CC, Osborn TJ., 2004. Climate impact of the European winter blocking episodes from NCEP/NCAR Reanalyses. *Clim. Dyn*. 23:17-28, doi:10.1007/s00382-004-0410-4.

Tullot IF., 2000. *Climatologia de España y Portugal* (Vol. 76). Universidad de Salamanca.

Tyrlis, E., Lelieveld, J. and Steil, B., 2013. The summer circulation over the eastern Mediterranean and the Middle East: influence of the South Asian monsoon. *Clim. Dyn*. 40(5-6): 1103-1123.

UNDP (2010), Elasha, B.O., 2010. Mapping of climate change threats and human development impacts in the Arab region. In: UNDP Arab Development Report–Research Paper Series. *UNDP Regiona Bureau for the Arab States.*

P. M. Borrel, P. Borrell, T. Cvitas and W. Seiler (Eds.) Transport and Transformation of Pollutants in the Troposphere. *Academic Publishing, Den Haag*. 689-693.

Vicente-Serrano SM, Beguería S, López Moreno JI, El Kenawy A, Angulo MM., 2009. Daily atmospheric circulation events and extreme precipitation risk in northeast Spain: role of the North Atlantic Oscillation, the Western Mediterranean Oscillation, and the Mediterranean Oscillation. *J Geophys Res.* 114: D08106. doi:10.1029/2008JD011492

Walsh J E, Phillips AS, Portis DH, Chapman WL., 2001. Extreme cold outbreaks in the United States and Europe, 1948-99. *J. Clim.* 14: 2642-2658.

Wallace, J.M. and Gutzler, D.S., 1981. Teleconnections in the geopotential height field during the Northern Hemisphere winter. *Mon. Weather Rev*. 109(4): 784-812.

Wallace, J.M., and P.V. Hobbs., 2006: Atmospheric Science: An Introductory Survey 2nd ed. *Academic Press, NY*. 420-421.

Publications

The main publications and contributions to internationals meetings derived from this thesis are:

International meetings

Mohammed, A.J. and Alarcón Jordán, M., 2015. Analysis of the occurence of extreme temperatures in the Iberian Peninsula in a recent 20-year period. In *5 thMETMED International Conference on Meteorology and Climatology of the Mediterranean* (pp. 34-34). Istanbul (Tukey). March 2015

Mohammed, A.; Alarcón, M. Synoptic situations and occurrence of extreme temperatures in the Iberian Peninsula. Geophysical Research Abstracts Vol. 18, EGU General Assembly. Viena (Autria). March 2016

Journals

Mohammed, A.J.; Alarcón, M. and Pino, D. 2018, Extreme temperature events on the Iberian Peninsula: Statistical trajectory analysis and synoptic patterns, *International Journal of Climatology*, accepted 28/5/2018-DOI:10.1002/joc.5733,Wiley.

Participation in projects:

1. BATMAN project

Name of the project: **Atmospheric bio-aerosols: levels, transport and impacts (BATMAN)**

Reference: CTM2017-89565-C2-2-P

Founding entity: Ministerio de Economía y Competitividad. Programa proyectos I+D convocatoria 2012.

Duration: 1/01/2013 - 30/05/2016

Principal research: Marta Alarcón Jordán (Universitat Politécnica de Catalunya)

2. TECBIOMET project

Name of the project: **New Technologies for the study of the diversity and dynamics of aerobiological components and for their forecast based on Meteorology (TECBIOMET)**

Reference: CGL2012-39523-C02-02

Founding entity: Ministerio de Economía, Industria y Competitividad. Programa proyectos I+D convocatoria 2017.

Duration: 1/01/2018 - 31/12/2020

Principal reserach: Marta Alarcón Jordán (Universitat Politécnica de Catalunya)